Photovoltaic Source Simulators for Solar Power Conditioning Systems: Design Optimization, Modeling, and Control

Ahmed M. Koran

Dissertation Submitted to the Faculty of the
Virginia Polytechnic Institute and State University
In Partial Fulfillment of the Requirements for the Degree of

Doctor of Philosophy
In
Electrical Engineering

Jih-Sheng Lai, Chair
Virgilio A. Centeno
Kathleen Meehan
Douglas J. Nelson
Wensong Yu

June 14, 2013
Blacksburg, Virginia

Keywords: *ac-dc Power Conversion, dc-dc Power Conversion, Maximum Power Point Tracking, Photovoltaic Cells, Photovoltaic Equivalent Circuit, Photovoltaic Source Simulator*

Photovoltaic Source Simulators for Solar Power Conditioning Systems: Design Optimization, Modeling, and Control

Ahmed M. Koran

ABSTRACT

This dissertation presents various systematic design techniques for photovoltaic (PV) source simulators to serve as a convenient tool for the dynamic performance evaluation of solar power conditioning systems and their maximum power point tracking algorithms. A well-designed PV source simulator should accurately emulate the static and the dynamic characteristic of actual PV generator. Four major design features should be adopted in any PV source simulator: (i) high power-stage efficiency, (ii) fast transient response-time, (iii) output impedance matching with actual PV generator, and (iv) precise reference generation technique. Throughout this research, two different PV source simulator systems are designed, modeled, and experimentally verified. The design of the first system focuses mainly on creating new reference generation techniques where the PV equivalent circuit is used to precisely generate the current-voltage reference curves. A novel technique is proposed and implemented with analog components to simplify the reference signal generator and to avoid computation time delays in digital controllers. A two-stage LC output filter is implemented with the switching power-stage to push the resonant frequency higher and thus allowing a higher control-loop bandwidth design while keeping the same switching ripple attenuation as in the conventional one-stage LC output filter. With typical control techniques, the output impedance of the proposed simulator did not

match the closed-loop output impedance of actual PV generator due to the double resonant peaks of the two-stage LC output filter. Design procedures for both control and power-stage circuits are explained. Experimental results verify the steady-state and transient performance of the proposed PV source simulator at around 2.7 kW output.

The design concept of the first simulator system is enhanced with a new type of PV source simulator that incorporates the advantages of both analog and digital based simulators. This simulator is characterized with high power-stage efficiency and fast transient response-time. The proposed system includes a novel three-phase ac-dc dual boost rectifier cascaded with a three-phase dc-dc interleaved buck converter. The selected power-stage topology is highly reliable and efficient. Moreover, the multi-phase dc-dc converter helps improve system transient response-time though producing low output ripple, which makes it adequate for PV source simulators.

The simulator circuitry emulates precisely the static and the dynamic characteristic of actual PV generator under different environmental conditions including different irradiance and temperature levels. Additionally, the system allows for the creation of the partial shading effect on PV characteristic. This dissertation investigates the dynamic performance of commercial and non-commercial solar power conditioning systems using the proposed simulator in steady-state and transient conditions. Closed-loop output impedance of the proposed simulator is verified at different operating conditions. The impedance profile –magnitude and phase- matches the output impedance of actual PV generator closely. Mathematical modeling and experimental validation of the proposed system is thoroughly presented based on a 2.0 kW hardware prototype. The proposed simulator efficiency including the active-front-end rectifier and the converter stages at the maximum power point is 96.4%.

TO MY PARENTS
MOHAMMAD AND FAKEZAR

TO MY SISTERS
NAZEK AND BANAN

TO MY WIFE AND SON
REFAD AND KAREEM

ACKNOWLEDGMENTS

I would like to express my deepest appreciation to my advisor Dr. Jih-Sheng Lai for giving me the opportunity to join the Future Energy Electronics Center (FEEC) at Virginia Tech. His continuous support, guidance, and wise suggestions throughout the course of this research have been always a source of inspiration. I would like to thank my Ph.D. committee members Dr. Kathleen Meehan, Dr. Virgilio Centeno, and Dr. Douglas Nelson for their suggestions and comments. Finally, I would like to thank all current and former FEEC members for their helpful discussions and great support. Special thanks to Mr. Gary Kerr, Mr. Thomas LaBella, Dr. Rae-Young Kim, and Dr. Wensong Yu for their help and support.

TABLE OF CONTENTS

LIST OF FIGURES

LIST OF TABLES

CHAPTER 1

INTRODUCTION

1.1 MOTIVATION

Renewable energy sources are becoming increasingly important recently with focus turning towards clean electricity generation. In particular, photovoltaic (PV) or solar power systems are one of the most promising and attractive renewable energy sources due to their low operational and maintenance costs, pollution free power generation, long life cycles, and noise free operation [1], [2]. Prior to installation, performance and efficiency of solar power conditioning systems have to be evaluated. Moreover, experimental validation and verification of solar power conditioning systems under a wide range of different environmental and load conditions have to be done [3], [4].

Solar or PV cells are used to directly convert sunlight into dc power. PV cells exhibit nonlinear output current-voltage characteristic. This current-voltage curve is characterized with a unique maximum power point (MPP) and depends on environmental conditions (solar irradiance, cell temperature, wind speed, etc…) and PV cell fabrication material [5]-[7]. Accordingly, a maximum power point tracking (MPPT) algorithm is required in solar power conditioning systems in order to maximize the generated output power [8]-[12]. Two existing methods are used to test solar power conditioning systems and their MPPT algorithms. The first method is to test using an actual PV panel with a direct solar irradiance or an adjustable

artificial light. This method is often used for low-power systems as testing medium- and high-power levels with actual PV panel is costly, bulky, and highly dependent on weather conditions. Furthermore, evaluation and comparison of different MPPT techniques requires repeatable weather and load conditions, which is impractical. The second method is to test using a PV source simulator that has a linear or a switching power-stage along with the associated control system. A high-power PV source simulator typically employs a switching-mode dc-dc converter that emulates the static and the dynamic characteristic of actual PV generator at different load and environmental conditions.

Photovoltaic source simulators can be used to study the behavior and the characteristic of different PV cells materials, assess the PV energy production, experimentally investigate the dynamic performance of solar power conditioning systems including stand-alone and grid-connected inverters regardless of environmental conditions, and evaluate different MPPT algorithms' response and efficiency.

The major targets of this dissertation are: (i) propose a flexible PV source simulator to be claimed as a substitute for actual PV generators, (ii) propose new simple, accurate, and flexible reference generation techniques to create the PV reference curve, (iii) match the dynamic and static characteristics of actual PV generators to justify the validity of the proposed PV source simulator, and (iv) utilize the proposed PV source simulator to evaluate the dynamic and static performance of different solar power conditioning systems during startup, steady-state, and transient conditions.

1.2 PHOTOVOLTAIC SOURCE SIMULATORS: BACKGROUND

Photovoltaic source simulators can be classified into different categories based on the design of power-stage, control system, and reference generation technique. Fig. 1.1 summarizes the different classifications of PV source simulators. Power-stage design can be configured with a linear [13], [14] or a switching power-stage. Linear PV source simulators are excellent in dynamic response but limited to low power applications. Low efficiency, high heat generation, and bulky size are serious concerns at high power applications where switching power-stages are more attractive. To replicate the current-voltage characteristic of a PV cell, the switching power-stage should operate in buck mode. Different switching power-stages have been reported as PV source simulators including: single-phase dc-dc buck converter [15], three-phase ac-dc voltage source and current source rectifier [16], half and full bridge dc-dc converter [17], [18], and LLC resonant dc-dc converter [19]. Other power-stages have been used such as a dc programmable power supply with a current limit, dc power supply with a variable resistor [20] or controlled switch resistor [21], and active power load [22].

The current-voltage reference generation techniques can be either analog [23]-[25] or digital based [26]-[28]. The analog based simulators are distinguished with simplicity and low cost implementation. Fig. 1.2 shows the basic structure of analog-based PV source simulators, two control-loops are used: (i) inner-current loop and (ii) outer-reference loop. The inner-current loop aims to control the output current of the PV source simulator to match the reference-current generated by the outer-reference loop. The current-voltage reference curves of analog-based PV source simulators can be employed using analog circuitry in one of three ways: (i) using a small PV cell with a light source [29], (ii) using a photo-diode with a light emitting diode [30], and (iii)

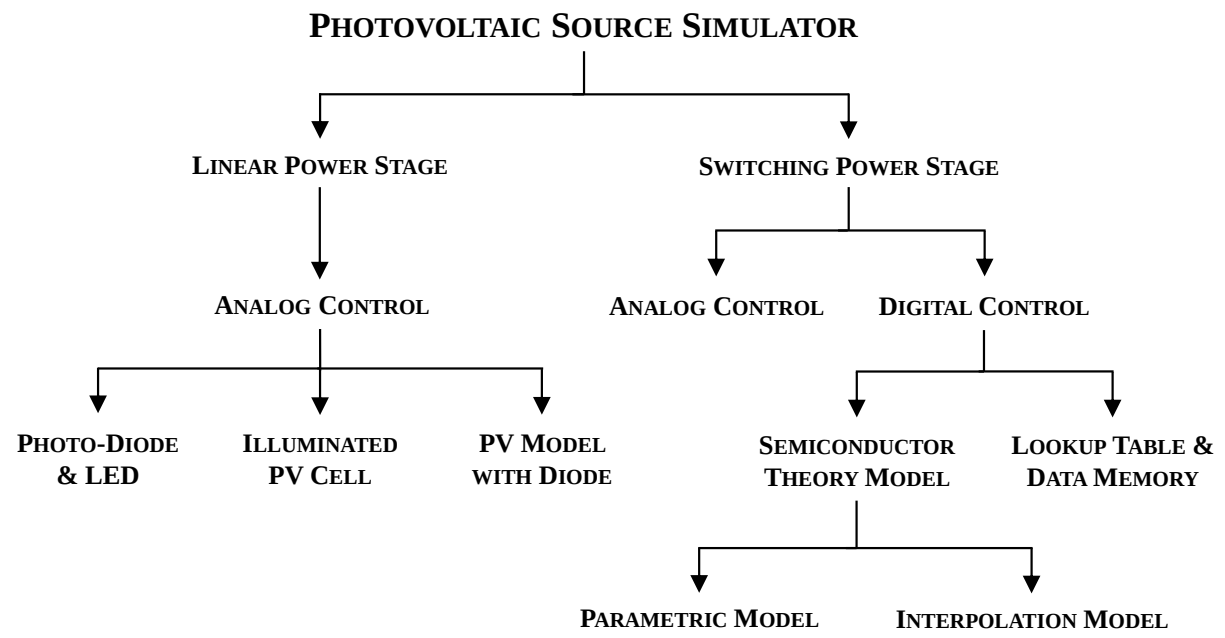

Figure 1.1 Photovoltaic source simulators classification chart

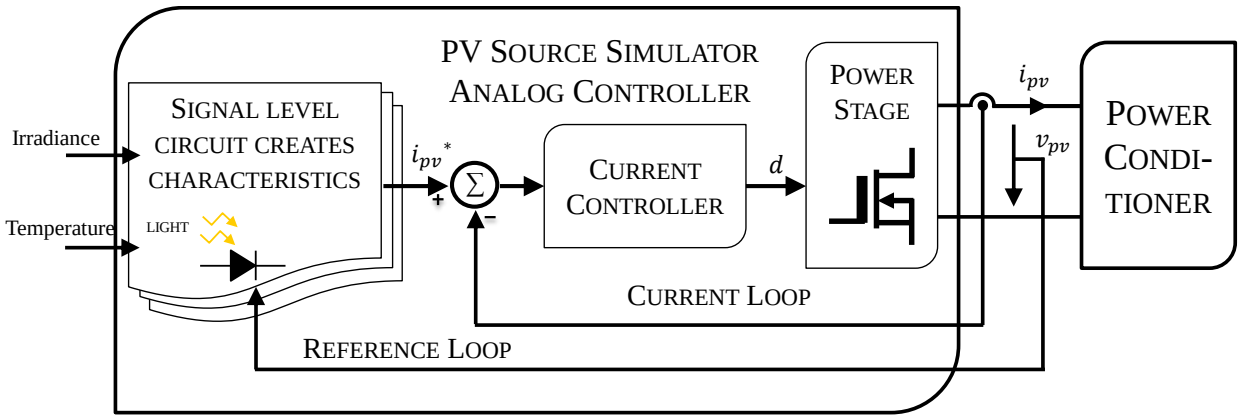

Figure 1.2 Analog-based photovoltaic source simulator basic structure

using a PV cell diode model with current source [31], [32]. The first approach is a real-time simulator [33] and hence, is the most accurate among other approaches. The second approach is flexible and can be used to emulate shading conditions effectively [34]. The implementation of the last approach is simple where the current source represents the sunlight illumination. Digital

reference generation based PV source simulators are flexible, reliable, and less sensitive to high-frequency switching noise. However, the digital time delay may affect the performance and design of control-loops. Fig. 1.3 shows the basic structure of digital-based PV source simulators. The two control-loops are digitally implemented to match the characteristic of actual PV generation systems. The current-voltage digital reference curve of digital-based PV source simulators can be digitally generated using one of two techniques. The first technique is to store pre-measured current-voltage curves in a data memory at different environmental and load conditions [35]-[38]. The more data points stored, the higher the resolution and accuracy the pre-generated characteristic. The second technique is the digital implementation of the mathematical model of PV cells [39]-[40]. A high-speed digital signal processor (DSP) is required due to the execution of sophisticated mathematical semiconductor equations. Two PV models have been widely used: (i) the parametric model and (ii) the interpolation model [41], [42]. The parametric model is used when all PV cell parameters (from manufacturer's data sheets) are known [43], whereas, the interpolation model requires knowledge of the open-circuit voltage, short-circuit current, voltage at the MPP, and current at the MPP [44], [45].

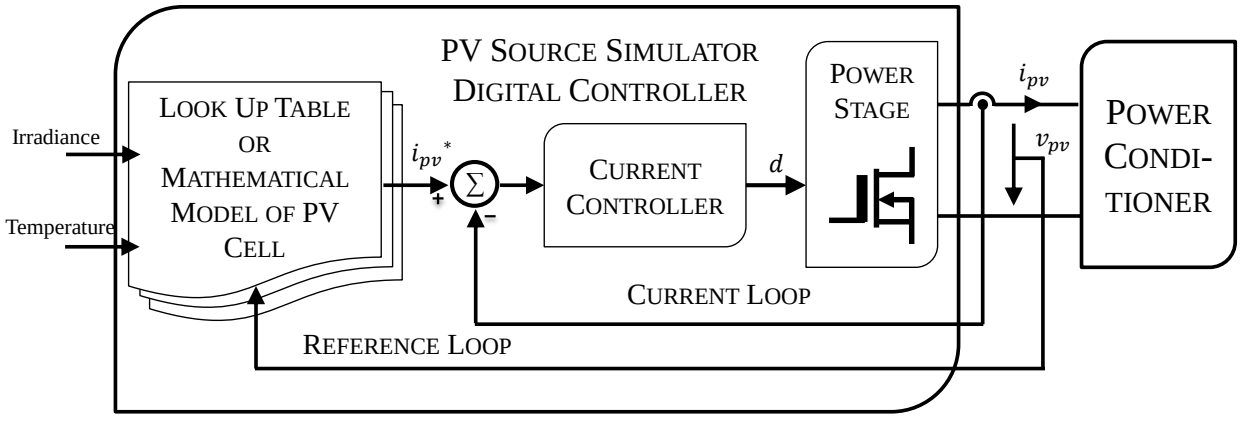

Figure 1.3 Digital-based photovoltaic source simulator basic structure

1.3 PHOTOVOLTAIC SOURCE SIMULATOR DEFINITION

A PV source simulator is a power electronics circuit able to reproduce the static and the dynamic characteristic of an actual PV generator over a wide range of environmental and load conditions. PV source simulators can be cost-effective, compact, and flexible [46]. A well-designed PV source simulator should adopt the following features:

- Accurately predict the output current-voltage and power-voltage characteristic of actual PV generator under different environmental and load conditions.
- Match the frequency response of the output impedance of actual PV generator in high and low-frequency ranges and at different operating conditions including constant current and constant voltage.
- Simulate the PV characteristic under partial shading conditions with multiple peaks and steps.
- Emulate the effect of bypass and blocking diodes on PV output characteristic.
- Reflect the effect of different PV configurations on PV output characteristic.
- Evaluate different MPP tracking algorithms performance and efficiency with reasonable response-time.
- Achieve high power-stage efficiency to be adequate for operations over a long period of equipment testing.
- Interface capability with other power electronics circuits and solar power conditioning systems.
- Evaluate solar power conditioning systems performance in steady-state and transient-state under different load and environmental conditions.

1.4 PHOTOVOLTAIC CELLS STATIC AND DYNAMIC CHARACTERISTICS

A PV cell is basically a p-n semiconductor junction that absorbs the energy of light particles (known as photons) and converts it to direct electric power. If the energy of the photon, which is a factor of its wavelength, is larger than the energy of the p-n junction band gap, the PV cell absorbs the photon energy and an electron is excited from an occupied low energy level in the valance band to an unoccupied higher energy level in the conduction band. The electron moves from the p-type material (minority carriers) to the n-type material of the PV cell to flow through the load. An anti-reflective coating layer is added to the surface of the PV cell to increase the amount of transmitted light through the cell and hence, enhances the quality of light absorption. Fig. 1.4(a) and Fig. 1.4(b) show the basic structure of PV cells. An intrinsic layer is added to extend carriers life-time and therefore increase the optically produced electron-hole pairs [47].

Fig. 1.5(a) and Fig. 1.5(b) show the dc and the ac equivalent circuit models of the PV cell, respectively. The dc circuit represents the static model of the PV cell [48], whereas the ac circuit represents the dynamic model of the PV cell [49]. In Fig. 1.5(a), the current source I_L is the maximum light-generated current through the PV cell, diode D represents the p-n semiconductor junction, resistor R_s is the internal Ohmic resistance of the PV cell, and R_{sh} accounts for stray currents such as leakage and recombination currents. The general equation describing the static current-voltage characteristic of the PV cell under a certain operating temperature T (in Kelvin) and illumination level G (in W/m^2) with parasitic resistances neglected is given in (1.1). The PV cell output current I_{pv} is a function of the p-n junction

saturation current I_0 and the light-generated current I_L, which are expressed as in (1.2) and (1.3), respectively [50].

$$I_{pv} = I_L - I_0 \left\{ exp\left(\frac{q}{nKT} V_{pv}\right) - 1 \right\} \tag{1.1}$$

$$I_0 = I_{0(T_r)} \left\{ exp\left(\frac{-qE_g}{nK\left(\frac{1}{T} - \frac{1}{T_r}\right)} \right) \right\} \left(\frac{T}{T_r}\right)^{\frac{3}{n}} \tag{1.2}$$

$$I_L = I_{L(T_r)}\left(1 + \alpha_{sc}(T - T_r)\right) \tag{1.3}$$

T is the PV cell temperature, T_r is the reference temperature (301.18 K), q is the electron charge (coulombs), n is the ideality factor of the p-n junction, K is Boltzmann constant ($1.3807 * 10^{-23}$ Joule/K), E_g is the band gap energy (eV), $I_{L(T_r)}$ is the light-generated current at the reference temperature, $I_{0(T_r)}$ is the diode saturation current at the reference temperature, and α_{sc} is the short-circuit temperature coefficient (A/sec). In Fig. 1.5(b) the ac equivalent circuit of the PV cell is represented with a passive-like model. Capacitor C_p is the PV cell dynamic capacitance, which is a combination of transition capacitance and diffusion capacitance of the p-n junction, and r_d is the equivalent dynamic resistance of the PV cell. The frequency response of the output impedance of the PV cell based on the ac equivalent model below for the same operating point is constant in the low-frequency range resembling resistive characteristic, and in high-frequency range, the magnitude and phase of the output impedance decreases resembling capacitive characteristic. The output impedance of the PV cell is operating point dependent, it is

high at constant current condition (current source characteristic) and low at constant voltage condition (voltage source characteristic).

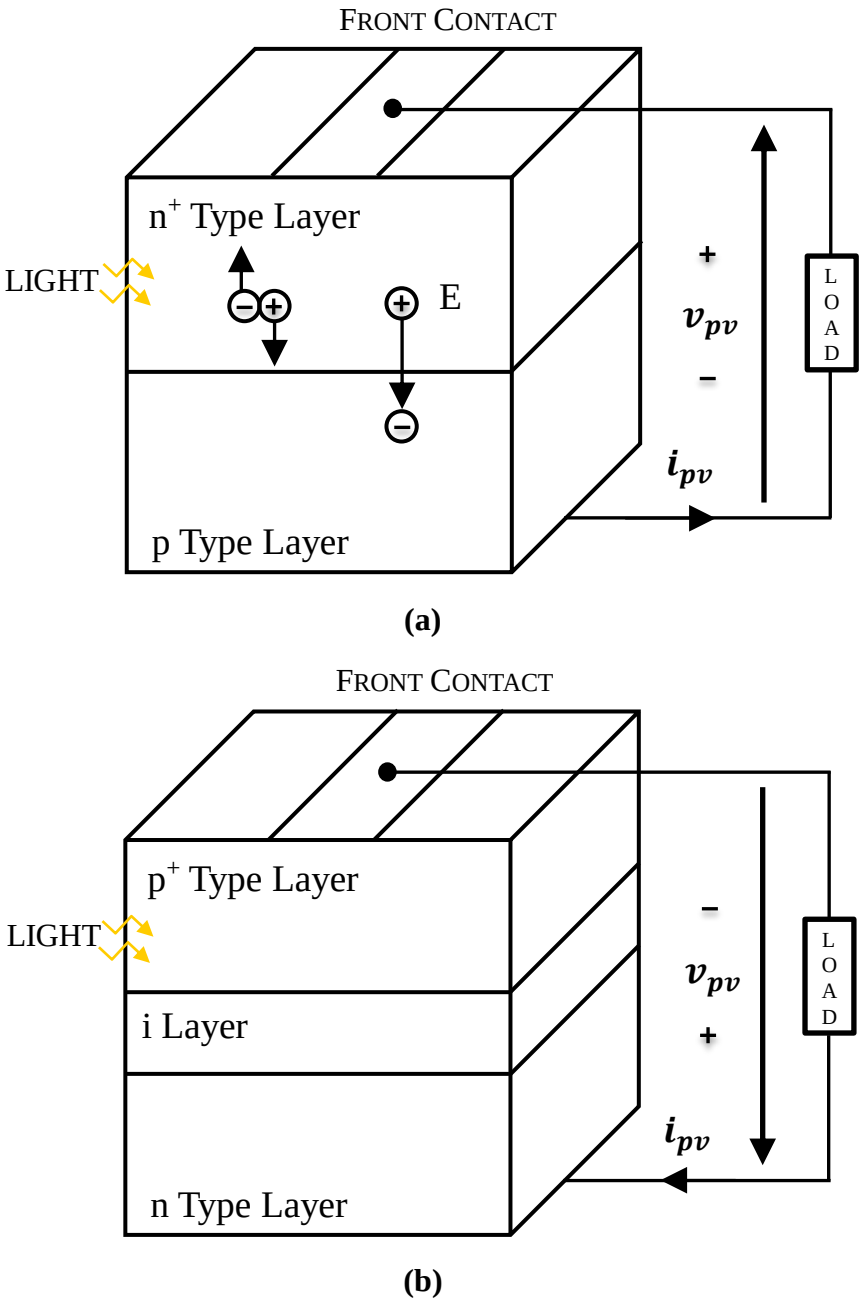

Figure 1.4 Photovoltaic cell basic structure; **(a)** Basic photovoltaic cell and **(b)** Photovoltaic cell with intrinsic layer

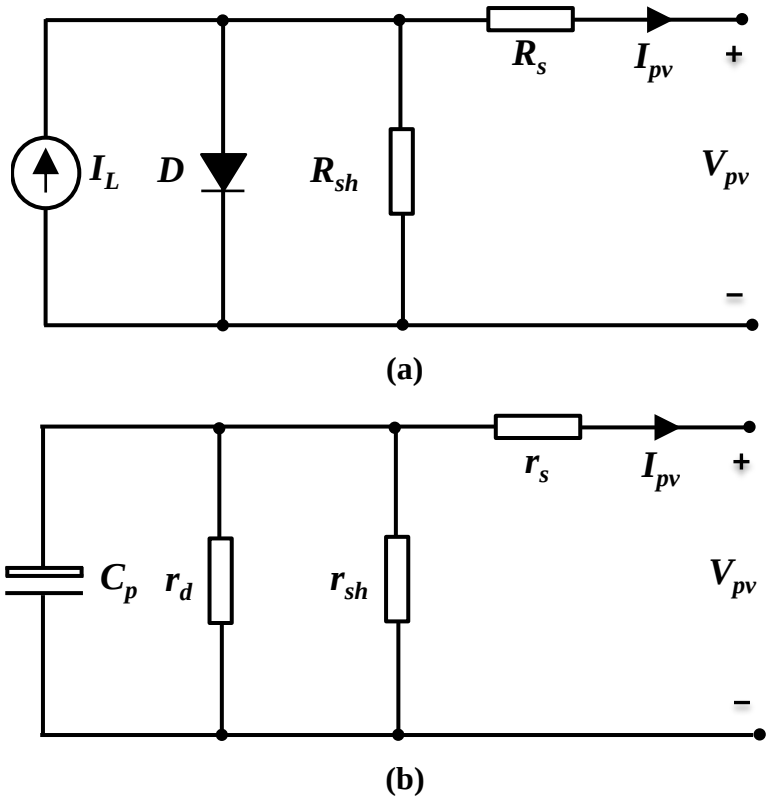

Figure 1.5 Photovoltaic cell equivalent circuit model; **(a)** DC model and **(b)** AC model

Fig 1.6 shows the PV cell current-voltage static characteristic on dark-state and illuminated-state [51]. The characteristic curve can be divided into three operating conditions: (i) constant-current (CC), (ii) maximum power point (MPP), and (iii) constant-voltage (CV). The electrical behavior of the PV cell can be described using three parameters. The first one is the-short-circuit current I_{sc}, which is the current through the PV cell at zero output voltage. The short-circuit current equals the light-generated current when series resistor r_s is neglected. This current is directly proportional to the illumination level of the PV cell. The second parameter is the open-circuit voltage V_{oc} at the terminals of the PV cell, which can be obtained at zero output current. Reverse bias saturation current of the p-n junction determines the PV cell's open-circuit voltage and is inversely proportional to the operating temperature. The open-circuit voltage of

the PV cell at a certain operating temperature and illumination level can be expressed as in (1.4). The third parameter is the fill factor, which is defined as the ratio of the maximum obtainable power of the PV cell to the product of the open-circuit voltage and short-circuit current. This is an important parameter in evaluating the performance of PV cells. Fill factor determines the squareness of the current-voltage curve of the PV cell

$$V_{oc} = V_{oc(T_r)}\big(1 - \beta_{oc}(T - T_r)\big) \tag{1.4}$$

$V_{oc(T_r)}$ is the open-circuit voltage at reference temperature and β_{oc} is the open-circuit temperature coefficient (V/sec).

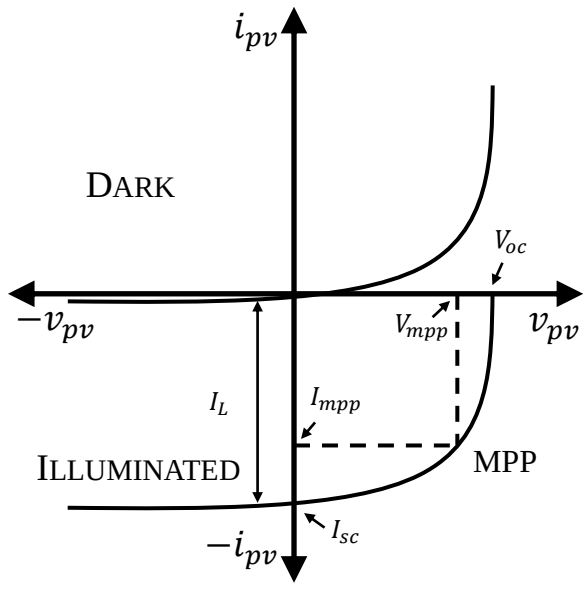

Figure 1.6 The basic photovoltaic cell current-voltage characteristic under dark-state and illuminated-state

1.5 MAXIMUM POWER POINT TRACKING

The nonlinear current-voltage characteristic of PV cells is characterized with a unique MPP, which is highly dependent on weather and load conditions. An MPPT algorithm is an analog or digital based technique allows the PV cell to operate at the MPP at any given environmental conditions. MPPT controllers or algorithms are integrated with solar power conditioning systems to maximize the output power extracted from PV generator. Various MPPT techniques have been proposed including, perturbation and observation (P&O) [52], incremental conductance [53], fractional open-circuit voltage [54], fractional short-circuit current [55], fuzzy logic controller [56], neural network [57], ripple correlation control [58], and dc link capacitor droop control [59].

The perturbation and observation method is the most commonly implemented technique among other algorithms although oscillations around the MPP can occur. In this technique, the controller adjusts the output voltage of the PV cell based on its instantaneous output power. The incremental conductance algorithm uses the slope of the power-voltage curve of the PV cell ($\Delta P/\Delta V$) to determine the voltage reference. The derivative of the cell output power with respect to the cell output voltage at the MPP is zero. This method requires more computations relative to the P&O but may reach the MPP faster. Different MPPT techniques can be evaluated based on their, periodic time, convergence speed, implementation complexity, and sensed parameters. Due to the numerous number of MPPT algorithms, it is not clear for PV system designers on how to choose the algorithm that fits with their application. Authors in [60] presented a complete comparison among different MPPT techniques to help PV system designers to select the MPPT algorithm that suits their application requirements.

1.6 MAJOR CONTRIBUTIONS AND DISSERTATION OUTLINE

This dissertation presents the design, modeling, and control PV source simulators to be used in solar power conditioning systems evaluation. Two novel PV source simulators have been proposed throughout the dissertation to emulate the static and the dynamic characteristic of actual PV generator and to evaluate the dynamic performance of solar power conditioning systems and their MPP tracking algorithms in steady-state and transient conditions. The first simulator system is an analog-based simulator where a novel technique is proposed and implemented with analog components to simplify the reference signal generator and to avoid computation time delays in digital controllers. This design is enhanced to propose the second simulator system, which incorporates the advantages of both analog and digital based simulators where a new power-stage circuit has been proposed and implemented. High power-stage efficiency and fast transient response-time have been achieved as compared to commercial PV source simulators and to the ones in literature.

In the first design, a novel analog technique is proposed to emulate the static and the dynamic characteristic of actual PV generator. The PV equivalent circuit is implemented with an analog circuit using high-bandwidth voltage-controlled current-source and voltage-controlled voltage-source. The generated current-voltage reference curves are highly precise with more than 20 kHz control-loop bandwidth. The proposed PV source simulator has the following features:

- Power-stage uses a switch-mode dc-dc converter to allow high-voltage and high-current outputs.

- Output voltage and current follow the reference curve precisely with desired conversion ratios by the use of a simple and conventional controller.
- Reasonably fast output response-time without distortion under the irradiance perturbation condition with frequency below 40 Hz.
- No need to provide a light source for different irradiance level testing because of the use of the voltage-controlled current-source loop.
- A two-stage LC filter allows ripple-free output and high cut-off frequency for fast loop bandwidth design.
- Simple and low cost implementation for PV equivalent circuit and power-stage of the single-phase dc-dc converter.
- Closed-loop output impedance closely matches the actual PV generator impedance in low-frequency range and at different operating regions.

The second simulator system is a hybrid-based PV source simulator that combines the advantages of both analog and digital based simulators. The proposed two-stage PV source simulator is characterized with high power-stage efficiency and fast transient response-time. Therefore, the proposed system is adequate for solar power conditioning systems evaluation. The proposed PV source simulator has the following features:

- Novel two-stage switching power circuits including a high reliable three-phase ac-dc dual boost rectifier cascaded with a three-phase dc-dc interleaved buck converter.
- Analog extraction of reference curves using an actual PV cell with an adjustable light source for a precise, simple, and flexible operation.
- Hybrid control system implementation combines the advantages of both analog and digital based simulators to minimize digital computation times.

- Accurately predict the static current-voltage and power-voltage characteristic of actual PV generator under different load and environmental conditions.
- Successfully emulate the partial shading effect on the static characteristic of actual PV generator including multiple steps and peaks.
- Closed-loop output impedance of the simulator closely matches the impedance of the actual PV generator at different operating zones including constant current and constant voltage.
- High power-stage efficiency including the ac-dc rectifier and the dc-dc converter compared to commercial products and to PV source simulators in literature, which makes it adequate for operations over a long period of equipment testing.
- Fast transient response-time relative to MPP tracking algorithms.

This dissertation titled 'Photovoltaic source simulators for solar power conditioning systems: design optimization, modeling, and control' consists of five main chapters organized in the following sequence:

Chapter 1 gives a detailed introduction of the research motivation and background. PV source simulators should precisely emulate the static and the dynamic characteristic of PV generator using a power electronics circuit along with its associated control system. Precise reference curve, output impedance matching, high power-stage efficiency, and fast transient response-time are the main concerns when designing a PV source simulator. A detailed classification of PV source simulators based on power-stage, control system, and reference generation technique is presented. PV cell basics and the operation of different MPPT algorithms are included. At last, research objectives along with major contributions are summarized.

Chapter 2 introduces the design of an analog-based PV source simulator. The simulator is characterized with two features: (i) novel reference generation circuit and (ii) two-stage LC filter. The reference circuit is experimentally built using analog components based on the PV equivalent circuit. Frequency response of the VCVS and the VCCS is measured and a high control-loop bandwidth is designed. Two reference circuits are proposed: (i) reference circuit using diodes and (ii) reference circuit using an un-illuminated PV cell. The two-stage LC filter allows the control-loop bandwidth to be improved while maintaining low output ripple.

Chapter 3 presents the design of a high efficiency PV source simulator with fast response-time. The proposed simulator is adequate for the evaluation of solar power conditioning systems and their MPPT algorithms. The power-stage circuit includes: (i) three-phase ac-dc dual boost rectifier and (ii) three-phase dc-dc interleaved buck converter. The rectifier stage is a new type of dual boost circuits that is highly reliable and efficient. The converter stage helps improve control-loop bandwidth with low output ripple. Detailed control system derivation and experimental results are presented.

Chapter 4 includes three main topics: (i) closed-loop output impedance of PV source simulators, (ii) evaluation of dynamic performance of solar power conditioning systems using PV source simulator, and (iii) evaluation of dynamic performance of solar power conditioning systems using actual PV generator. The measured and simulated closed-loop output impedance of the proposed simulator systems is presented and compared to the impedance of actual PV generator. Detailed experimental waveforms of different solar power conditioning systems connected to the proposed PV source simulators and to actual PV generator are included.

Chapter 5 includes a summary of conclusions and suggests future works, where the design of the PV source simulators can be further improved.

CHAPTER 2

DESIGN OF ANALOG-BASED PHOTOVOLTAIC SOURCE SIMULATOR WITH A NOVEL REFERENCE SIGNAL GENERATOR AND TWO-STAGE LC FILTER

2.1 INTRODUCTION

This chapter focuses in creating new reference generation techniques for PV source simulators characterized with simplicity, accuracy, and flexibility. A PV source simulator using a novel analog controller and a two-stage LC output filter is proposed because the conventional single-stage LC filter with low cut-off frequency will limit the overall system control-loop bandwidth. The PV source simulator consists of a PV equivalent circuit to produce the reference current-voltage characteristic curve and a single-phase dc-dc buck converter to amplify it for high-power applications. A novel analog technique is proposed to emulate the PV equivalent circuit, which consists of a voltage-controlled current-source (VCCS), a voltage-controlled voltage-source (VCVS), a series connected diode stack or an actual un-illuminated PV cell, and a resistor network. This equivalent circuit is closed-loop controlled and can generate a reference with higher than 20 kHz bandwidth. The single-phase dc-dc buck converter takes the reference signal and amplifies it with pulse width modulator (PWM) to produce high-voltage and high-current at the output, which is then filtered by the proposed two-stage LC output filter. Because the two-stage LC filter's resonant frequency is high, the control-loop bandwidth can be improved while maintaining the same switching ripple attenuation as compared to that of the one-stage LC output filter. This chapter describes the design procedure in detail. Measured frequency domain

response of the PV equivalent circuit, hardware setup, and experimental results will be shown to verify the design concept.

2.2 SYSTEM DESCRIPTION AND CONTROL STRATEGY

The entire system block diagram is shown in Fig. 2.1. There are three major circuit sections: (i) PV equivalent circuit, (ii) control system circuit, and (iii) power-stage circuit. The PV equivalent circuit consisting of a VCCS loop and a VCVS loop produces the current-voltage reference curve and feeds it to the power-stage circuit to amplify it for high-power applications through the analog control system circuit. The power-stage circuit is a single-phase dc-dc buck converter switching stage along with a two-stage LC output filter.

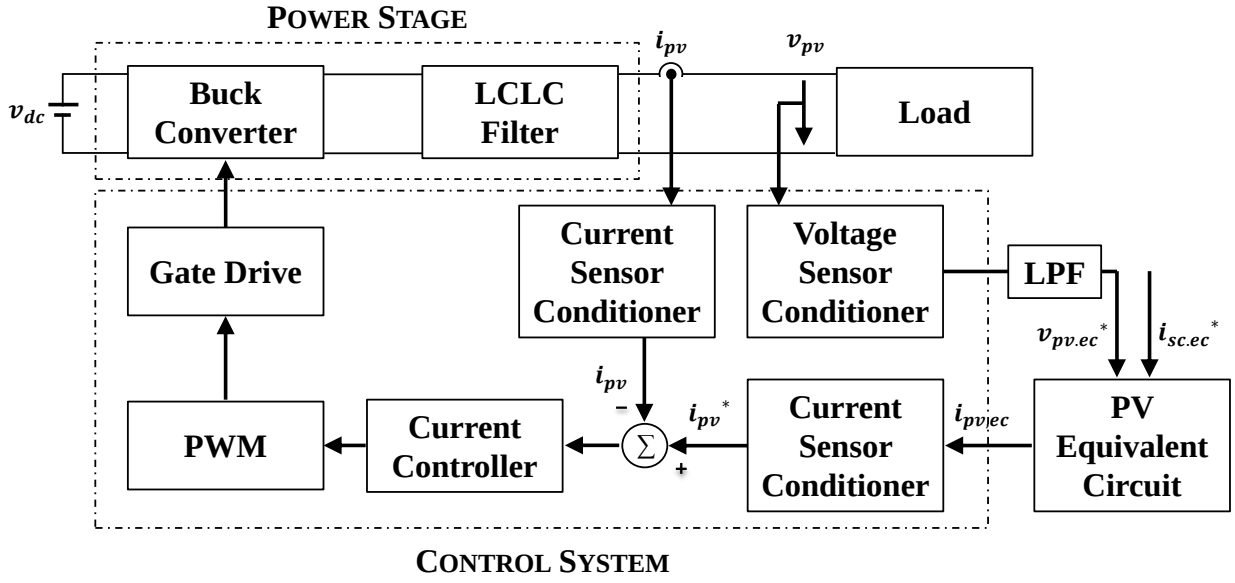

Figure 2.1 The proposed PV source simulator entire system block diagram

Fig. 2.2 shows the control system block diagram of the proposed PV source simulator. There are two analog control-loops: (i) inner-current loop and (ii) outer-reference loop. The inner-current loop aims to control the output current i_{pv} of the power-stage and achieves fast dynamic response to load and disturbance variations. The outer-reference loop contains two cascaded controllers, the first one is associated with the PV equivalent circuit where it senses the output voltage v_{pv} of the power-stage and feeds it back to the PV equivalent circuit. This circuit along with its associated control system generates a reference current $i_{pv,ec}$ that will force the power-stage to produce an actual PV current-voltage reference curve. The second controller of the outer-reference loop is a low pass filter that is added to control and limit the overall control-loop bandwidth of the system. For stability consideration, the inner-current loop should be faster than the outer-reference loop. Conditioning circuit gains h_1, h_2, and h_3 determine the voltage and current values of the power-stage. R represents is the equivalent load resistance of the power conditioning system. The detailed design procedure for both loops will be discussed in the next section.

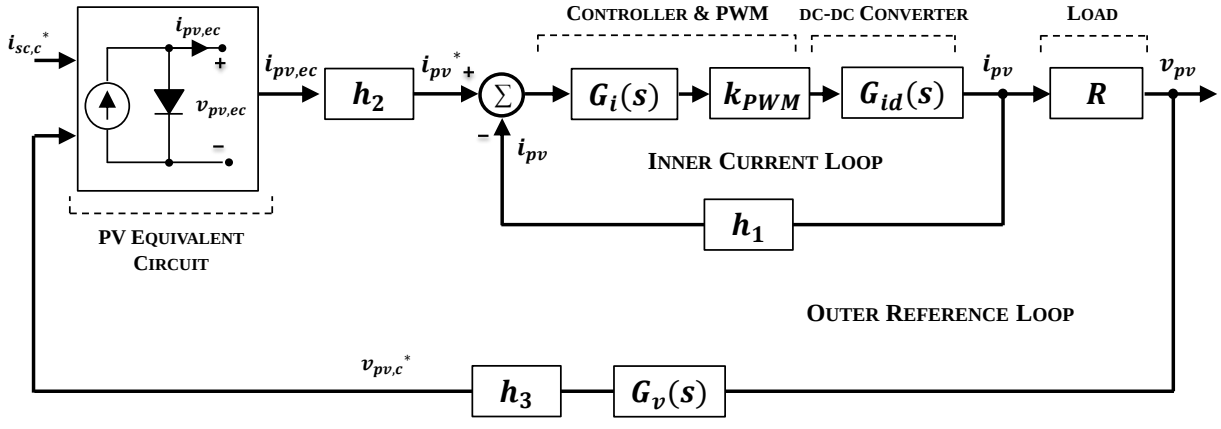

Figure 2.2 Control system block diagram of the proposed PV source simulator

2.3 DESIGN PROCEDURE AND SYSTEM CONFIGURATION

2.3.1 PHOTOVOLTAIC EQUIVALENT CIRCUIT DESIGN WITH DIODES

A PV equivalent circuit model is shown in Fig. 2.3. This single-diode equivalent circuit is characterized with simplicity and accuracy. Different models have been proposed as the two-diode model and three-diode model to precisely present the electrical behavior of the PV cells and arrays of cells. In single diode-model, the current source $I_{sc,ec}$ is proportional to the solar irradiance (W/m^2), and diode D is a typical pn junction diode. Resistor R_{sh} represents the leakage current along the cell borders and localized short circuits whereas resistor R_s represents the resistive paths through the semiconductor material and contacts [61]. The current-voltage characteristic of this circuit can be designed to match an actual PV cell or arrays of cells with proper diode and resistors selection.

Fig. 2.4 illustrates the experimental version of the PV equivalent circuit. The circuit shown in Fig. 2.3 is experimentally built with analog components to generate the current-voltage output reference curves. Current source $I_{sc,ec}$ is represented by a voltage-controlled current-source (VCCS) loop. Metal oxide semiconductor field effect transistor (MOSFET) T_1 operates in the linear region so current $I_{sc,ec}$ will be controlled to follow the current reference $I_{sc,ec}{}^*$. In the voltage-controlled voltage-source (VCVS) loop, MOSFET T_2 operates in the linear region as well to control the output terminal voltage of the PV equivalent circuit $V_{pv,ec}$. This loop determines the operating point of the PV source simulator along the current-voltage characteristic curve. With the use of VCCS loop, there is no need to use an external light source. As for the diode D, its current-voltage characteristic affects the generated PV reference curve.

Therefore, it should be carefully selected to match with characteristic of actual PV generator. In this design, four series-connected diodes (Model number: S2M-13) with 1.5 A forward current were used in the experimental PV equivalent circuit.

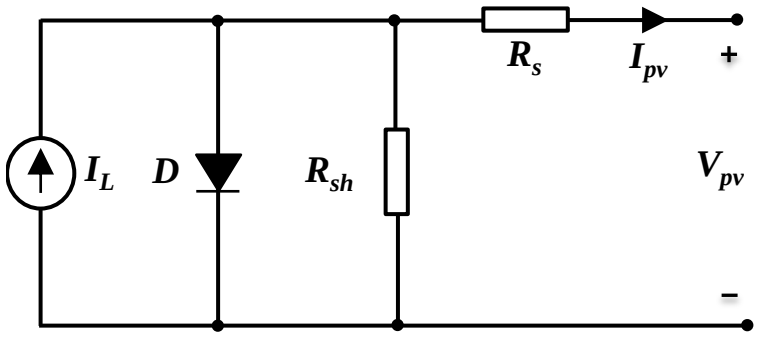

Figure 2.3 Single-diode photovoltaic equivalent circuit model

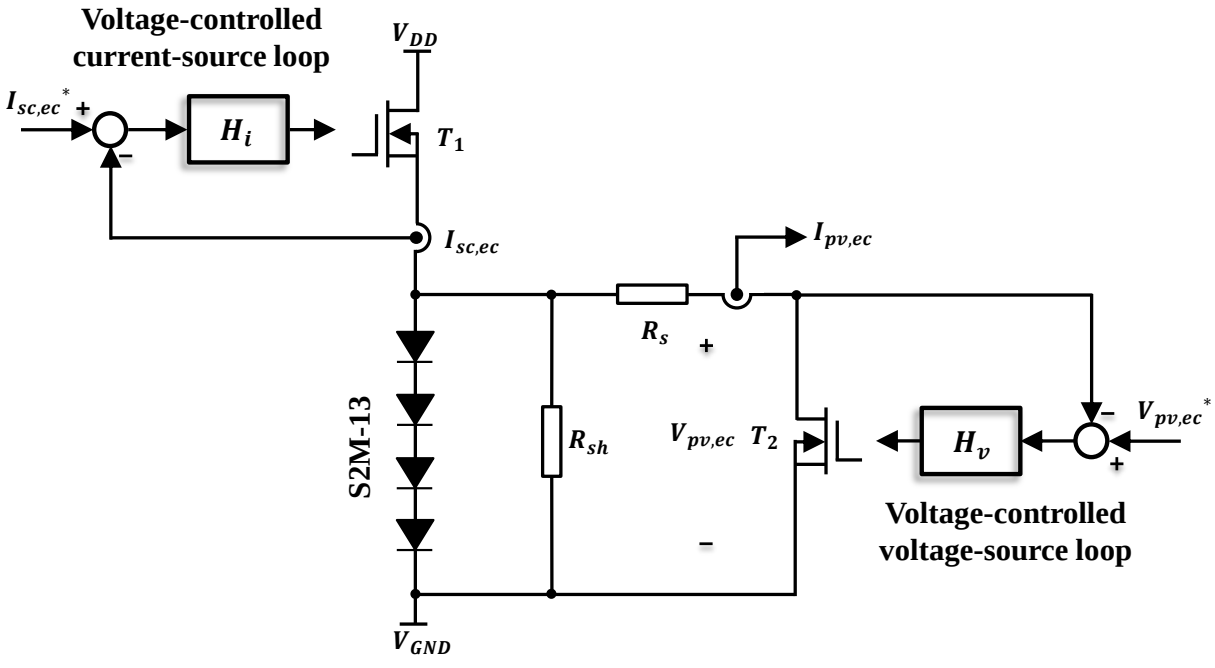

Figure 2.4 Experimental implementation of photovoltaic equivalent circuit with diodes

A high control-loop bandwidth for both the VCCS loop and the VCVS loop should allow decoupling between the reference signal generation circuit and the outer-reference loop dynamics. Fig. 2.5(a) and Fig. 2.5(b) show the measured compensated loop gain for both the VCCS loop and the VCVS loop, respectively. The loop gains were measured using a frequency response analyzer with advanced digital signal processing (Model: 3120 Analyzer). The VCCS loop was designed to have a cross-over frequency of 90 kHz (one-tenth of the operational amplifier bandwidth) and 60^o phase margin, whereas the VCVS loop was designed to have 20 kHz cross-over frequency with 50^o phase margin (one-sixth of the VCCS bandwidth). Since the performance of the VCCS loop affects the desired magnitude and response of output current of the PV source simulator i_{pv}, its control-loop bandwidth should be faster than that of the VCVS loop.

The VCCS loop controller $H_i(s)$ consists of an integrator and a set of double poles and double zeros, which is known as "type 3" controller. The VCVS loop controller $H_v(s)$ consists of an integrator and a set of pole and zero, which is known as "type 2" controller [62]. Using the controller circuit parameters obtained from the above design, a hardware circuit that emulates PV current-voltage characteristic is experimentally built and tested. Fig. 2.6(a) and Fig. 2.6(b) show the experimental results of the experimental current-voltage and power-voltage reference curves using the PV equivalent circuit shown in Fig. 2.4 at different irradiance levels, respectively. Moreover, by changing the PV equivalent circuit parameters (diode and resistors), any type of PV cells can be emulated. Fig. 2.6(c) and Fig. 2.6(d) show three different experimental current-voltage and power-voltage curves implementing the PV equivalent circuit with diodes at different series resistor values. Table 2-1 summarizes the parameters of the designed analog controllers of the VCCS loop and VCVS loop associated with the PV equivalent circuit.

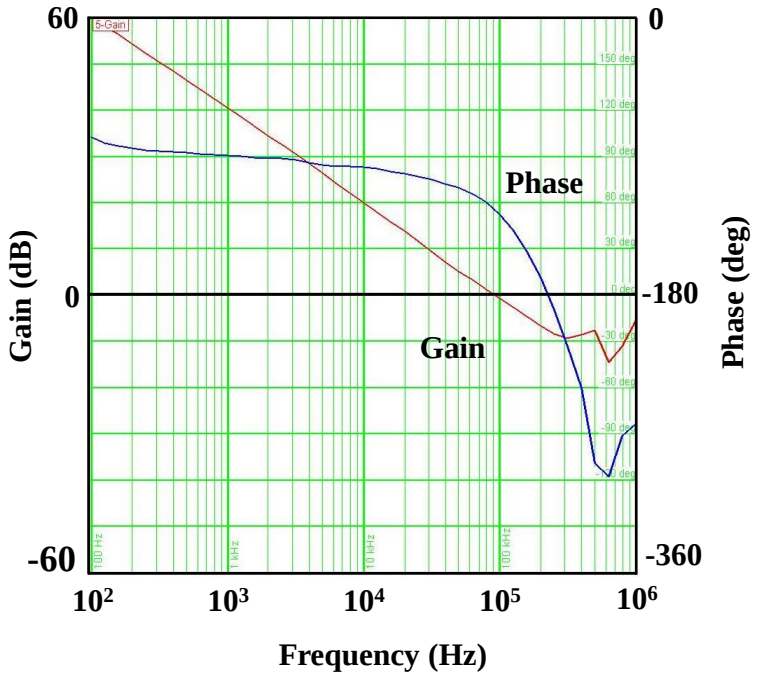

(a)

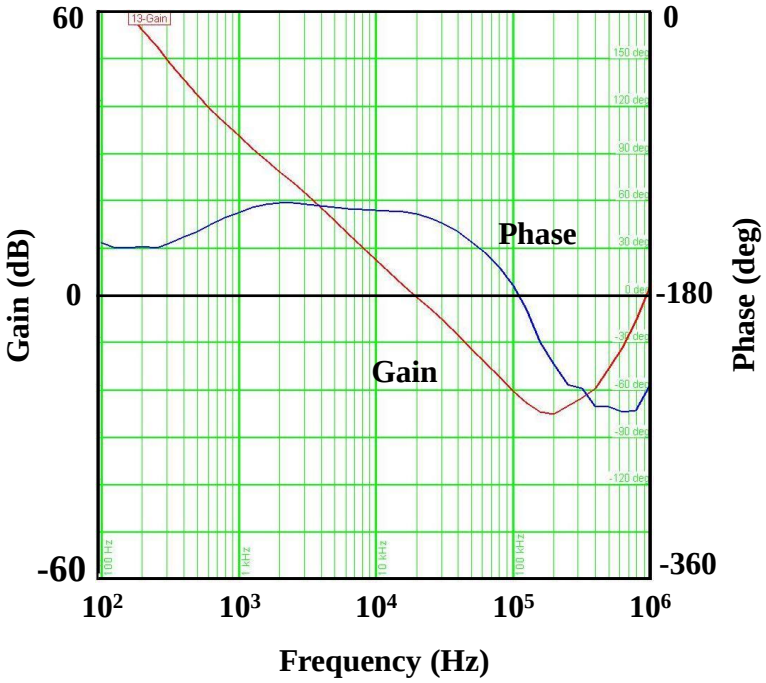

(b)

Figure 2.5 Measured compensated loop gain; **(a)** Voltage-controlled current-source loop and **(b)** Voltage-controlled voltage-source loop

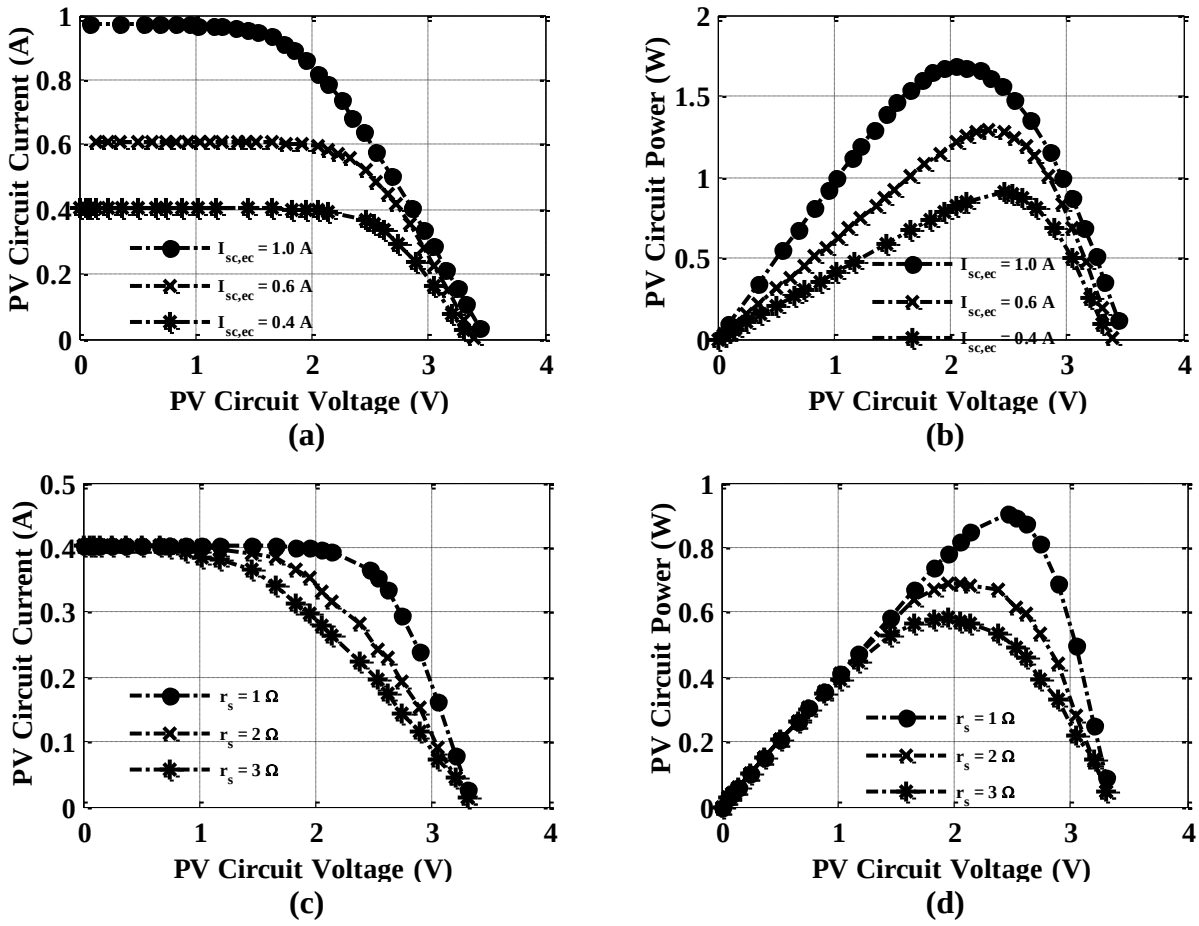

Figure 2.6 Reference curves with diodes; **(a)** Current-voltage at different irradiances, **(b)** Power-voltage at different irradiances, **(c)** Current-voltage with different series resistor values, and **(d)** Power-voltage with different series resistor values

Table 2-1 DESIGNED CONTROLLERS PARAMETERS OF PV EQUIVALENT CIRCUIT

PV Equivalent Circuit		
Control-Loop	Controller Format	Design Parameters
VCCS Controller $H_i(s)$	$k\frac{(s/\omega_{z1}+1)(s/\omega_{z2}+1)}{s(s/\omega_{p1}+1)(s/\omega_{p2}+1)}$	$k = 207.9\ k$ $\omega_{z1} = 29.069\ krad/s$ $\omega_{z2} = 595.20\ krad/s$ $\omega_{p1} = 73.529\ krad/s$ $\omega_{p2} = 1001.1\ krad/s$
VCVS Controller $H_v(s)$	$k\frac{(s/\omega_{z}+1)}{s(s/\omega_{p}+1)}$	$k = 42.19\ k$ $\omega_{z} = 71.43\ krad/s$ $\omega_{z} = 86.81\ krad/s$

2.3.2 PHOTOVOLTAIC EQUIVALENT CIRCUIT DESIGN WITH ACTUAL PV CELL

Another approach to emulate the PV characteristic is to use an actual un-illuminated PV cell as a reference signal generator with no light source. Fig. 2.7 represents the PV equivalent circuit of this approach. This circuit is obtained by the equivalent transformation of the circuit in Fig. 2.3 using Thévenin's theorem. The left part of the circuit consists of a diode D and resistors R_{sh} and R_s. This part is equivalent to the PV equivalent circuit with $I_{sc,ec} = 0$. Therefore, this part can be implemented with actual PV cell under no illumination or in total darkness, while the current source $I_{sc,ec}$ is produced with an external VCCS circuit to represent the light source. In this case, there is no need for any external light source, similar to the previous case using series diodes to emulate the PV cell characteristic. Fig. 2.8 illustrates the experimental version of this PV equivalent circuit with the use of a small un-illuminated PV cell. The circuit is built with analog components to generate the current-voltage reference characteristic curves. This technique is easier to generate the current-voltage characteristic of a specific PV cell than the previous one, which uses diode and resistors network. However, the current-voltage characteristic of the circuit in Fig. 2.8 depends on the selected PV cell material and is for some materials slightly different from actual characteristic with irradiance because the current-voltage characteristic of the diode D depends on the irradiance level. The carrier concentration in the PV cell becomes higher with the increase of the irradiance level, which affects the PV current-voltage characteristic curve [63]. Moreover, the PV equivalent circuit is an approximation model of the actual PV cell. Different PV materials can be tested using this circuit, which is beyond the focus of this study.

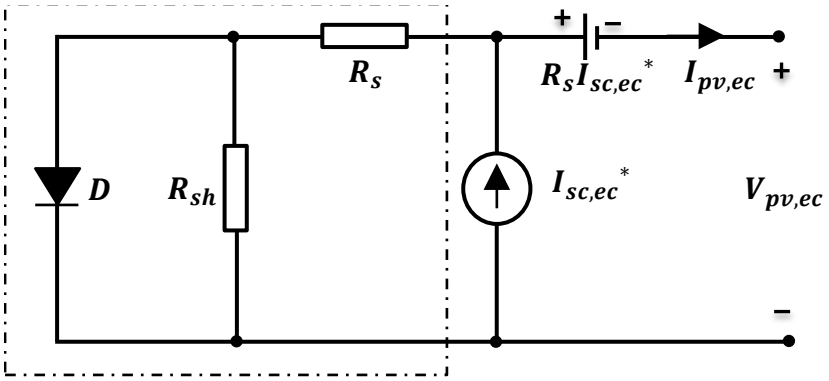

Figure 2.7 Photovoltaic equivalent circuit transformed from the conventional photovoltaic equivalent circuit shown in Figure 2.3

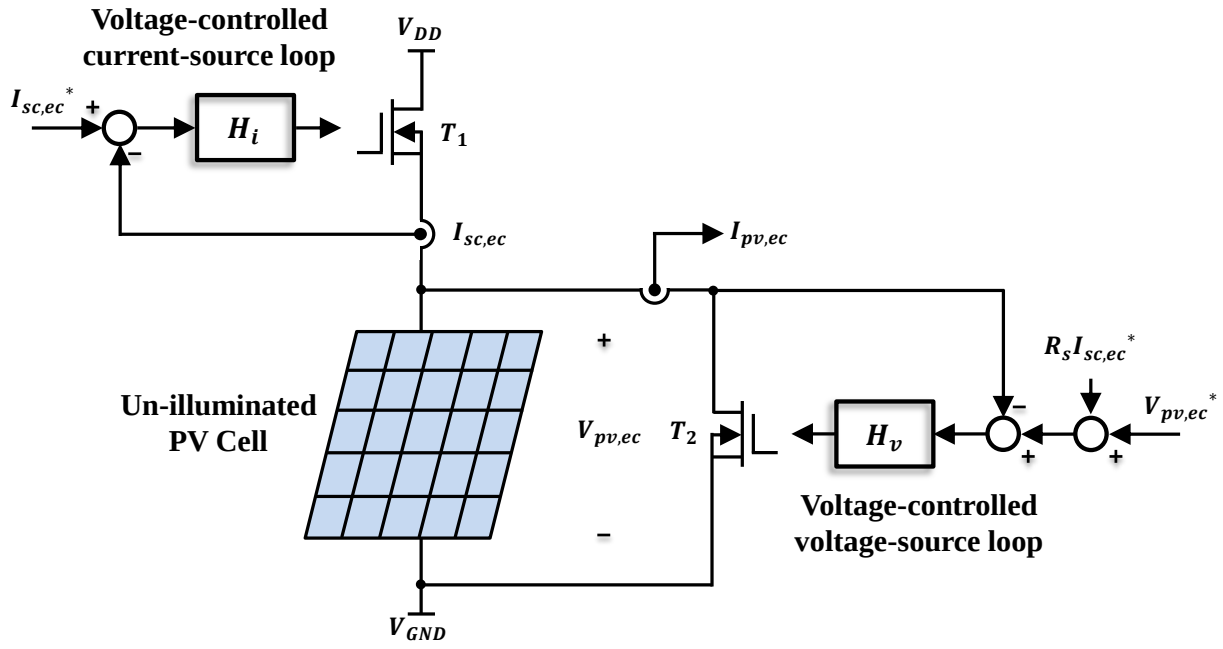

Figure 2.8 Experimental implementation of photovoltaic equivalent circuit with actual un-illuminated photovoltaic cell

Fig. 2.9 shows the current-voltage and power-voltage reference characteristic curve that is generated by the experimental PV equivalent circuit using a single un-illuminated

polycrystalline PV cell. Through estimation, a 1.0 V voltage source was added to represent $R_s I_{sc,ec}$, while $I_{sc,ec}{}^*$ was controlled to be 0.4 A. Bear in mind, in case of polycrystalline PV cells this characteristic is not exactly same as that of the PV cell under illuminated condition, but it shows a similar characteristic of a PV cell and can be used for MPP controller testing and evaluation.

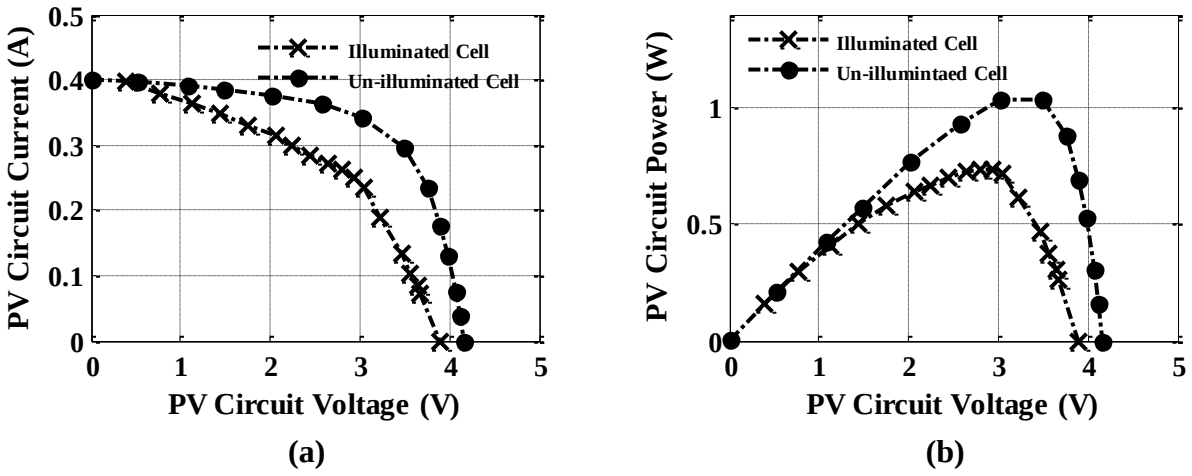

Figure 2.9 Experimental reference curve with the un-illuminated PV cell model; **(a)** Current-voltage and **(b)** Power-voltage

2.4 POWER STAGE AND CONTROL SYSTEM DESIGN

The power-stage circuit is a single-phase dc-dc buck converter with two-stage LC output filter, as shown in Fig. 2.10. IXYS's insulated gate bipolar transistor (IGBT) module (Model: VIO 160-12P1) with a rating of 1200 V and 160 A is selected as the power-stage switching device for its positive temperature coefficient and reduced protection circuit. IXYS's Fast recovery epitaxial diode (Model: VIO 160-12P1) is selected as the main switching diode for its fast reverse recovery and low-voltage drop. The power-stage switching frequency is 30 kHz. A two-stage LC output filter is used to increase the system control-loop bandwidth while attenuating the same switching ripple as with a one-stage LC filter. The cut-off frequency of the filter is designed at around 3 kHz to provide 55 dB attenuation for the 30 kHz switching frequency. To achieve the same attenuation with one-stage LC output filter, the required cut-off frequency is 1 kHz. Fig. 2.11 shows the frequency response comparison of one-stage and two-stage LC filters with a resistive load. Filter inductor L_1 is designed in continuous conduction mode to allow 30% peak-to-peak current ripple. Three stackable toroid powder cores with 26μ permeability (Model: Kool Mμ 77191A) has been selected to obtain the required inductance value. The second inductor current is designed based on filter's cut-off frequency. Both inductors have been built using Litz-wire (AWG# 11) to reduce skin effect and proximity effect at high-frequency. Internal dc resistance of each inductor was 30 mΩ. Filter capacitors C_1 and C_2 are designed to achieve the required cut-off frequency of 3 kHz and meet the desired ripple attenuation at the switching frequency. Polypropylene metalized film capacitors are chosen for dc filtering due to their good frequency characteristic and low dissipation factor. Capacitor C_1 (Model: B3274D4475K) with 450 V rating and 5 mΩ equivalent series resistor and capacitor C_2

(Model: 930C4W1K-F) with 400 V rating and 27 mΩ equivalent series resistor was selected. Table 2-2 shows the switching power-stage technical specifications.

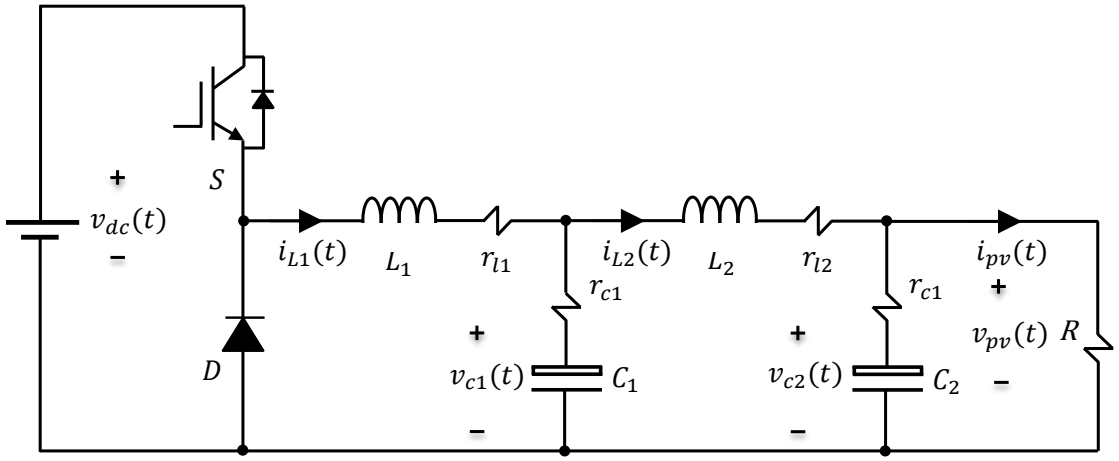

Figure 2.10 Circuit diagram of single-phase dc-dc buck converter with two-stage LC output filter

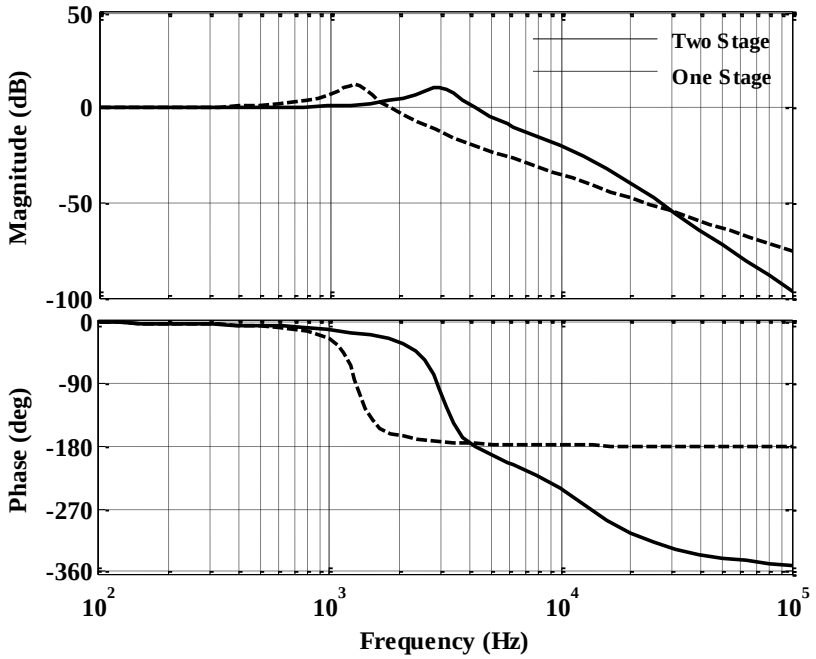

Figure 2.11 Frequency response comparison between one-stage and two-stage LC output filters with resistive load

Table 2-2 TECHNICAL SPECIFICATIONS OF THE PROPOSED PV SOURCE SIMULATOR

dc-dc Converter Stage (Buck)			
Electrical Specifications		Component Parameters	
Input Voltage	300 V	Inductance L_1	300 μH
Output Voltage	(0-250) V	Inductance L_2	300 μH
Output Current	(0-20) A	Capacitance C_1	4.7 μF
OC Voltage	250 V	Capacitance C_2	1.0 μF
SC Current	20 A	Main Switch	VIO 160-12P1
Switching Time	33.3 μs	Main Diode	VIO 160-12P1

Modeling of the dc-dc buck converter helps to predict steady-state solutions, derive small-signal transfer functions, predict transient response behavior, and design linear and nonlinear controllers. To design the control system; three models have to be derived: (i) the switching model, (ii) the large-signal model, and (iii) the small-signal model. The switching model is a time dependent model consists of two sub-circuits: (i) on-time sub-circuit, and (ii) off-time sub-circuit. Based on these two sub-circuits the state space representation of the switching model of the single-phase buck converter with two-stage filter is obtained as in (2.1) and (2.2). The second step is to convert the switching model by combining the two sub-circuits into a time independent model using averaging techniques; this model is the large-signal model and is expressed as in (2.3). Fig. 2.12 shows the equivalent circuit diagram of the large-signal model of the single-phase dc-dc buck converter with two-stage filter. To simplify the mathematical operations the equivalent load resistor R is assumed to be much larger than the equivalent series resistor of the filter capacitor r_{C_2}. The last step is to convert the large-signal model into a linear small-signal model around an equilibrium point where the state-variables and the input-variables are represented with the quiescent variables and small ac variations, ($\vec{x}(t) = X + \tilde{x}(t)$). Throughout this work, $\vec{x}(t)$ represents the average value of the quantity $x(t)$, $\tilde{x}(t)$ represents the small ac variations of the quantity $x(t)$, and X represents the steady-state value of the

quantity $x(t)$. Equation (2.4) illustrates state space representation of the small-signal model of the single-phase buck converter with two-stage filter, whereas Fig. 2.13 shows its equivalent circuit diagram. The forth order control to output-current small-signal transfer function is derived based on the small-signal model as in (2.5) neglecting circuit parasitics and second order ac variations.

$$\frac{d}{dt}\begin{bmatrix} i_{L_1}(t) \\ v_{C_1}(t) \\ i_{L_2}(t) \\ v_{C_2}(t) \end{bmatrix} = \begin{bmatrix} \frac{-r_{l_1}-r_{c_1}}{L_1} & -\frac{1}{L_1} & \frac{r_{c_1}}{L_1} & 0 \\ \frac{1}{C_1} & 0 & -\frac{1}{C_1} & 0 \\ \frac{r_{c_1}}{L_2} & \frac{1}{L_2} & \frac{r_{c_1}+r_{l_2}-r_{c_2}}{L_2} & \frac{1}{L_2} \\ 0 & \frac{1}{C_2} & 0 & -\frac{1}{C_2 R} \end{bmatrix} \begin{bmatrix} i_{L_1}(t) \\ v_{C_1}(t) \\ i_{L_2}(t) \\ i_{C_2}(t) \end{bmatrix} + \begin{bmatrix} \frac{1}{L_1} \\ 0 \\ 0 \\ 0 \end{bmatrix} [v_{dc}(t)] \qquad (2.1)$$

$$\frac{d}{dt}\begin{bmatrix} i_{L_1}(t) \\ v_{C_1}(t) \\ i_{L_2}(t) \\ v_{C_2}(t) \end{bmatrix} = \begin{bmatrix} \frac{-r_{l_1}-r_{c_1}}{L_1} & -\frac{1}{L_1} & \frac{r_{c_1}}{L_1} & 0 \\ \frac{1}{C_1} & 0 & -\frac{1}{C_1} & 0 \\ \frac{r_{c_1}}{L_2} & \frac{1}{L_2} & \frac{r_{c_1}+r_{l_2}-r_{c_2}}{L_2} & \frac{1}{L_2} \\ 0 & \frac{1}{C_2} & 0 & -\frac{1}{C_2 R} \end{bmatrix} \begin{bmatrix} i_{L_1}(t) \\ v_{C_1}(t) \\ i_{L_2}(t) \\ v_{C_2}(t) \end{bmatrix} + \begin{bmatrix} 0 \\ 0 \\ 0 \\ 0 \end{bmatrix} [v_{dc}(t)] \qquad (2.2)$$

$$\frac{d}{dt}\begin{bmatrix} \vec{i}_{L_1}(t) \\ \vec{v}_{C_1}(t) \\ \vec{i}_{L_2}(t) \\ \vec{v}_{C_2}(t) \end{bmatrix} = \begin{bmatrix} \frac{-r_{l_1}-r_{c_1}}{L_1} & -\frac{1}{L_1} & \frac{r_{c_1}}{L_1} & 0 \\ \frac{1}{C_1} & 0 & -\frac{1}{C_1} & 0 \\ \frac{r_{c_1}}{L_2} & \frac{1}{L_2} & \frac{r_{c_1}+r_{l_2}-r_{c_2}}{L_2} & \frac{1}{L_2} \\ 0 & \frac{1}{C_2} & 0 & -\frac{1}{C_2 R} \end{bmatrix} \begin{bmatrix} \vec{i}_{L_1}(t) \\ \vec{v}_{C_1}(t) \\ \vec{i}_{L_2}(t) \\ \vec{v}_{C_2}(t) \end{bmatrix} + \begin{bmatrix} \frac{d}{L_1} \\ 0 \\ 0 \\ 0 \end{bmatrix} [\vec{v}_{dc}(t)] \qquad (2.3)$$

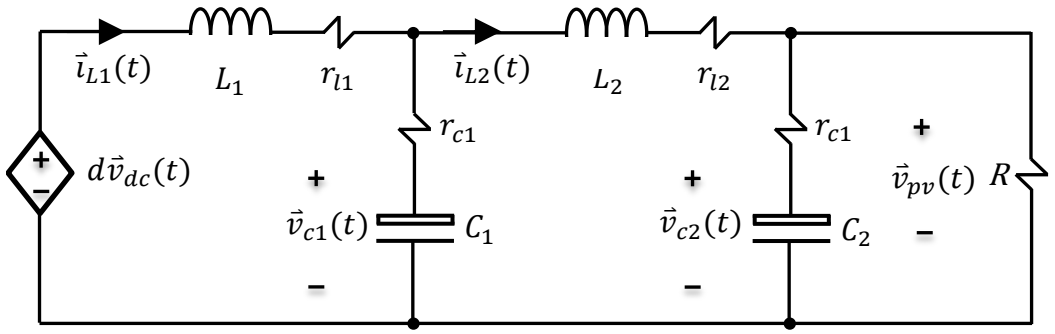

Figure 2.12 Large-signal model circuit diagram of the single-phase buck converter with two-stage output filter

$$\frac{d}{dt}\begin{bmatrix}\tilde{\imath}_{L_1}(t)\\ \tilde{v}_{C_1}(t)\\ \tilde{\imath}_{L_2}(t)\\ \tilde{v}_{C_2}(t)\end{bmatrix}=\begin{bmatrix}\frac{-r_{l_1}-r_{c_1}}{L_1} & -\frac{1}{L_1} & \frac{r_{c_1}}{L_1} & 0\\ \frac{1}{C_1} & 0 & -\frac{1}{C_1} & 0\\ \frac{r_{c_1}}{L_2} & \frac{1}{L_2} & \frac{r_{c_1}-r_{l_2}-r_{c_2}}{L_2} & -\frac{1}{L_2}\\ 0 & 0 & \frac{1}{C_2} & -\frac{1}{C_2R}\end{bmatrix}\begin{bmatrix}\tilde{\imath}_{L_1}(t)\\ \tilde{v}_{C_1}(t)\\ \tilde{\imath}_{L_2}(t)\\ \tilde{v}_{C_2}(t)\end{bmatrix}+\begin{bmatrix}\frac{D}{L_1} & \frac{V_{dc}}{L_1}\\ 0 & 0\end{bmatrix}\begin{bmatrix}\tilde{v}_{dc}(t)\\ \tilde{d}(t)\end{bmatrix} \quad (2.4)$$

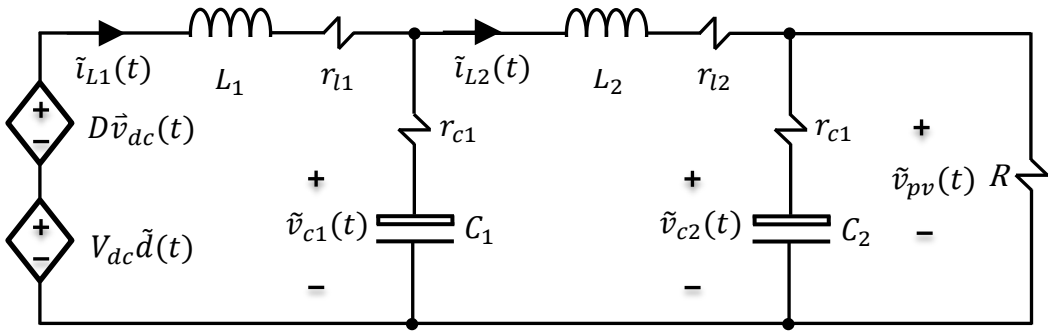

Figure 2.13 Small-signal model circuit diagram of the single-phase buck converter with two-stage output filter

$$G_{id}(s) = \frac{V_{dc}(C_1Rs + 1)}{L_1C_1L_2C_2s^4 + L_1L_2C_1s^3 + (L_1C_2R + 2L_1C_1R)s^2 + (L_1C_1 + L_2C_2)s + R} \quad (2.5)$$

$i_{L_1}, i_{L_2}, v_{C_1}$, and v_{C_2} are the first filter inductor current, the second filter inductor current, the first filter capacitor voltage, and the second filter capacitor voltage, respectively. $r_{l_1}, r_{l_2}, r_{c_1}$, and r_{c_2} represent the equivalent series resistors of the output filter inductors and capacitors. D is the steady-state duty cycle whereas V_{dc} is the steady-state input voltage.

Fig. 2.14 shows the frequency response of the uncompensated system plant $G_{id}(s)$ and the designed current compensator $G_c(s)$. Fig. 2.15 illustrates the frequency response of the inner-current loop gain $T_i(s)$ and the frequency response of the closed inner-current loop $G_{cl}(s)$. The inner-current loop was designed to have a bandwidth of 455 kHz (one decade below the cut-off frequency of output filter), 89^o phase margin, and 15.6 dB gain margin. Since it is a two-loop system, the outer-reference loop's sensor conditioning circuit was designed to have a 40 Hz cut-off frequency, or one decade below the inner-current loop bandwidth. The bandwidth of the outer-reference loop is set using a low pass filter. Table 2-3 shows the controller parameters.

Table 2-3 DESIGNED CONTROLLERS PARAMETERS OF DC-DC CONVERTER STAGE

dc-dc Converter Stage (Buck)		
Inner-Current Loop $G_i(s)$	$k\frac{(s/\omega_{z1}+1)(s/\omega_{z2}+1)}{s(s/\omega_{p1}+1)(s/\omega_{p2}+1)}$	$k = 83.843$ $\omega_{z1} = 27.451\ krad/s$ $\omega_{z2} = 37.475\ krad/s$ $\omega_{p1} = 190.92\ krad/s$ $\omega_{p2} = 644.83\ krad/s$
Outer-Reference Loop $G_v(s)$	$k\frac{1}{(s/\omega_p+1)(s/\omega_p+1)}$	$k = 1.0$ $\omega_p = 251\ rad/s$

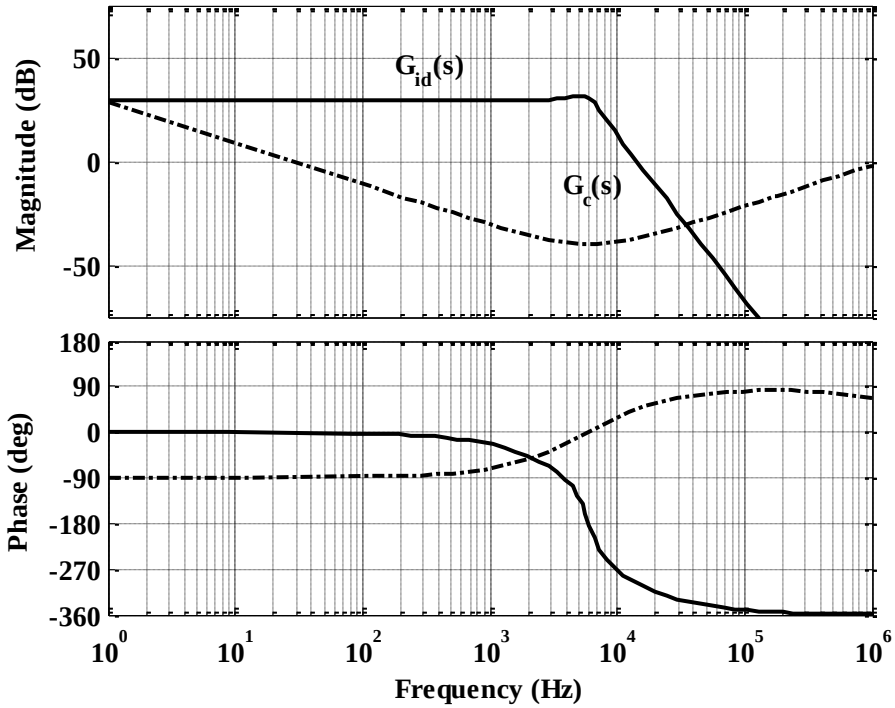

Figure 2.14 Converter frequency response of the uncompensated system plant $G_{id}(s)$ and the designed current controller $G_c(s)$

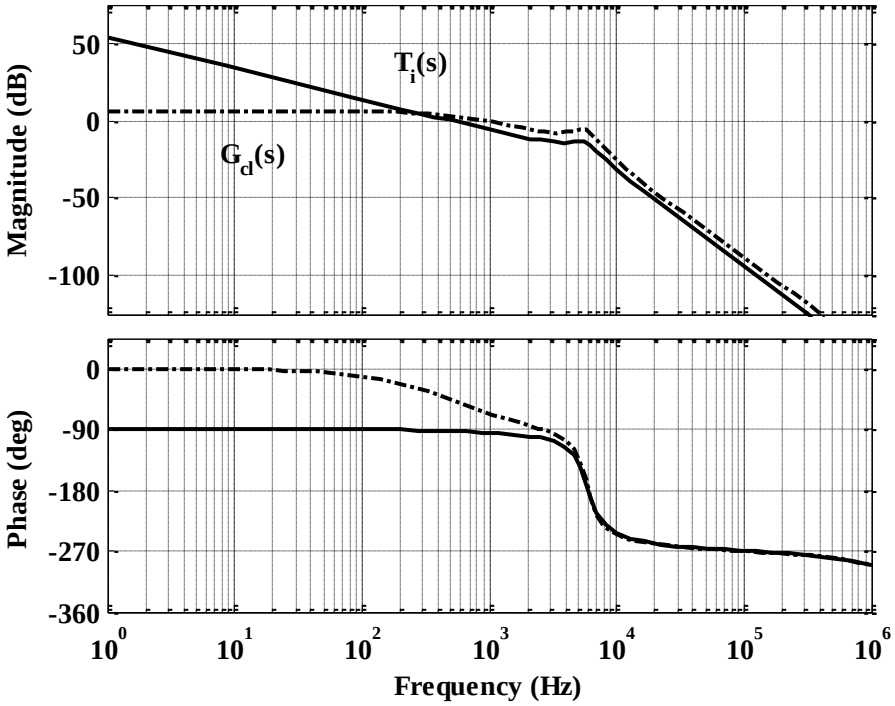

Figure 2.15 Converter frequency response of the compensated inner-current loop gain $T_i(s)$ and the frequency response of the closed inner-current loop $G_{cl}(s)$

2.5 EXPERIMENTAL RESULTS

The proposed PV source simulator is experimentally built and tested. Fig. 2.16 shows the proposed simulator hardware prototype. A resistor bank was used as the variable load to reproduce the PV current-voltage characteristic. The voltage sensor gain h_1 and the current sensor gains h_2 and h_3 are set to be 0.014, 4, and 0.2, respectively. Therefore, the open-circuit voltage and short-circuit current of the dc-dc buck converter will be 250 V (= 3.5 V / 0.014) and 20 A (= 1.0 A × 4 / 0.2). The overall power conversion gain is about 1400. The maximum output power was tested up to 2.7 kW. With higher input voltage and sufficient cooling of the power-stage, this power level can be further increased.

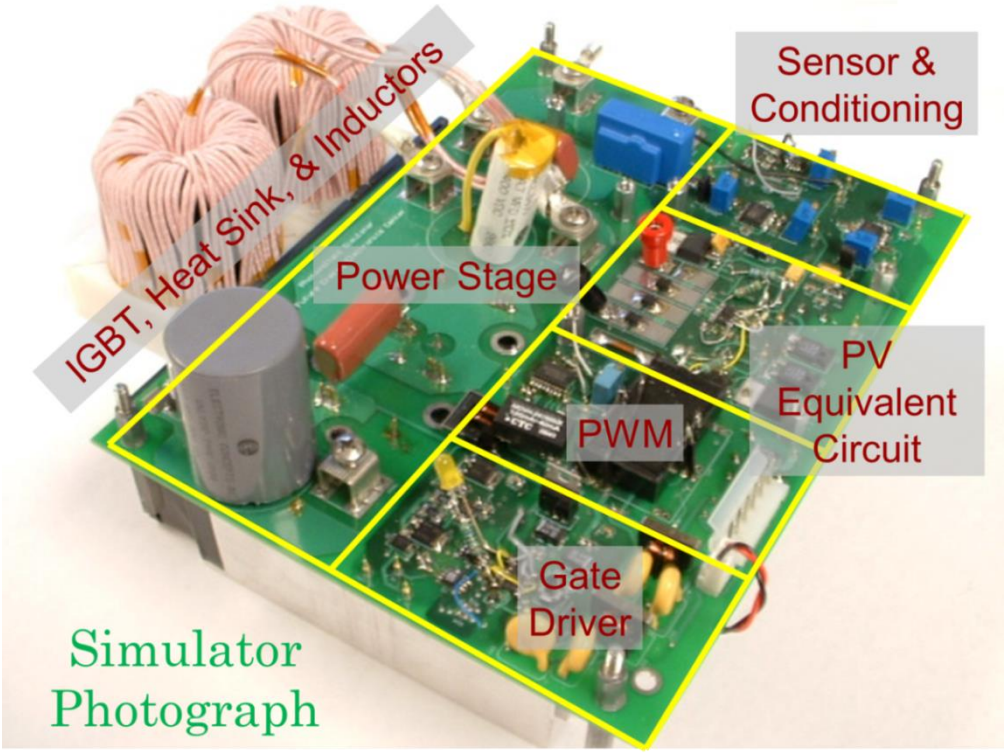

Figure 2.16 Hardware prototype of the proposed photovoltaic source simulator

Fig. 2.17 shows the measured efficiency results of the PV source simulator at different output power levels. The efficiency was measured using a digital multi-meter with 0.025% dc accuracy (Model: Fluke 187). The efficiency maintains in between 95% and 96% from 300 W to 2.7 kW power output.

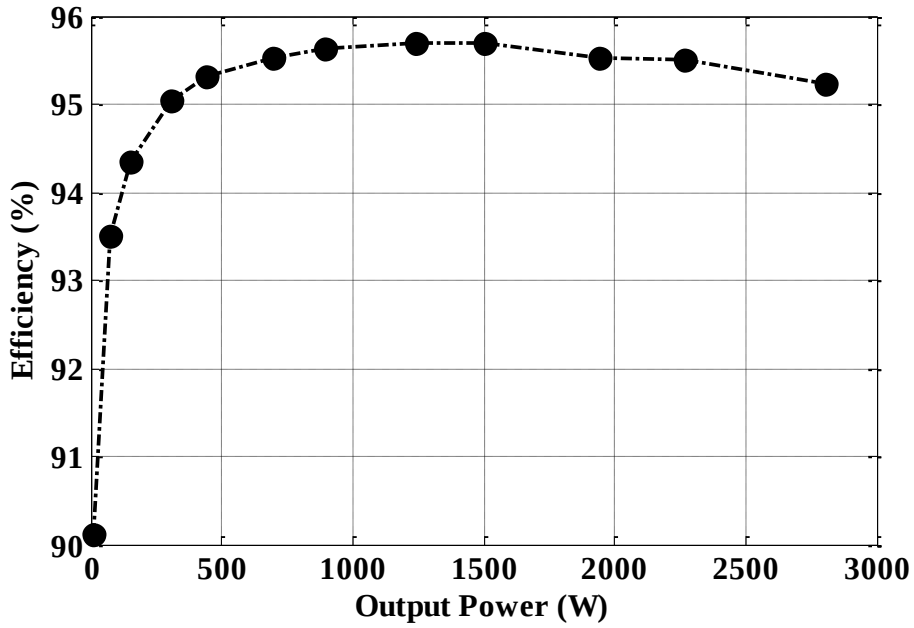

Figure 2.17 Measured PV source simulator efficiency curve including converter and filter power-stages

Fig. 2.18 presents the experimental waveforms showing the detailed steady-state performance of the proposed PV source simulator connected to an electronic load (resistive mode). Fig. 2.18(a) shows the PV source simulator performance when operating at the constant current operational zone of the PV characteristic curve (high-current and low-voltage), whereas Fig. 2.18(b) shows the performance of the PV source simulator when operating at the constant voltage operational zone of the PV characteristic curve (low-current and high-voltage). The system shows a stable performance in both zones due to the robust design of system controller,

although, the system control-loop bandwidth was optimized at the MPP operational condition of the emulated PV curve. Moreover, during both operational zones (constant-current and constant-voltage) current through the dc-dc stage second inductor L_2 stays in continuous conduction mode. Mixed operational modes (continuous or discontinuous) may cause control system instability.

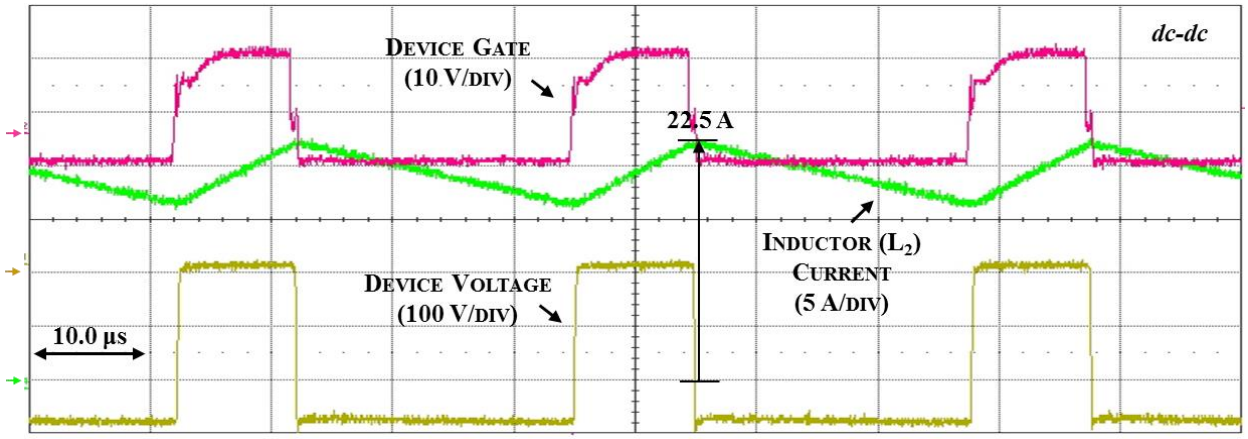

(a)

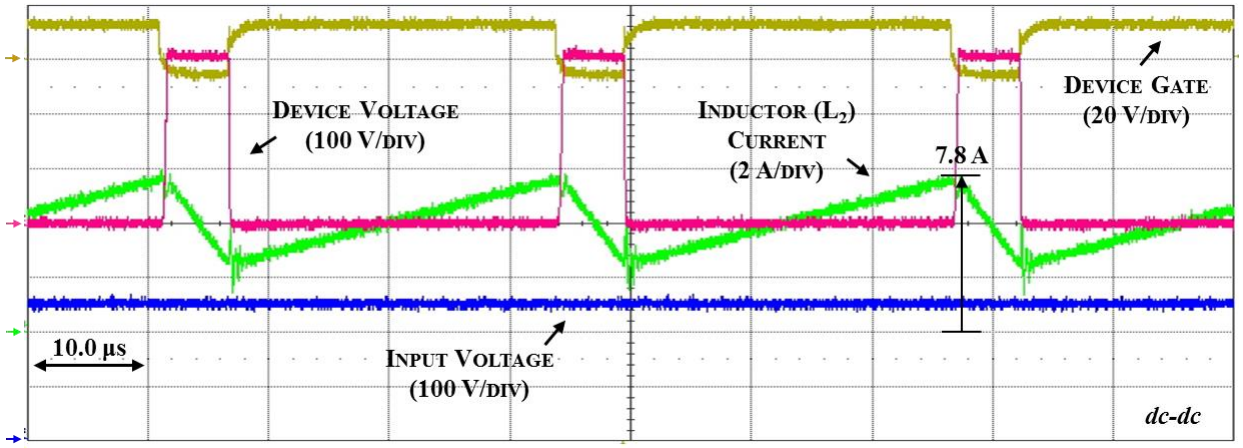

(b)

Figure 2.18 Detailed steady-state experimental waveforms of the proposed PV source simulator; **(a)** High-current and low-voltage operation zone and **(b)** Low-current and high-voltage operation zone

2.5.1 USING PHOTOVOLTAIC EQUIVALENT CIRCUIT WITH DIODES

This section shows test results using the PV equivalent circuit with series-connected diodes shown in Fig. 2.4 to generate the reference current signal $I_{sc,ec}{}^{*}$. The PV characteristic curves shown in Fig. 2.19 were generated by the power-stage at different irradiance reference levels. The results match with the current-voltage reference curve in Fig. 2.6 with the desired conversion ratios. With higher irradiance level, the MPP shift up to a higher current and lower voltage level.

Fig. 2.20 records the transient response-time waveforms of the output voltage v_{pv} and output current i_{pv} of the proposed PV source simulator for a step load change (76 Ω to 9 Ω). Response-time was recorded to be 3.8 milliseconds. This time will be enhanced with the design in Chapter 3; accordingly the PV source simulator will be more adequate for the evaluation of solar power conditioning systems and MPPT algorithms.

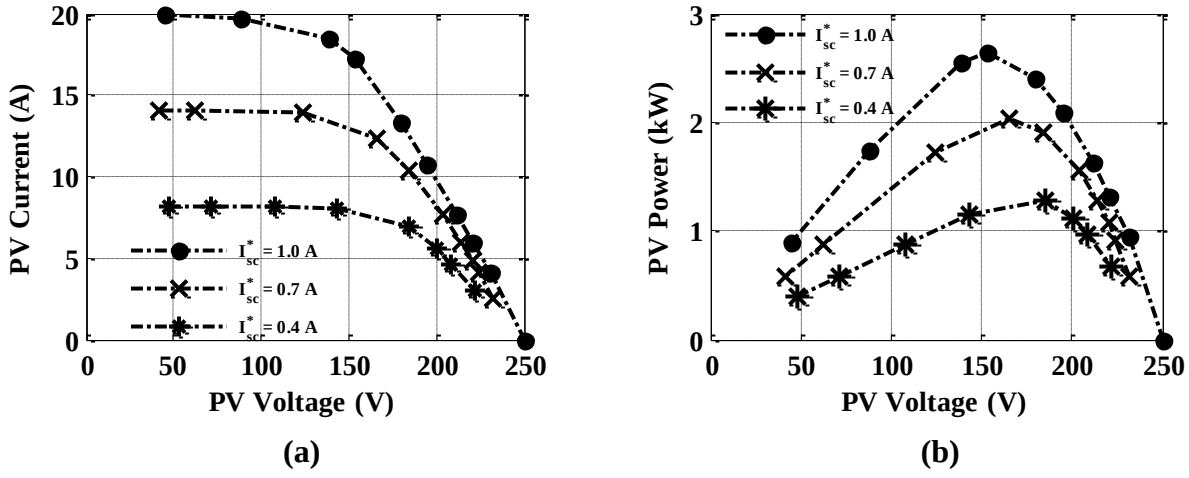

Figure 2.19 Experimental PV curves generated by power-stage implementing PV equivalent circuit with diodes; **(a)** Current-voltage and **(b)** Power-voltage

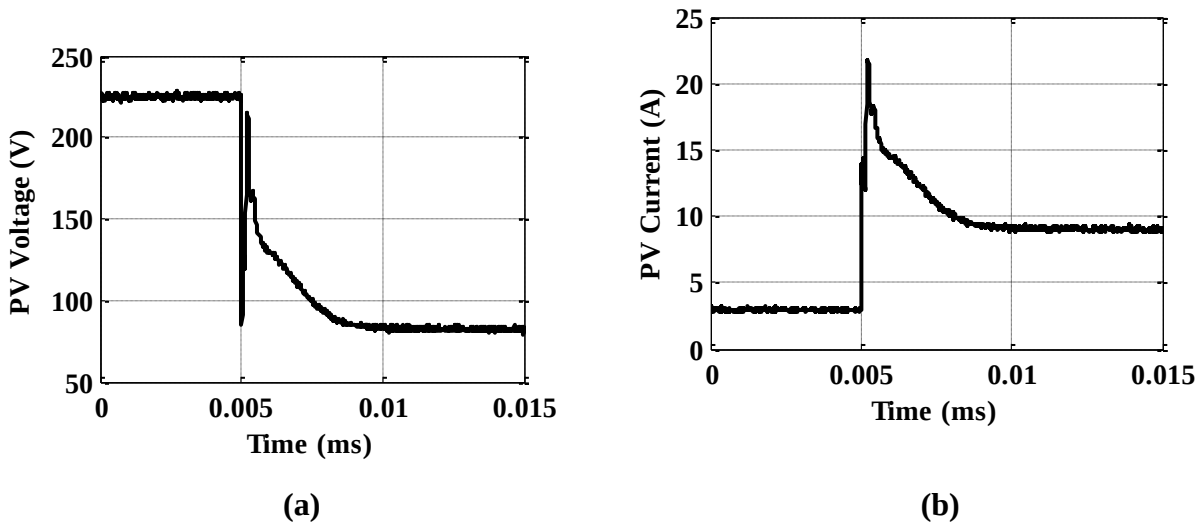

Figure 2.20 Experimental dynamic response waveforms for a step load change; **(a)** PV voltage and **(b)** PV current

Fig. 2.21 shows the output voltage v_{pv} and current i_{pv} waveforms of the PV source simulator under different irradiance levels and perturbing frequencies. The current source $I_{sc,ec}{}^{*}$ corresponds to the irradiance level, which is a triangular wave and serves as the reference. The output voltage and current of the power-stage $v_{pv}$and i_{pv} should follow the given reference precisely. Fig. 2.21(a) shows the results of slow perturbation using a 10 Hz triangular wave as the reference. The output voltage and current follow the reference very well. Fig. 2.21(b) shows the results of fast perturbation using a 40 Hz triangular wave as the reference. In this case, the output voltage and current cannot exactly follow the reference, resulting in waveform distortion. In general, the time interval of most MPPT control algorithms is more than one second, and a fast perturbation with higher than 10 Hz frequency rarely occur. Therefore, the response of this PV source simulator is sufficient for evaluating the MPPT control algorithms of the solar power

conditioning systems. The PV source simulator overall bandwidth is designed as previously mentioned to be 40 Hz, which does match with this result.

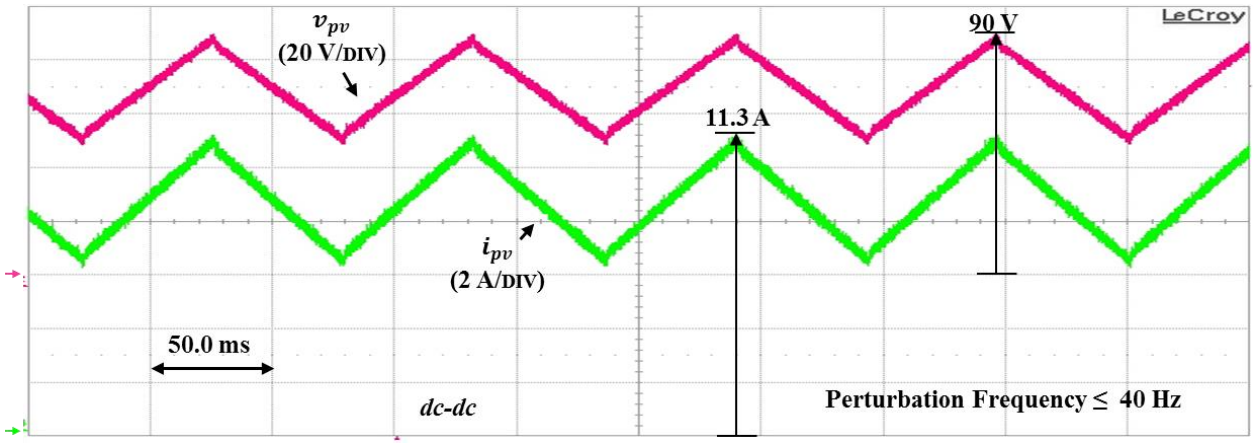

(a)

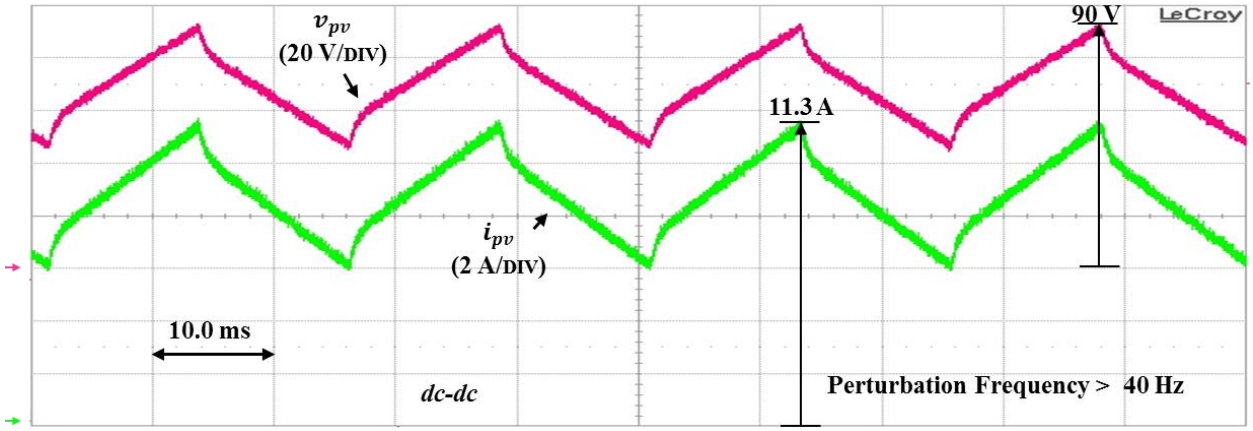

(b)

Figure 2.21 Experimental waveforms of PV source simulator output voltage and current with perturbation injected to the reference current; **(a)** ≤ 40 Hz and **(b)** > 40 Hz

2.5.2 USING PHOTOVOLTAIC EQUIVALENT CIRCUIT WITH AN ACTUAL PV CELL

This section shows the test results using an un-illuminated polycrystalline PV cell based PV source simulator shown in Fig. 2.9. Fig. 2.22 shows the current-voltage characteristic curve

generated by the power-stage with $I_{sc,ec}{}^{*}$ is 0.4 A, and different offset voltages $R_s I_{sc,ec}$. The result matches the basic cell characteristic shown in Fig. 2.10 with a desired voltage and current conversion ratios. The perturbation test results are not shown because they are the same as those shown in Fig. 2.21.

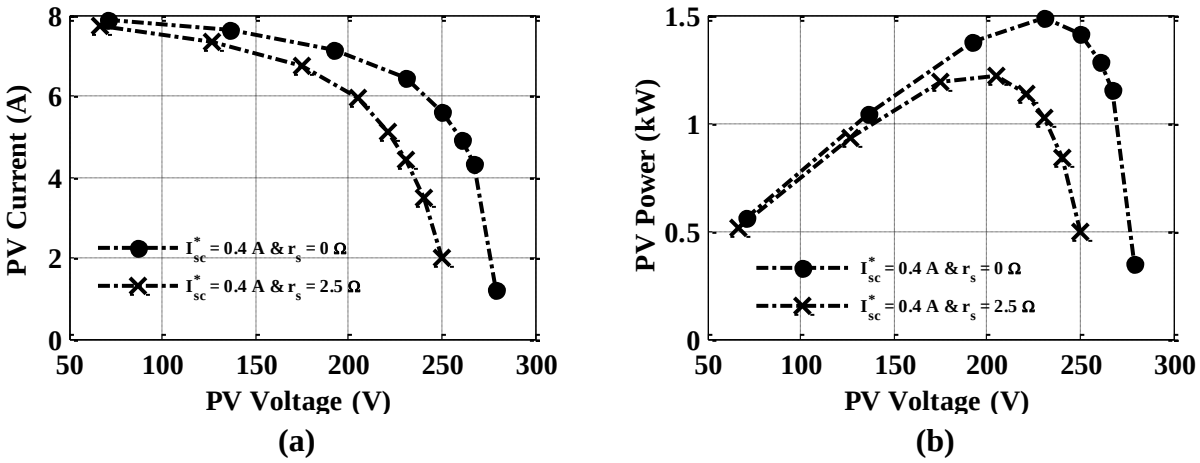

Figure 2.22 Experimental PV curve generated by power-stage implementing PV equivalent circuit with un-illuminated a polycrystalline PV cell; **(a)** Current-voltage and **(b)** power-voltage

2.6 SUMMARY

In this chapter, a systematic design approach is proposed and described in detail for a PV source simulator, which consists of a PV equivalent circuit, a control system circuit, and a power-stage circuit. The PV equivalent circuit is implemented with a novel analog circuit using high-bandwidth voltage-controlled current-source and voltage-controlled voltage-source to generate high precision current-voltage reference curves in order to eliminate the computation time delays in digital controllers. The power-stage consists of a single-phase buck converter and a two-stage output filter with a high cut-off frequency to allow a high control-loop bandwidth while keeping the same switching ripple attenuation as a one-stage output filter does.

The proposed PV source simulator hardware prototype has been designed and built. Two approaches of generating the current-voltage reference signal using a series diode stack and an actual um-illuminated PV cell were implemented. Both approaches show power-stage output matches the actual PV characteristic curve with the desired conversion ratios. Experimental results showed high accuracy and reasonably fast response-time. Power level of 2.7 kW has been demonstrated.

CHAPTER 3

DESIGN OF HYBRID-BASED PHOTOVOLTAIC SOURCE SIMULATOR WITH HIGH-EFFICIENCY AND FAST RESPONSE-TIME FOR SOLAR POWER CONDITIONING SYSTEMS EVALUATION

3.1 INTRODUCTION

This chapter presents a new type of hybrid-based PV source simulator. The proposed two-stage PV source simulator is characterized with high power-stage efficiency and fast transient response-time. Therefore, the proposed system is adequate for solar power conditioning systems evaluation. Response-time of PV source simulators has been reported to be in the range of 10 milliseconds to several 100 milliseconds [64]-[66]. The hybrid simulator combines both analog and digital based concepts. This technique decreases digital computational times allowing a higher switching frequency and therefor a higher control-loop bandwidth to be selected. The proposed system extracts real-time current-voltage reference characteristic curves using an actual solar reference-cell (0.5 Watt) with a controllable light source. This analog extraction technique is simple, very accurate, and flexible. Subsequently, the reference curves are processed with a DSP for flexible and reliable control-loop implementation. The switching power-stage amplifies the reference curves with a PWM to produce high power current-voltage characteristic. The power-stage consists of an active-front-end (AFE) three-phase ac-dc rectifier cascaded with a multi-phase dc-dc interleaved converter. This chapter describes the development and design of the PV source simulator in detail. System description along with control strategy will be

thoroughly presented. Hardware setup and experimental results of the PV source simulator connected to an electronic load at different environmental and load conditions will be shown to verify the performance of the proposed system and its design concept.

3.2 SYSTEM DESCRIPTION AND CONTROL STRATEGY

The basic structure of the proposed PV source simulator is composed of three main circuits: (i) the power-stage circuit, (ii) digital control circuit, and (iii) analog reference-generation circuit. The power-stage includes a three-phase ac-dc rectifier cascaded with a multi-phase dc-dc converter. The three-phase ac-dc rectifier is a new type of dual boost topology [67], [68]. Fig. 3.1 presents the circuit diagram of the proposed ac-dc dual boost rectifier. For each phase, the upper and lower switch duty cycles are determined by the direction of its input phase reference current and its calculated ac reference duty cycle, as described in (3.1) and (3.2).

$$\left.\begin{array}{c} i_{a_{ref}} \leq 0 \\ d_{a_U} = {}^1\!/_2 - {}^1\!/_2\, d_a \\ d_{a_L} = 0 \end{array}\right\} \tag{3.1}$$

$$\left.\begin{array}{c} i_{a_{ref}} \geq 0 \\ d_{a_U} = 0 \\ d_{a_L} = {}^1\!/_2 + {}^1\!/_2\, d_a \end{array}\right\} \tag{3.2}$$

$i_{a_{ref}}$ is phase a reference current, d_a is phase a reference duty cycle, and d_{a_U}, d_{a_L} are phase a upper and lower switch duty cycles with no dead time required. The dual boost circuit

integrates two active switches per phase or six active switches for a three-phase system without having two switches in series for each phase leg; in consequence, the shoot-through failure is avoided. This distinguished feature makes the dual boost topologies attractive due to their high reliability. Generally, a hard-switched conventional three-phase circuit utilizes IGBTs rather than MOSFET as the main power switch because of poor reverse recovery characteristic of their body diodes. However, in dual boost circuit, the MOSFETs can be employed with three-phase circuits as their body diodes do not conduct current. The use of MOSFETs allows higher switching frequencies where the size of the passive components can be significantly reduced. Furthermore, the turn-off and conduction losses can be substantially reduced with proper switch selection.

Fig. 3.2 illustrates the proposed control strategy of the three-phase dual boost rectifier. This digital control system is based on the dq0 synchronous rotating reference frame that is referenced to the grid phase-to-neutral voltage v_{an} through a phase locked loop (PLL). The PLL circuit is designed in the dq0 synchronous frame as shown in Fig. 3.3 along with its designed parameters. The voltage reference of the PLL control-loop ${v_{d_{PLL}}}^*$ is set to zero and an angle offset (30^o) has been added to compensate for the phase difference between line-to-line and phase-to-neutral grid voltages. The control system incorporates two decoupled inner-current loops (d-axis and q-axis) to control the ac input current and a superimposed outer-voltage loop to control the dc-link voltage. The outer-voltage loop generates the q-axis current reference, whereas the d-axis current reference is set to zero to get unity power factor at the ac side. In some cases, the d-axis current reference is set to a negative value to compensate for the reactive power component of the input current; this reactive power can be created due to the insertion of the electromagnetic interference (EMI) filter [69]. The control system outputs three reference

voltages ${v_{as}}^*, {v_{bs}}^*,$ and ${v_{cs}}^*$. Afterward, a hybrid pulse width modulation (HPWM) technique is applied to create the PWM gating sequence of the three-phase dual boost rectifier [70]. This HPWM technique adds a zero sequence voltage reference ${v_{zs}}^*$ to the three reference voltages; the zero sequence reference voltage is given in (3.3) and (3.4).

$$\left.\begin{matrix} {v_{max}}^* - {v_{mid}}^* > {v_{mid}}^* - {v_{min}}^* \\ {v_{zs}}^* = 1 - {v_{max}}^* \end{matrix}\right\} \tag{3.3}$$

$$\left.\begin{matrix} {v_{max}}^* - {v_{mid}}^* < {v_{mid}}^* - {v_{min}}^* \\ {v_{zs}}^* = -1 - {v_{min}}^* \end{matrix}\right\} \tag{3.4}$$

${v_{max}}^*, {v_{mid}}^*,$ and ${v_{min}}^*$ are the maximum, minimum, and middle values of the three reference voltages, respectively. The resultant reference voltages are then divided by the dc-link voltage to create duty cycles $d_a, d_b,$ and d_c. HPWM helps reduce switching losses and further improve the system efficiency.

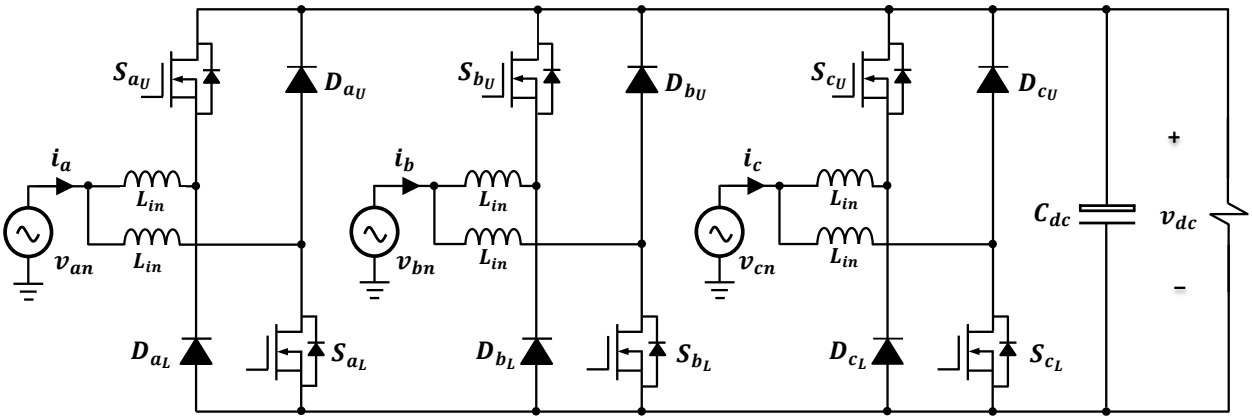

Figure 3.1 Circuit diagram of the proposed three-phase ac-dc dual boost rectifier

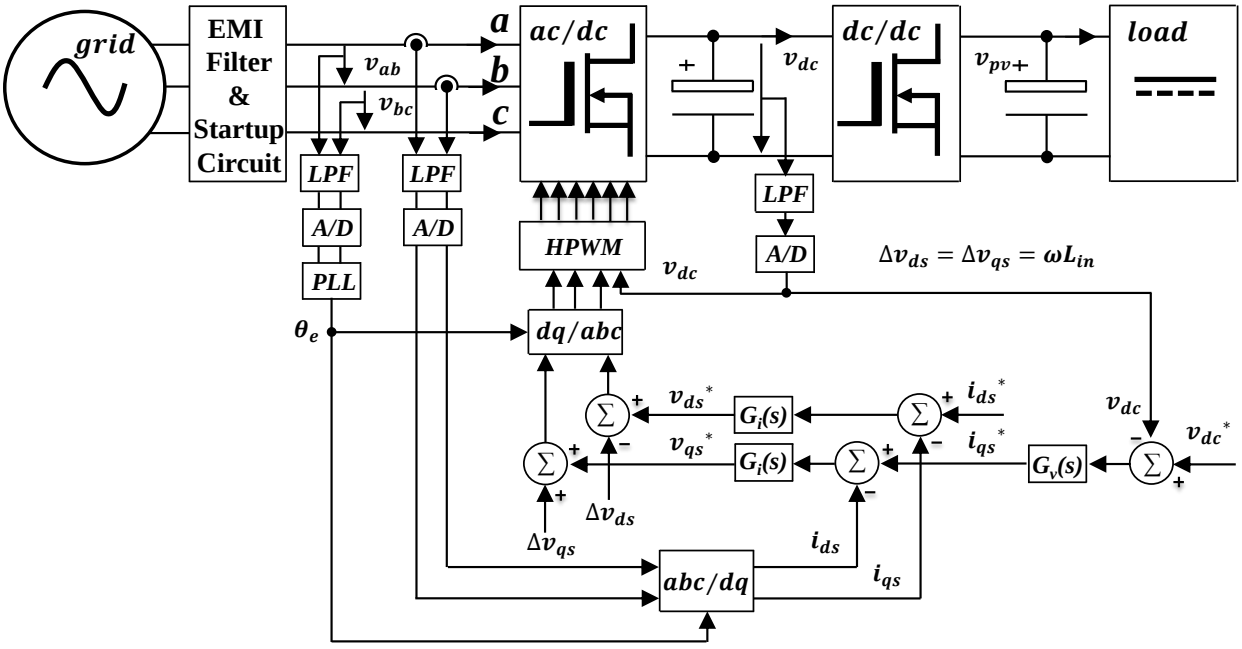

Figure 3.2 Proposed control strategy block diagram for the three-phase ac-dc rectifier

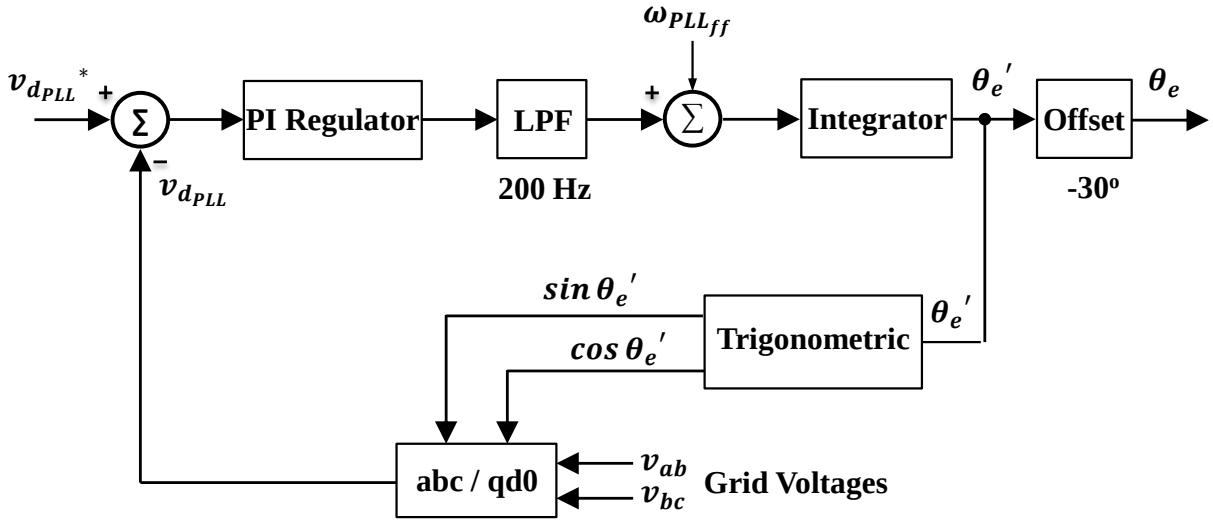

Figure 3.3 Proposed digital phase locked loop circuit diagram

The second part of the power circuit is a multi-phase dc-dc interleaved converter [71], [72]. The multi-phase circuit consists of three interleaved buck converters as shown in Fig. 3.4. The multiple interleaved currents divide the total output current by n number of phases to lower the current stress of semiconductor devices and therefore reduce system conduction losses proportional to n. Moreover, ripple currents tend to cancel each other at the output of the converter causing a continuous dc input current at certain conditions, and thus allowing larger ripple current for individual phase currents or smaller size inductors [73]. This allows the control system to be designed with an ultrafast transient response-time, which is necessary for PV source simulators. Furthermore, the fundamental frequency of the output ripple current is n times the switching frequency allowing a small output capacitor to be used. Fig. 3.5 shows the proposed control strategy of the three-phase dc-dc interleaved buck converter. This hybrid control system incorporates two control-loops, an outer analog loop and an inner digital loop. The purpose of the outer analog loop is to generate a precise real-time reference current whereas the inner digital loop aims to control the total average inductor current i_L of the converter to match the actual current-voltage characteristic of the reference-cell and achieve fast dynamic response to load disturbances. The real-time analog reference generation is conceived by the circuit shown in Fig. 3.6. This high-bandwidth analog circuit, which is designed based on the circuit shown in Fig. 2.8 of Chapter 2; controls the output voltage of an illuminated PV cell $V_{pv,cell}$ in order to generate the control-loop reference current $I_{pv,cell}$. This analog implementation of the reference generation circuit is accurate, simple, and flexible. Moreover, no digital computational times are introduced to the control system. Modeling, control, and design of different circuitries of the PV source simulator including the ac-dc rectifier stage, the dc-dc converter stage, and the analog reference generation stage will be thoroughly introduced in the next section.

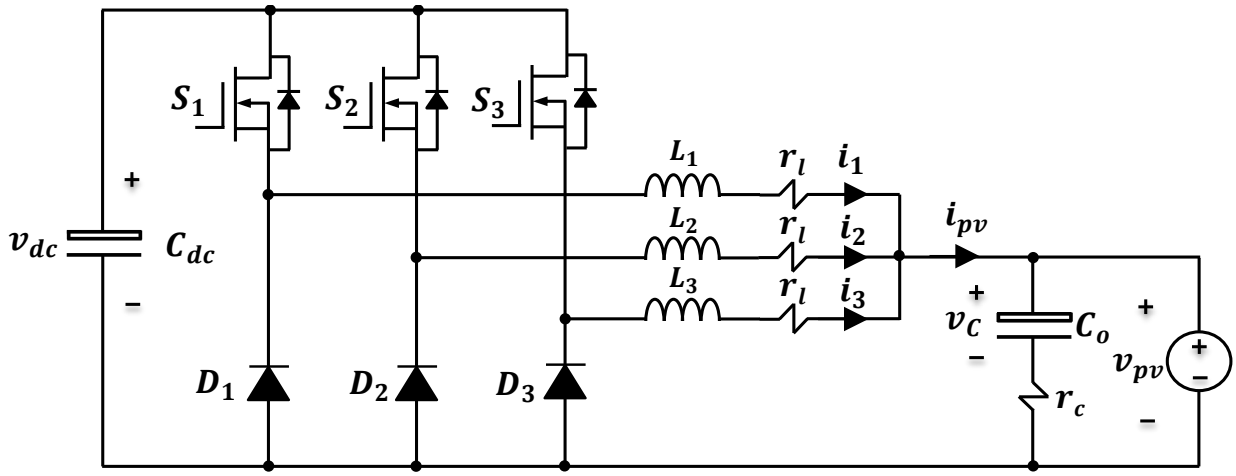

Figure 3.4 Circuit diagram of the proposed three-phase dc-dc interleaved buck converter

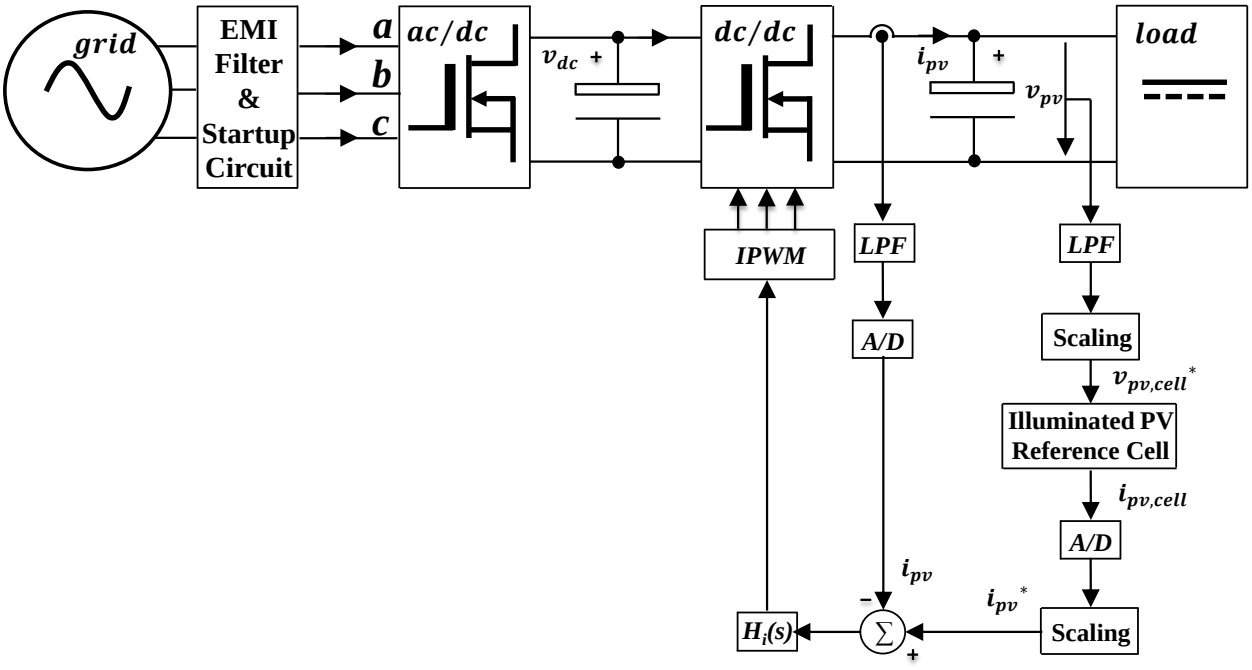

Figure 3.5 Proposed control strategy block diagram for the three-phase dc-dc converter

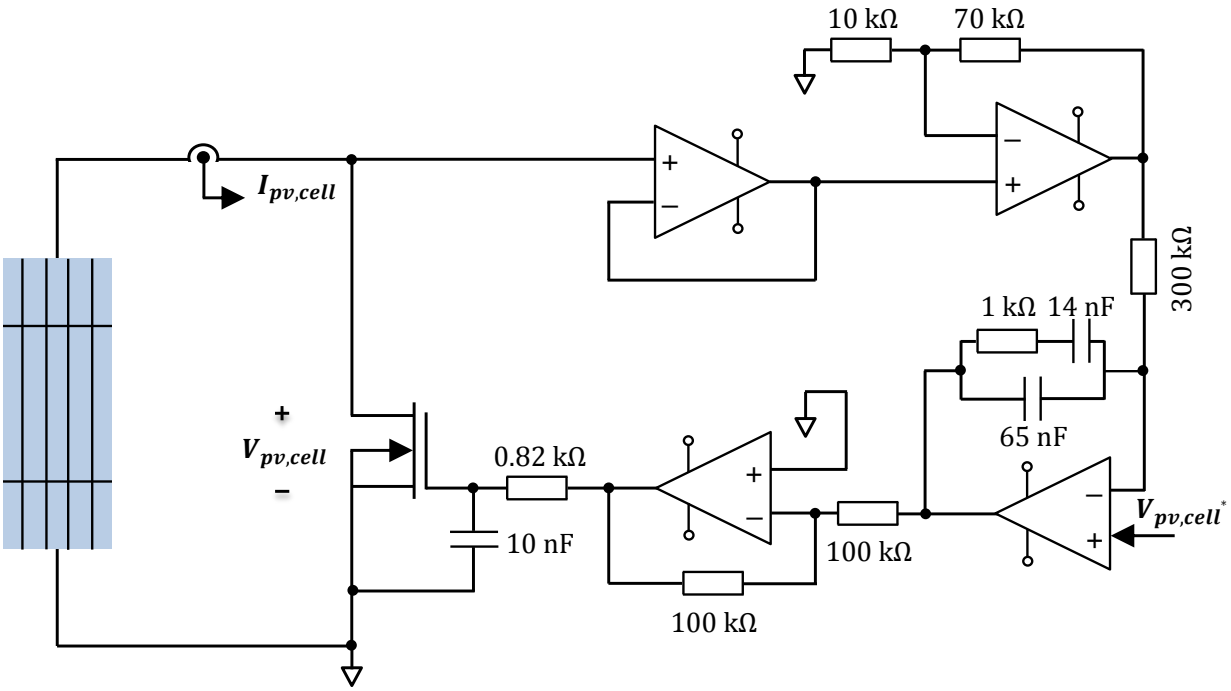

Figure 3.6 Real-time reference generation circuit diagram of the proposed system

3.3 CONTROL SYSTEM AND POWER STAGE DESIGN METHODOLOGY

3.3.1 MODELING, CONTROL, AND DESIGN OF THE AC-DC RECTIFIER STAGE

The dual control system of the ac-dc rectifier stage aims to control the dc-link output voltage, control and shape the ac input current, achieve unity power factor at the input, and attain a fast dynamic response to load disturbances. This system is implemented with Texas Instruments DSP (Model: TMS320F28335), which is a 32-bit high performance floating point controller. The design of the rectifier control-loops in frequency domain (q-axis and d-axis control-loops) requires the derivation of four models in state space representation format: (i) the switching-model as in (3.5) and (3.6) (ii) the large-signal model in abc-frame as in (3.7) and (3.8), (iii) the large-signal model in dq0-frame as in (3.9), and (iv) the small-signal model as in (3.10). Park's transformation matrix is used to transform the abc-frame to the dq0-frame. The dq0 frame reduces the three ac quantities into a two dc quantities, and hence simplifies mathematical operations. Based on the derived models (switching, large, and small-signal), the decoupled control to q-axis input-current transfer function $G_{id}(s)$ in dq0 synchronous rotating reference frame assuming continuous conduction mode (CCM) operation is derived as in (3.11).

$$\frac{d}{dt}\begin{bmatrix} i_a(t) \\ i_b(t) \\ i_c(t) \end{bmatrix} = \frac{1}{L_{in}}\begin{bmatrix} v_{an}(t) \\ v_{bn}(t) \\ v_{cn}(t) \end{bmatrix} - \frac{1}{L_{in}}[v_{dc}(t)]\begin{bmatrix} s_a \\ s_b \\ s_c \end{bmatrix} + \frac{1}{3}[v_{dc}(t)]\begin{bmatrix} 1 & 1 & 1 \\ 1 & 1 & 1 \\ 1 & 1 & 1 \end{bmatrix}\begin{bmatrix} s_a \\ s_b \\ s_c \end{bmatrix} \tag{3.5}$$

$$\frac{d}{dt}[v_{dc}(t)] = -\frac{1}{RC_{dc}}[v_{dc}(t)] + \frac{1}{L_{in}}[s_a \quad s_b \quad s_c]\begin{bmatrix} i_a(t) \\ i_b(t) \\ i_c(t) \end{bmatrix} \tag{3.6}$$

$$\frac{d}{dt}\begin{bmatrix}\vec{\imath}_a(t)\\ \vec{\imath}_b(t)\\ \vec{\imath}_c(t)\end{bmatrix}=\frac{1}{L_{in}}\begin{bmatrix}\vec{v}_{an}(t)\\ \vec{v}_{bn}(t)\\ \vec{v}_{cn}(t)\end{bmatrix}-\frac{1}{L_{in}}[\vec{v}_{dc}(t)]\begin{bmatrix}\vec{d}_a(t)\\ \vec{d}_b(t)\\ \vec{d}_c(t)\end{bmatrix}+\frac{1}{3}[\vec{v}_{dc}(t)]\begin{bmatrix}1 & 1 & 1\\ 1 & 1 & 1\\ 1 & 1 & 1\end{bmatrix}\begin{bmatrix}\vec{d}_a(t)\\ \vec{d}_b(t)\\ \vec{d}_c(t)\end{bmatrix} \tag{3.7}$$

$$\frac{d}{dt}[\vec{v}_{dc}(t)]=-\frac{1}{RC_{dc}}[\vec{v}_{dc}(t)]+\frac{1}{L_{in}}\begin{bmatrix}\vec{d}_a(t) & \vec{d}_b(t) & \vec{d}_c(t)\end{bmatrix}\begin{bmatrix}\vec{\imath}_a(t)\\ \vec{\imath}_b(t)\\ \vec{\imath}_c(t)\end{bmatrix} \tag{3.8}$$

$$\frac{d}{dt}\begin{bmatrix}\vec{\imath}_{ds}(t)\\ \vec{\imath}_{qs}(t)\\ \vec{v}_{dc}(t)\end{bmatrix}=\begin{bmatrix}0 & -\omega & -\frac{d_d}{L_{in}}\\ \omega & 0 & -\frac{d_q}{L_{in}}\\ \frac{d_d}{C_{dc}} & \frac{d_q}{C_{dc}} & -\frac{1}{C_{dc}R}\end{bmatrix}\begin{bmatrix}\vec{\imath}_{ds}(t)\\ \vec{\imath}_{qs}(t)\\ \vec{v}_{dc}(t)\end{bmatrix}+\begin{bmatrix}\frac{1}{L_{in}} & 0\\ 0 & \frac{1}{L_{in}}\\ 0 & 0\end{bmatrix}\begin{bmatrix}\vec{v}_{dg}(t)\\ \vec{v}_{qg}(t)\end{bmatrix} \tag{3.9}$$

$$\frac{d}{dt}\begin{bmatrix}\tilde{\imath}_{ds}(t)\\ \tilde{\imath}_{qs}(t)\\ \tilde{v}_{dc}(t)\end{bmatrix}=\begin{bmatrix}0 & -\omega & -\frac{D_d}{L_{in}}\\ \omega & 0 & -\frac{D_q}{L_{in}}\\ \frac{D_d}{C_{dc}} & \frac{D_q}{C_{dc}} & -\frac{1}{RC_{dc}}\end{bmatrix}\begin{bmatrix}\tilde{\imath}_{ds}(t)\\ \tilde{\imath}_{qs}(t)\\ \tilde{v}_{dc}(t)\end{bmatrix}+\begin{bmatrix}\frac{1}{L_{in}} & 0 & -\frac{V_{dc}}{L_{in}} & 0\\ 0 & \frac{1}{L_{in}} & 0 & -\frac{V_{dc}}{L_{in}}\\ 0 & 0 & \frac{I_{ds}}{C_{dc}} & \frac{I_{qs}}{C_{dc}}\end{bmatrix}\begin{bmatrix}\tilde{v}_{dg}(t)\\ \tilde{v}_{qg}(t)\\ \tilde{d}_d(t)\\ \tilde{d}_q(t)\end{bmatrix} \tag{3.10}$$

$$G_{id}(s)=V_{dc}\frac{C_{dc}s+2\frac{P_o}{V_{dc}^2}}{L_{in}C_{dc}s^2+L_{in}\frac{P_o}{V_{dc}^2}s+D_q^2} \tag{3.11}$$

The derived switching model is based on the switching combinations of the three-phase switching functions s_a, s_b, and s_c. If phase a upper switch is on s_a is one and if phase a lower switch is on s_a is zero. i_a, i_b, and i_c are input phase current, v_{an}, v_{bn}, and v_{cn} are grid input phase voltages, d_a, d_b, and d_c are phase duty cycles, i_{ds}, i_{qs} are the d-axis and q-axis

components of the input phase currents, v_{dg}, v_{qg} are the d-axis and q-axis components of the grid input phase voltages, v_{dc} is the dc-link voltage, d_d, d_q are the d-axis and q-axis components of the phase duty cycles, ω is the angular frequency, c_{dc} is the dc-link capacitance, L_{in} is the phase boost inductance, R is the equivalent resistance of the dc-dc converter-stage, and P_o is the rectifier steady-state output power.

Fig. 3.7, Fig. 3.8, and Fig. 3.9 illustrate the equivalent circuit diagram of the derived large-signal model in abc-frame, large-signal model in dq0-frame, and small-signal-model in dq0 frame, respectively.

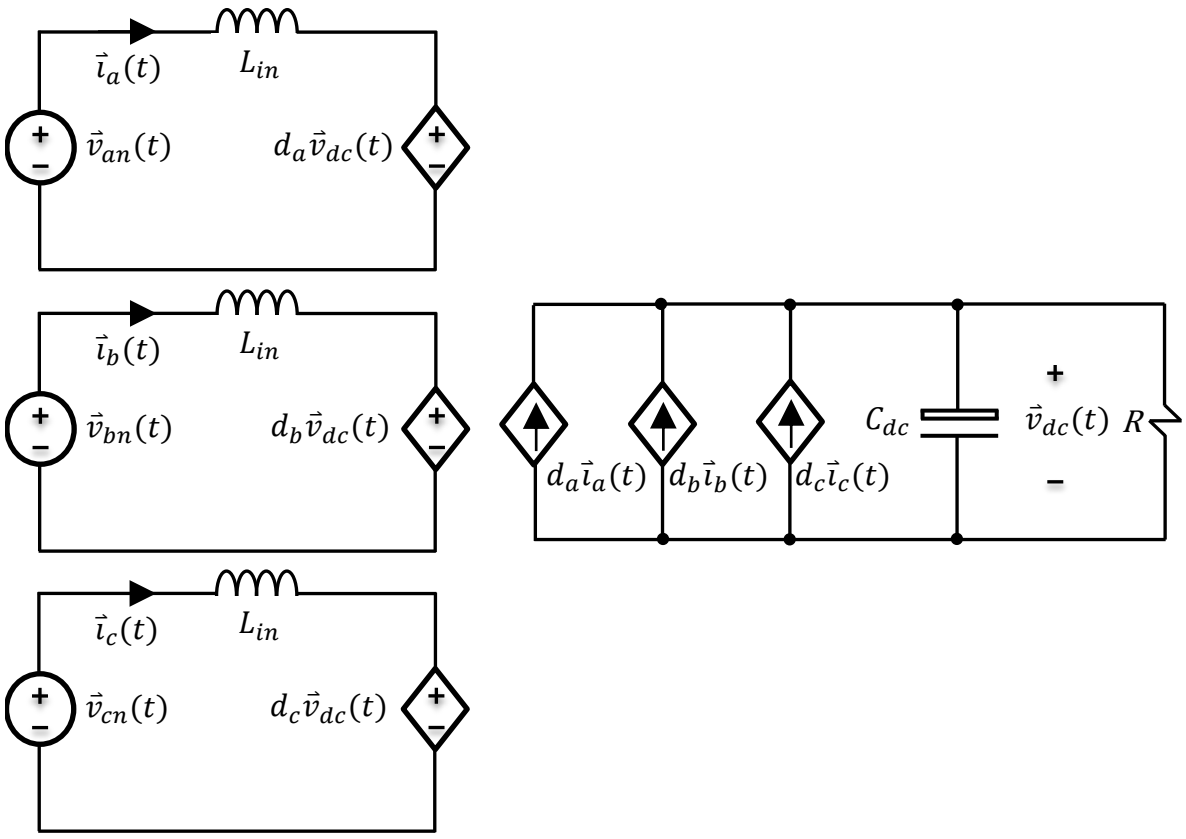

Figure 3.7 Large-signal model circuit diagram in abc-frame of the three-phase ac-dc dual boost rectifier

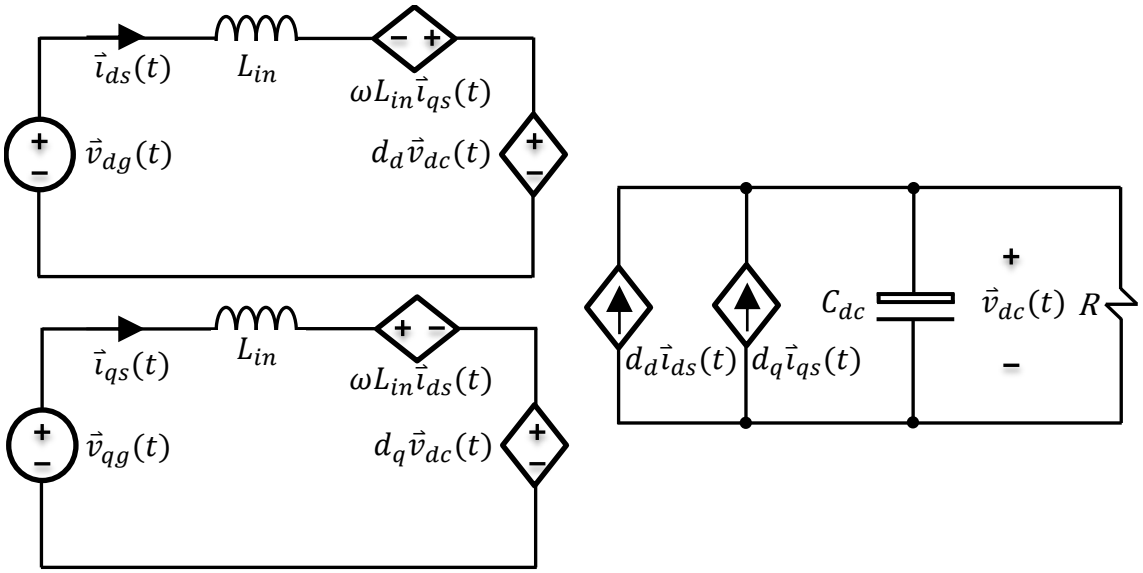

Figure 3.8 Large-signal model circuit diagram in dq0-frame of the three-phase ac-dc dual boost rectifier

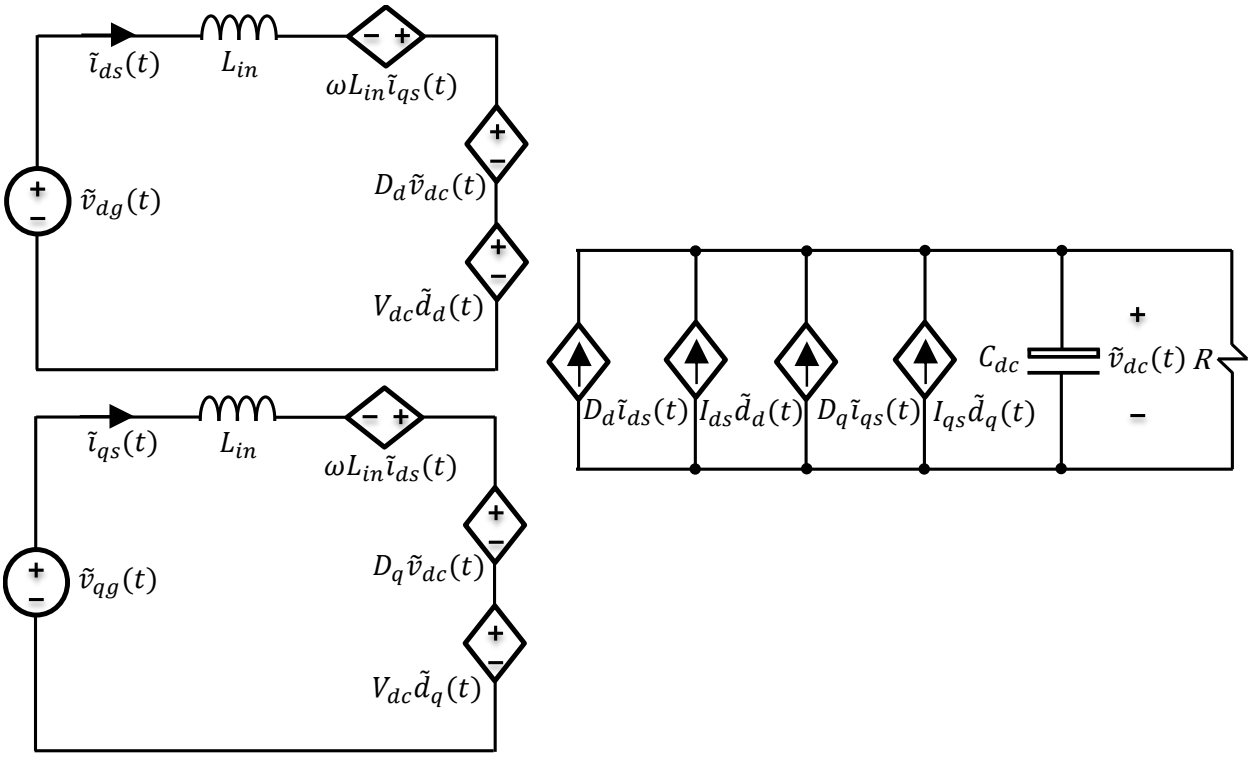

Figure 3.9 Small-signal model circuit diagram in dq0-frame of the three-phase ac-dc dual boost rectifier

The design procedure of the q-axis and d-axis current loop controllers is identical. A conventional linear proportional-integral (PI) controller $G_i(s)$ is suitable to realize input current fast dynamics and minimize steady-state error. The controller is designed around the peak MPP of the dc-dc converter stage to maintain full control bandwidth.

Fig. 3.10 shows the frequency response of the compensated current loop gain $T_i(s)$ including digital time delay. The digital time delay is modeled as e^{-sT_S} (T_s is the sampling time). The designed controller attains a 2.5 kHz cross-over frequency that is about one-tenth below the switching frequency (33 kHz) and 88^o phase margin through placing the compensator zero at a frequency below the resonant frequency of the system plant $G_{id}(s)$. This design scenario minimizes current overshoot but may cause zero crossing distortion because the system holds high phase margin at frequencies lower than the designed bandwidth. After closing the current loops (q-axis and d-axis), the outer-voltage loop that controls the dc-link voltage can be closed. The dc-link voltage to the q-axis reference current transfer function can be derived as in (3.12) and (3.13).

$$G_{vi}(s) = \frac{T_{icl}(s)}{C_{dc}s + P_o/V_{dc}^2} \tag{3.12}$$

$$T_{icl}(s) = \frac{T_i(s)}{1 + T_i(s)} = \frac{G_i(s)G_{id}(s)}{1 + G_i(s)G_{id}(s)} \tag{3.13}$$

$T_{icl}(s)$ is the closed-loop q-axis current controller transfer function. A PI controller $G_v(s)$ is used as a voltage compensator to regulate the dc-link voltage. Fig. 3.10 shows the frequency response of the compensated outer-voltage loop gain $G_v(s)$ including digital time delay, as well.

In three-phase rectifier systems, the voltage loop is usually designed at a frequency one decade below 360 Hz so that the controller does not respond to the sixth harmonic of line frequency at the dc-link [74]. Therefore, the voltage loop is designed to achieve a 50 Hz cross-over frequency and 93^o phase margin. Table 3-1 shows the designed current and voltage compensator parameters of the inner-current loops and outer-voltage loop of the rectifier stage.

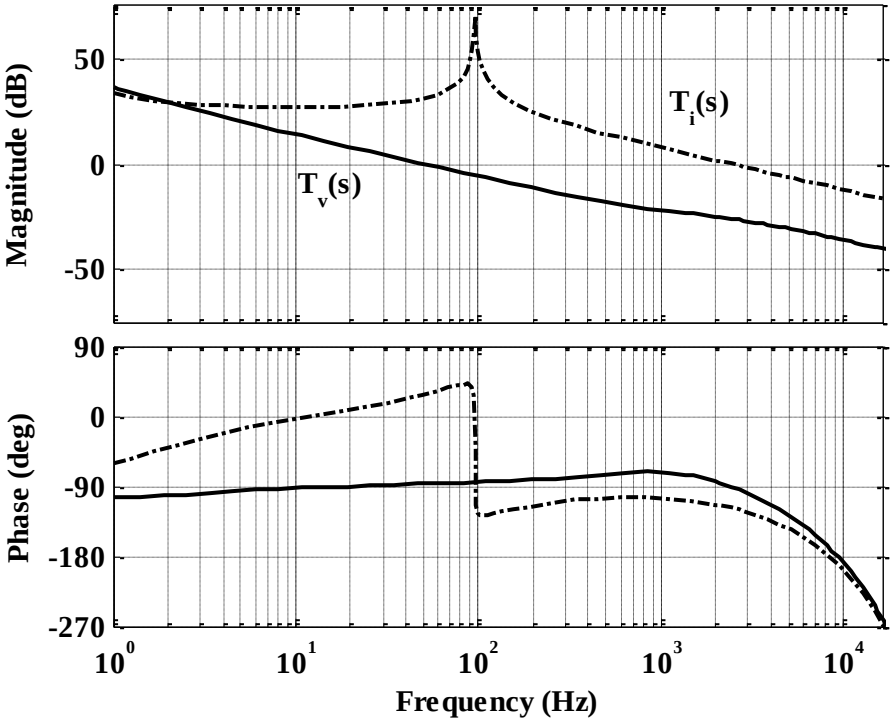

Figure 3.10 Rectifier frequency response of the compensated current loop gain $T_i(s)$ and voltage loop gain $T_v(s)$, including digital time delay

The rectifier stage input inductance L_{in} is designed in CCM to allow 10% peak-to-peak input current ripple. Three stackable toroid powder cores with 60μ permeability (Model: Kool Mμ 77192A) has been selected to obtain the required inductance value. The inductor was built and experimentally tested using a two-pulse test circuit to verify its inductance value along with

its saturation current characteristic. Fig 3.11 shows the experimental waveforms of inductor current and voltage. The inductor current reaches 30 A linearly with no saturation and its equivalent dc resistance is 41 mΩ. The no-load inductance is 950 µH whereas the full-load inductance is 750 µH. The dc-link capacitor (Model: EET-UQ2W471LF) has been selected to allow a 1.0 V peak-to-peak ripple at the dc-link voltage. The equivalent series resistance of the selected capacitor is 423 mΩ. Fairchild's SuperMOS MOSFET (Model: FCA76N60N) with a rating of 600 V and 36 mΩ is selected as the power-stage main switching device to achieve high power-stage efficiency and allow small heat sinking requirement with no forced air cooling. ST Microelectronic's ultra-fast recovery diode (Model: STTH6004W) with a reverse recovery time of t_{rr} = 50 ns and low forward voltage drop has been chosen as the power-stage main switching diode to minimize the reverse recovery effect on system performance and hence improve the overall efficiency of the power-stage.

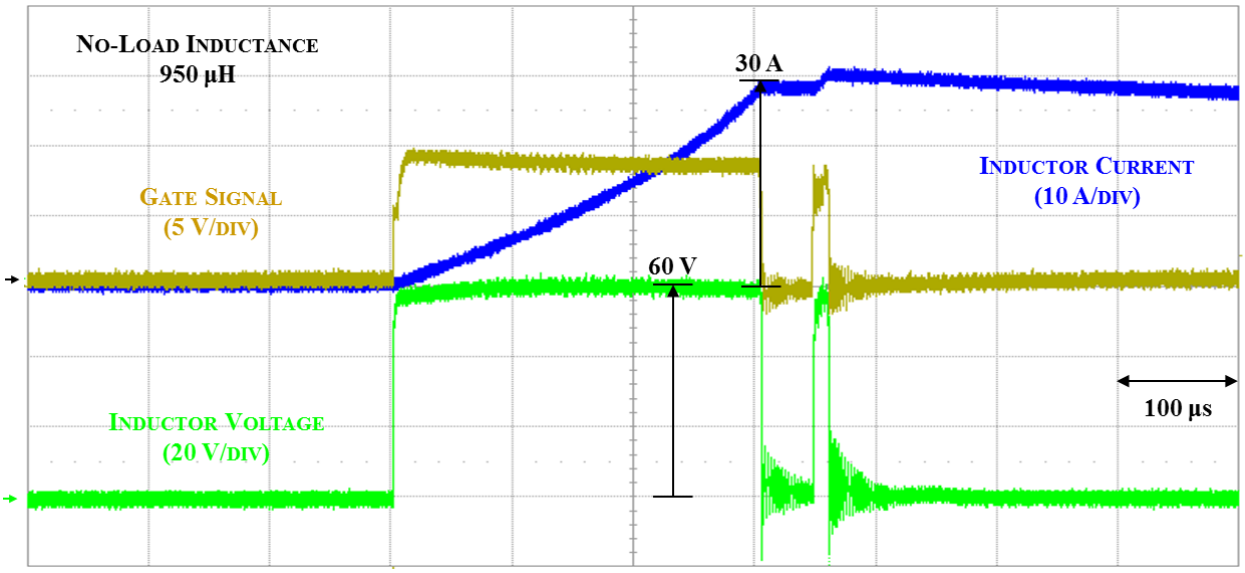

Figure 3.11 Inductors saturation current design verification test for the three-phase ac-dc rectifier power-stage

3.3.2 MODELING, CONTROL, AND DESIGN OF THE DC-DC CONVERTER STAGE

The control system of the dc-dc converter stage aims to control the total output inductor current i_{pv} of the converter through an inner digital loop. To design the dc-dc converter control system, the large and small-signal models of the three-phase buck converter are derived assuming resistive type load as in (3.14) and (3.15) and a voltage type load as in (3.16) and (3.17), respectively. Based on the derived models, the control to the total-current transfer function $H_{id}(s)$ including circuit parasitics is given as in (3.18) for a resistive type load and as in (3.19) for a voltage type load.

$$\frac{d}{dt}\begin{bmatrix}\vec{i}_{pv}(t)\\ \vec{v}_C(t)\end{bmatrix}=\begin{bmatrix}-\dfrac{(r_l+\frac{Rr_c}{R+r_c})}{L_o} & -\dfrac{R}{L_o(R+r_c)}\\ \dfrac{R}{C_o(R+r_c)} & -\dfrac{1}{C_o(R+r_c)}\end{bmatrix}\begin{bmatrix}\vec{i}_{pv}(t)\\ \vec{v}_C(t)\end{bmatrix}+\begin{bmatrix}\dfrac{d}{L_o}\\ 0\end{bmatrix}[\vec{v}_{dc}(t)] \tag{3.14}$$

$$\frac{d}{dt}\begin{bmatrix}\tilde{i}_{pv}(t)\\ \tilde{v}_C(t)\end{bmatrix}=\begin{bmatrix}-\dfrac{(r_l+\frac{Rr_c}{R+r_c})}{L_o} & -\dfrac{R}{L_o(R+r_c)}\\ \dfrac{R}{C_o(R+r_c)} & -\dfrac{1}{C_o(R+r_c)}\end{bmatrix}\begin{bmatrix}\tilde{i}_{pv}(t)\\ \tilde{v}_C(t)\end{bmatrix}+\begin{bmatrix}\dfrac{D}{L_o} & \dfrac{V_{dc}}{L_o}\\ 0 & 0\end{bmatrix}\begin{bmatrix}\tilde{v}_{dc}(t)\\ \tilde{d}(t)\end{bmatrix} \tag{3.15}$$

$$\frac{d}{dt}\begin{bmatrix}\vec{i}_{pv}(t)\\ \vec{v}_C(t)\end{bmatrix}=\begin{bmatrix}-\dfrac{r_l}{L_o} & 0\\ 0 & \dfrac{1}{C_o r_c}\end{bmatrix}\begin{bmatrix}\vec{i}_{pv}(t)\\ \vec{v}_C(t)\end{bmatrix}+\begin{bmatrix}\dfrac{d}{L_o} & -\dfrac{1}{L_o}\\ 0 & \dfrac{1}{C_o r_c}\end{bmatrix}\begin{bmatrix}\vec{v}_{dc}(t)\\ \vec{v}_{pv}(t)\end{bmatrix} \tag{3.16}$$

$$\frac{d}{dt}\left[\tilde{\imath}_{pv}(t)\right] = \begin{bmatrix} -\frac{r_l}{L_o} & 0 \\ 0 & \frac{1}{C_o r_c} \end{bmatrix}\left[\tilde{\imath}_{pv}(t)\right] + \begin{bmatrix} \frac{D}{L_o} & \frac{V_{dc}}{L_o} & -\frac{1}{L_o} \end{bmatrix}\begin{bmatrix} \tilde{v}_{dc}(t) \\ \tilde{d}(t) \\ \tilde{v}_{pv}(t) \end{bmatrix} \tag{3.17}$$

$$H_{id}(s) = \frac{V_{dc}(C_o(R + r_c)s + 1)}{L_o C_o(R + r_c)s^2 + (L_o + C_o R r_l + C_o R r_c + C_o r_l r_c)s + (R + r_l)} \tag{3.18}$$

$$H_{id}(s) = \frac{V_{dc}}{L_o s + r_l} \tag{3.19}$$

i_{pv} is the total inductor current, v_C is the output capacitor voltage, d is the converter main duty cycle, L_o is the output phase inductance ($L_o = L_1/3 = L_2/3 = L_3/3$), C_o is the output capacitance of the converter stage, r_l and r_c are the equivalent series resistance of the phase inductance and output capacitance, respectively. R is the equivalent load resistance of the power conditioning system. A proportional-integral-derivative (PID) controller $H_i(s)$ is selected to achieve fast dynamic response of the current loop assuming either a resistive type load or a voltage type load. Although, the cut-off frequency of the output filter is a key limitation factor against high system control-loop bandwidth, the use of the three-phase interleaved buck converter allows the use of small phase inductors and output capacitor, which improves system transient response. The designed compensator achieves a 2.09 kHz cross-over frequency, which is about one-tenth below the switching frequency (33 kHz) and 104^o phase margin. Fig. 3.12 shows the frequency response of the uncompensated system plant $H_{id}(s)$ and the compensated current loop gain $L_i(s)$ including digital time delay for a resistive type load and for a voltage type load. The control system includes an outer analog reference loop that generates the

reference value to the digital inner-current loop. The outer loop includes the reference-cell circuitry, which is designed to have a high-bandwidth in order to match the response of the actual PV cell. An analog controller $H_v(s)$ is implemented to obtain 200 Hz cross-over frequency, which is one-tenth of the inner-current loop bandwidth and 90^o phase margin. To limit the speed of the outer loop, a low pass filter (LPF) is added in series with the reference-cell circuitry to control the converter overall bandwidth. This control-loop bandwidth will be changed to optimize the converter overall bandwidth as will be discussed in the experimental results section of Chapter 4. Fig. 3.13 shows the measured loop gain of the reference generation circuit using Venable frequency response analyzer (Model: 3120). Table 3-1 summarizes the parameters of the designed controllers of the converter stage.

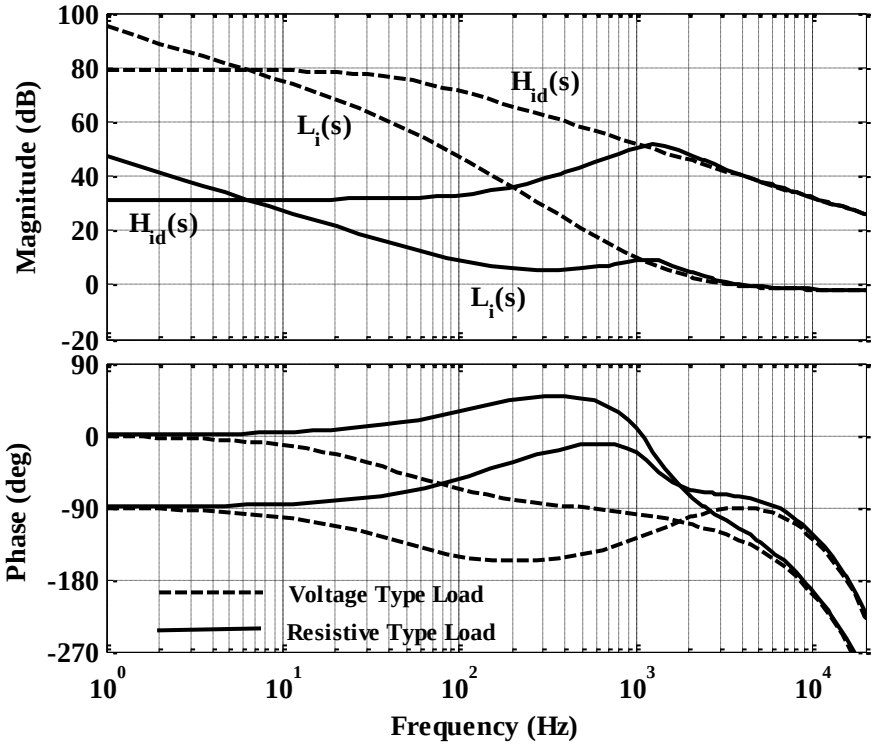

Figure 3.12 Converter frequency response of the system plant $H_{id}(s)$ and the compensated current loop gain $L_i(s)$, including digital time delay for voltage and resistive type loads

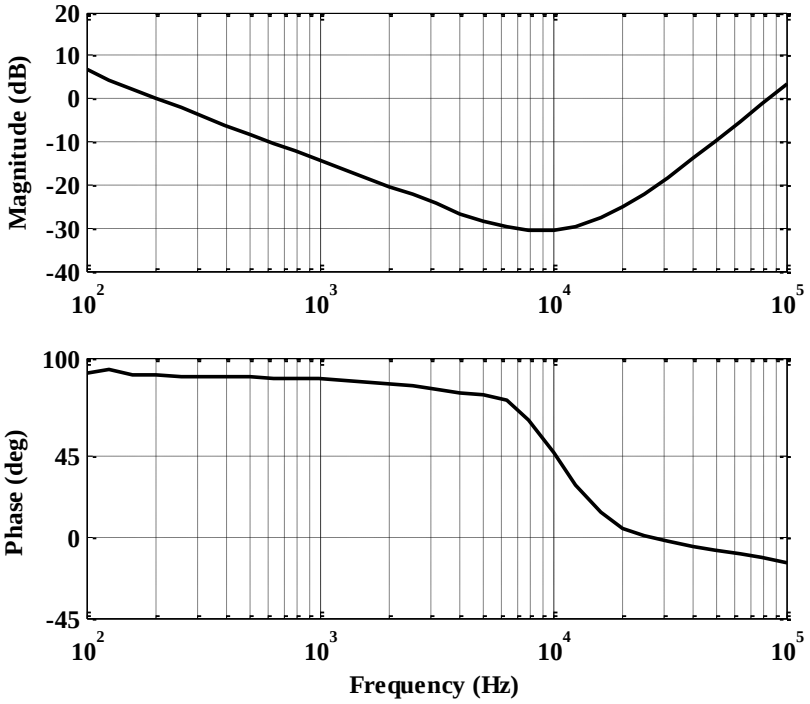

Figure 3.13 Measured compensated loop gain of reference generation circuit

The three-phase interleaved dc-dc converter phase inductance is designed in CCM to allow 6 A peak-to-peak phase current ripple. This high phase ripple amount allows a small inductance to be selected and therefore improves system transient response and control-loop bandwidth design. Simultaneously, the interleaved multi-phase dc-dc converter stage topology minimizes the total output current ripple. The minimum phase inductance of a defined ripple percentage for the multi-phase dc-dc buck converter in continuous conduction mode is defined as in (3.20).

$$L_{phase} = \frac{V_{dc}V_{pv} - {V_{pv}}^2}{nV_{dc}f_s\Delta I_{pv}} \tag{3.20}$$

f_s is the power-stage switching frequency and ΔI is the peak-to-peak output current ripple. Four toroid powder cores with 26μ permeability (Model: Kool Mμ 77191A) has been selected to meet the design requirement. Fig 3.14 shows the inductor current and voltage waveform under the two-pulse test to verify its inductance value along with its saturation current characteristic. The inductor current reaches 30 A linearly with no saturation. The dc resistance of the inductor is 42 mΩ. The no-load inductance is 450 μH whereas the full-load inductance is 400 μH. The multi-phase circuit allows a small output capacitor C_o (Model: B43504B9017M) to be selected as the output current ripple frequency is n times the switching frequency of the power-stage. As a result, the cut-off frequency of the output filter is sufficiently pushed high to improve system bandwidth while keeping low output ripple. The equivalent series resistance of the selected capacitor is 880 mΩ. The dc-dc converter stage utilizes Infineon's CoolMOS MOSFET (Model: IPW60R045CP) as its switching device with a rating of 650 V and 45 m Ω on-resistance. The selected switching device is adequate for hard switching applications with no forced air cooling. The same fast recovery diode from the rectifier stage is employed in the converter stage as well.

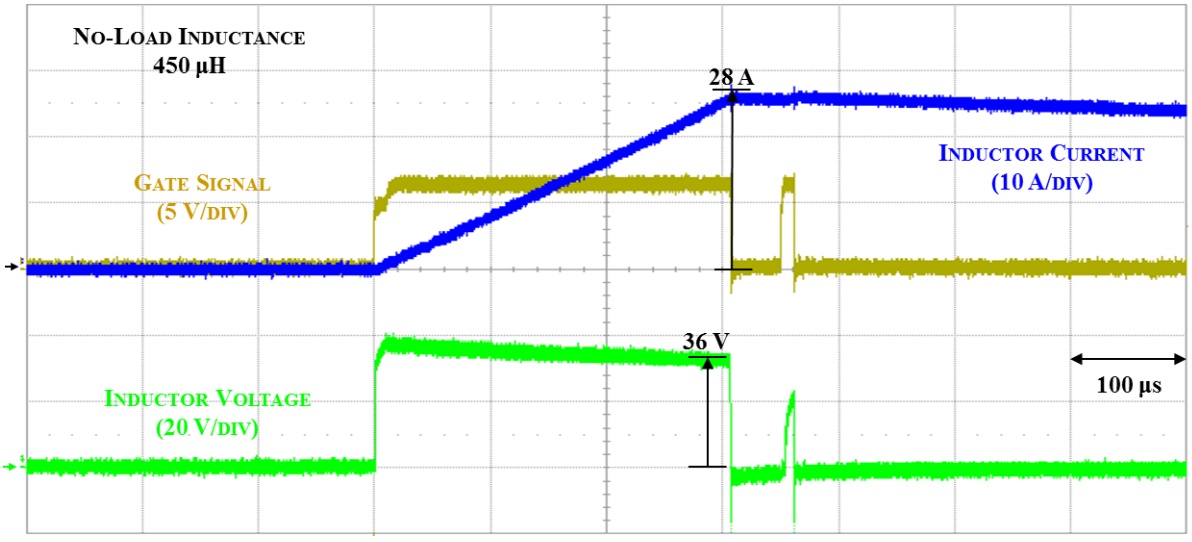

Figure 3.14 Inductors saturation current design verification test for the three-phase dc-dc converter power-stage

Table 3-1 DESIGNED CONTROLLERS PARAMETERS OF AC-DC RECTIFIER AND DC-DC CONVERTER STAGES

ac-dc Rectifier Stage (Boost)		
Control-Loop	Controller Format	Design Parameters
Inner-Current Loop $G_i(s)$	$k\frac{(s/\omega_z+1)}{s}$	$k=20.64$ $\omega_z=526\,rad/s$
Outer-Voltage Loop $G_v(s)$	$k\frac{(s/\omega_z+1)}{s}$	$k=7$ $\omega_z=9\,rad/s$
dc-dc Converter Stage (Buck)		
Inner-Current Loop $H_i(s)$	$k\frac{(s/\omega_z+1)(s/\omega_z+1)}{s}$	$k=22.3$ $\omega_z=11.05\,krad/s$
Outer-Reference Loop $H_v(s)$	$k\frac{(s/\omega_z+1)}{s(s/\omega_p+1)}$	$k=42.19$ $\omega_z=71.4\,krad/s$ $\omega_p=86.8\,krad/s$

3.4 EXPERIMENTAL RESULTS

The proposed PV source simulator was experimentally implemented and tested to verify its steady-state and dynamic performance based on the above-described methodology. Fig. 3.15 shows the proposed simulator hardware prototype. Two experimental setups were conducted: i) The photovoltaic source simulator connected to an electronic load (resistive mode) to reproduce the PV characteristic at different load and environmental conditions and ii) The photovoltaic source simulator connected to a commercial and non-commercial solar power inverters to evaluate the dynamic performance of the solar power conditioning system and to optimize the PV source simulator control-loop bandwidth, this setup will be covered in Chapter 4. The electrical specifications and components parameters of the proposed PV source simulator are summarized in Table 3-2.

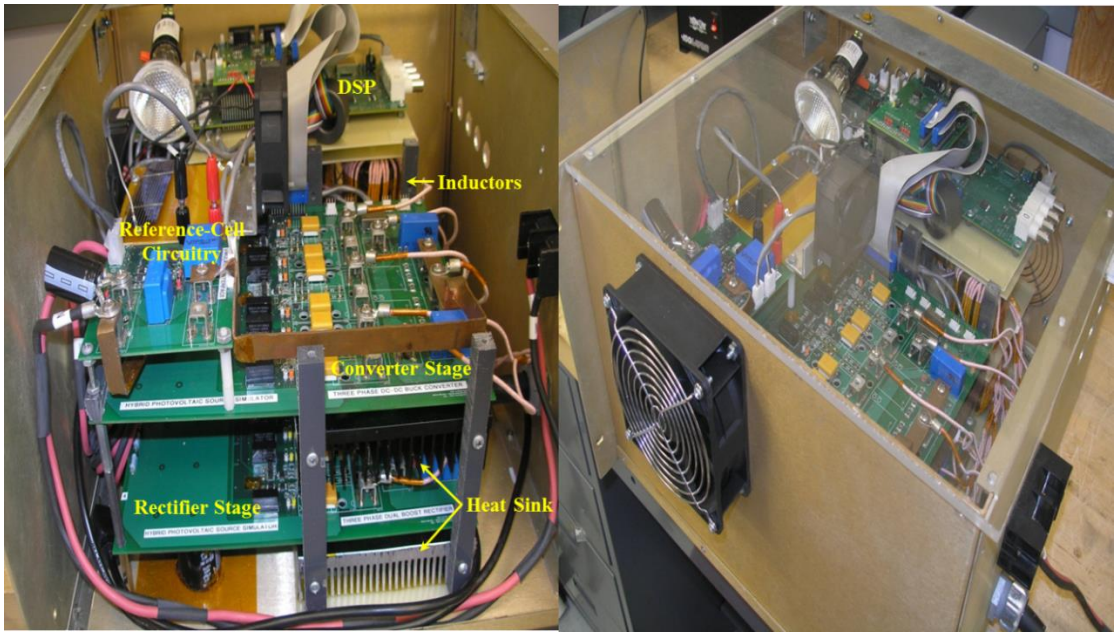

Figure 3.15 Hardware prototype of the proposed photovoltaic source simulator

Table 3-2 TECHNICAL SPECIFICATIONS OF THE PROPOSED PV SOURCE SIMULATOR

ac-dc Rectifier Stage (Boost)			
Electrical Specifications		Component Parameters	
Input Voltage	120 V (RMS)	Inductance	950 μH
Output Voltage	375 V	Capacitance	2.35 mF
Power Factor	1.0	Main Switch	FCA76N60
Sampling Time	30 μs	Main Diode	STTH6004W
Switching Frequency	33 kHz	Gate Driver	MC33153D
dc-dc Converter Stage (Buck)			
Electrical Specifications		Component Parameters	
Input Voltage	375 V	Inductance	450 μH
Output Voltage	(0-200) V	Capacitance	100 μF
Output Current	(0-20) A	Main Switch	IPW60R045CP
Sampling Time	30 μs	Main Diode	STTH6004W
Switching Frequency	33 kHz	Gate Driver	MC33153D

Fig. 3.16 shows three sets of experimental current-voltage and power-voltage output characteristic of the proposed PV source simulator connected to an electronic load (resistive mode). The generated curves represent the amplified non-linear characteristic of the reference-cell. Fig. 3.16(a) displays the curves at different irradiance levels where the reference-cell short-circuit current $i_{sc,cell}$ is directly proportional to the light intensity. Fig. 3.16(b) displays the curves at different reference-cell temperatures. Reverse bias saturation current of the PV reference-cell determines the cell's open-circuit voltage $v_{oc,cell}$ and is inversely proportional to the temperature of the cell [75]. Fig. 3.16(c) displays the curves of two reference cells when one of them is partially shaded, which results multiple MPPs. This curve is generated utilizing two reference-cells connected in series with bypass diodes (Model: LX2400) anti-parallel connected with each cell. The partial shading effect emulation is a necessary feature of PV source simulators for the evaluation of solar power conditioning system performance and their MPPT algorithms.

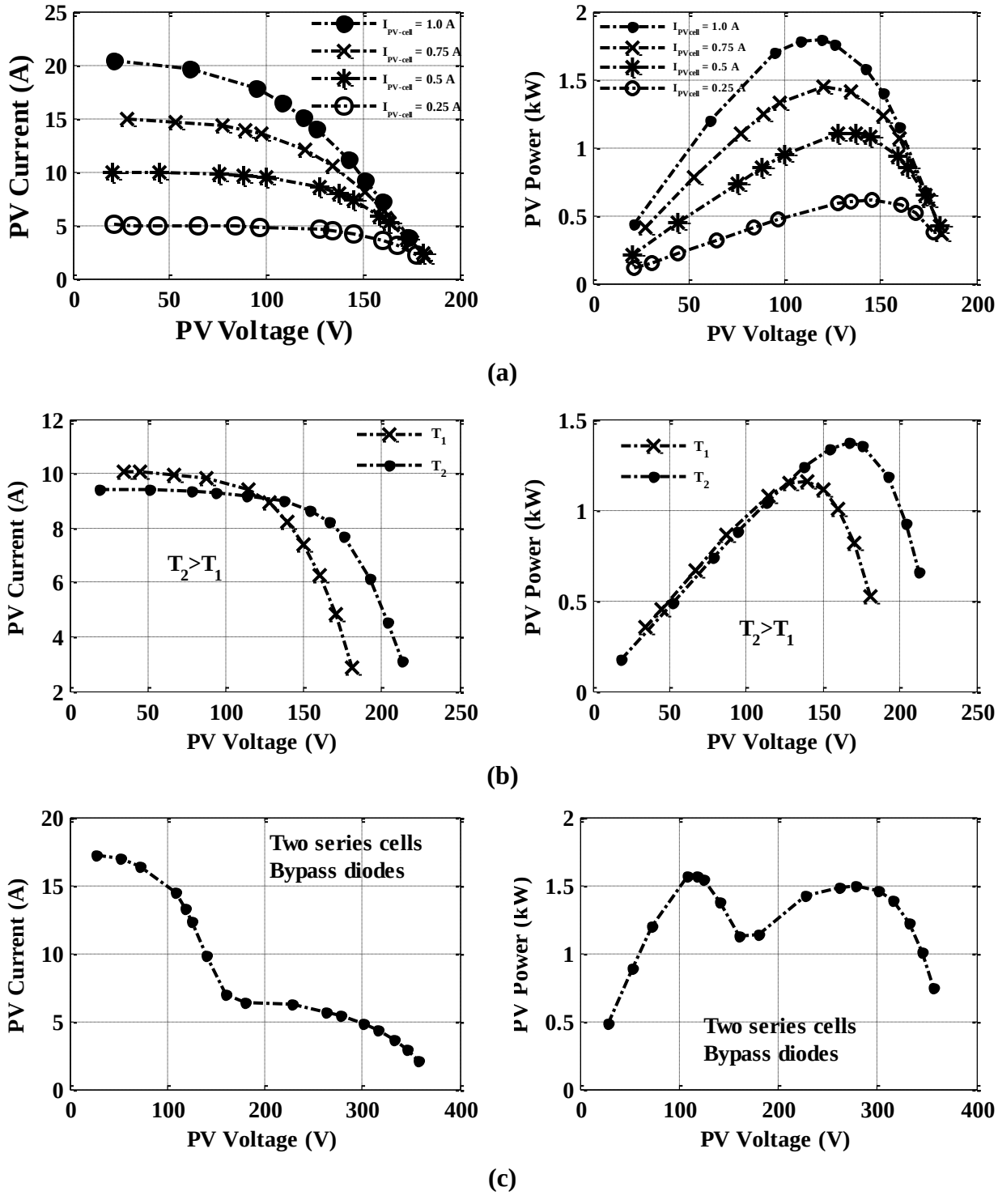

Figure 3.16 Experimental output current-voltage and power-voltage characteristic of the proposed PV source simulator; **(a)** Characteristic at different irradiance levels, **(b)** Characteristic at different temperature levels, and **(c)** Characteristic with partial shading effect and bypass diodes

Fig. 3.17 presents the experimental waveforms showing the detailed steady-state performance of the proposed two-stage PV source simulator connected to a resistive load. Fig. 3.17(a) shows the three-phase ac input currents $i_a, i_b,$ and i_c of the ac-dc rectifier stage, and the dc-link voltage v_{dc}, whereas fig. 3.17(b) shows the three-phase dc output inductor currents $i_1, i_2,$ and i_3, of the dc-dc converter stage and their total current i_{pv}. Well-designed inductors and power-stage board layout allow balanced currents at input and output sides of the proposed system. Fig 3.17(c) shows input phase voltage and input phase current of the ac-dc rectifier stage where a unity power factor is achieved. The total harmonic distortion (THD) of the input phase current is below 3.6 % at the rated power. Fig. 3.17(d) shows the relationship between phase current direction and phase duty cycles (upper and lower) of the ac-dc rectifier as previously clarified in (1) and (2). The applied duty cycle is maximized at phase current zero crossing causing waveform distortion. Different techniques can be applied to enhance the quality of the waveform, which is beyond the scope of this research. Fig 3.18 shows the simulation waveforms of the detailed steady-state performance of the proposed PV source simulator. The simulated results match the experimental ones perfectly.

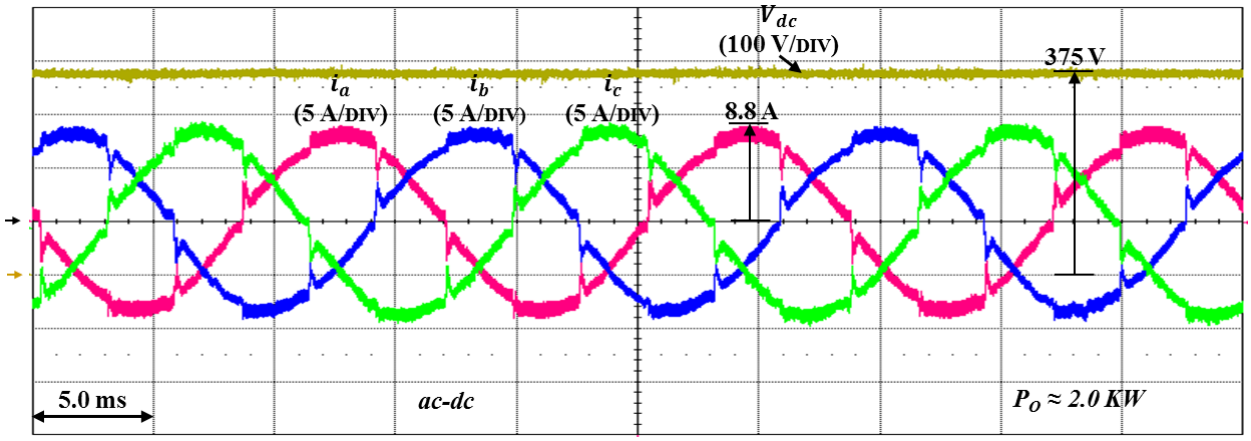

(a)

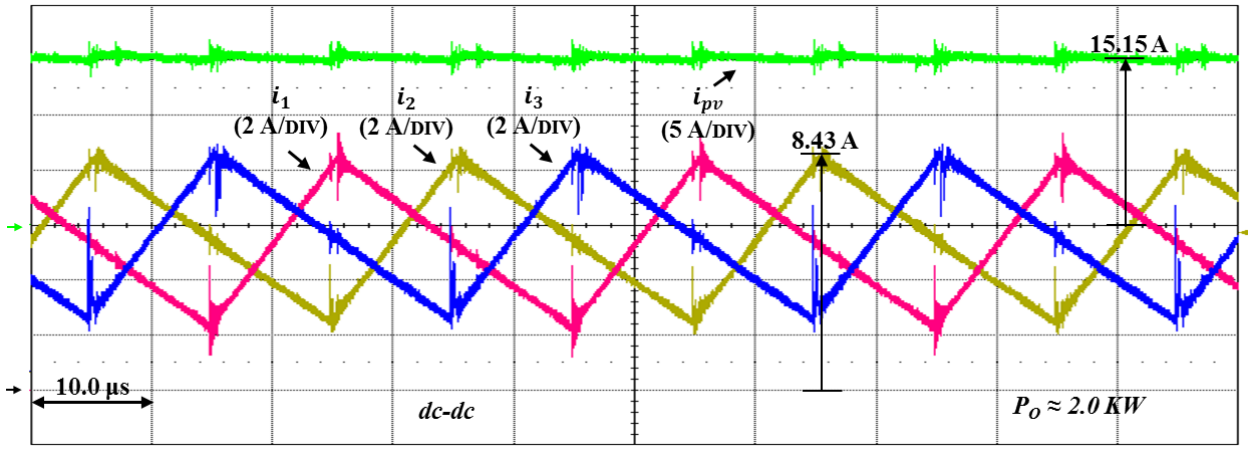

(b)

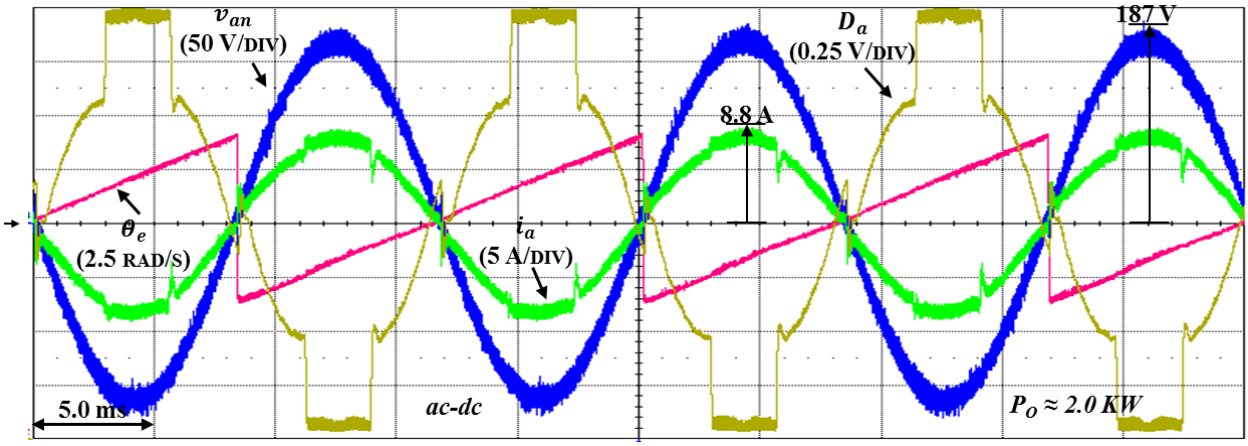

(c)

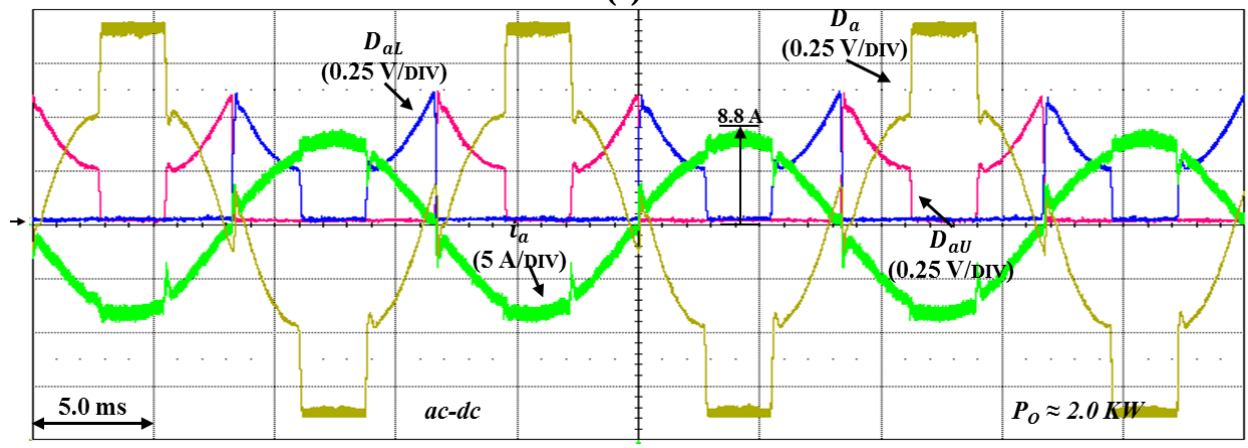

(d)

Figure 3.17 Experimental waveforms of the proposed PV source simulator: **(a)** Rectifier input currents and dc-link voltage, **(b)** Converter output currents and total output current, **(c)** Rectifier input phase voltage, input phase current, duty cycle, and electrical angle, and **(d)** Rectifier duty cycle, upper duty cycle, lower duty cycle, and input phase current

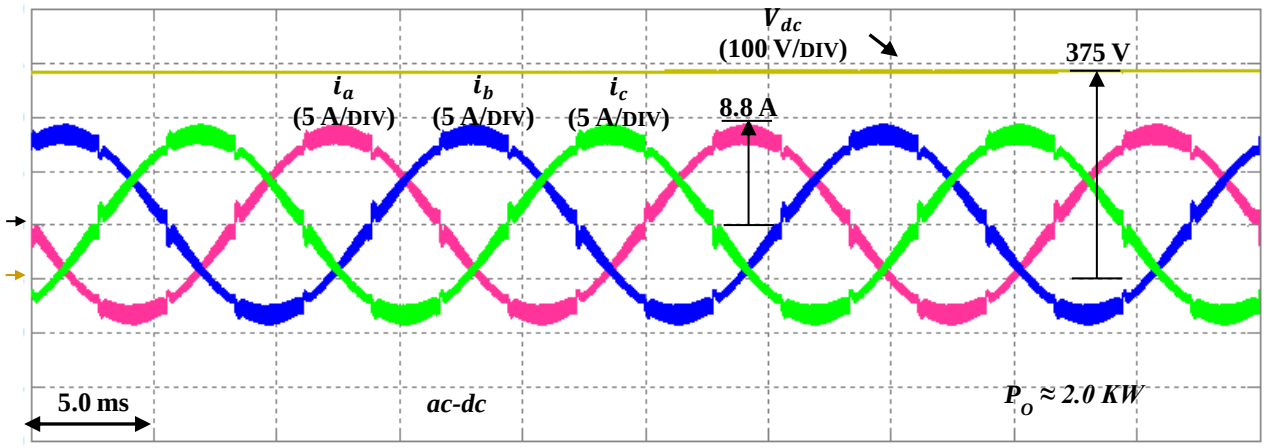
V_{dc}
(100 V/DIV)
375 V
i_a
(5 A/DIV)
i_b
(5 A/DIV)
i_c
(5 A/DIV)
8.8 A
5.0 ms
ac-dc
$P_o \approx 2.0$ KW

(a)

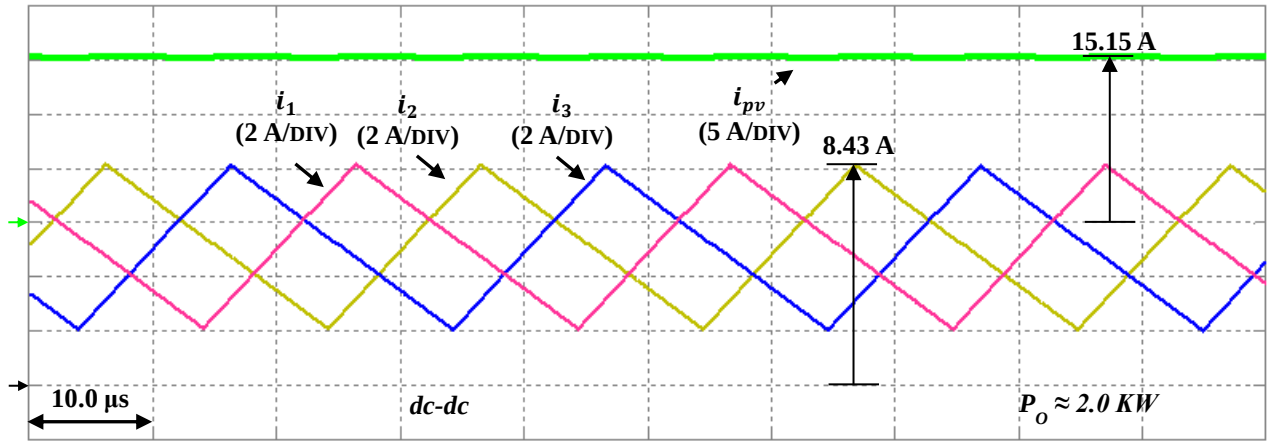
15.15 A
i_1
(2 A/DIV)
i_2
(2 A/DIV)
i_3
(2 A/DIV)
i_{pv}
(5 A/DIV)
8.43 A
10.0 µs
dc-dc
$P_o \approx 2.0$ KW

(b)

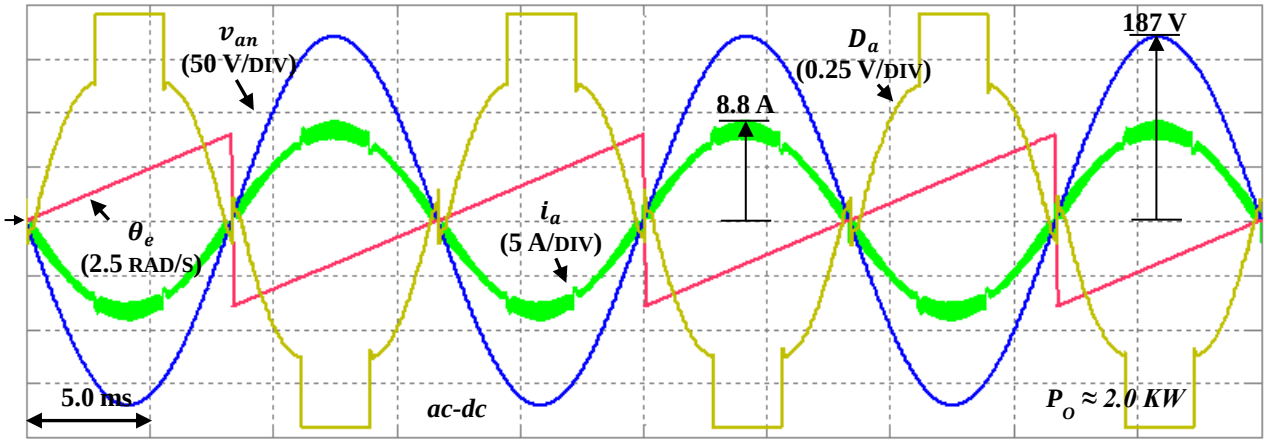
v_{an}
(50 V/DIV)
D_a
(0.25 V/DIV)
187 V
8.8 A
θ_e
(2.5 RAD/S)
i_a
(5 A/DIV)
5.0 ms
ac-dc
$P_o \approx 2.0$ KW

(c)

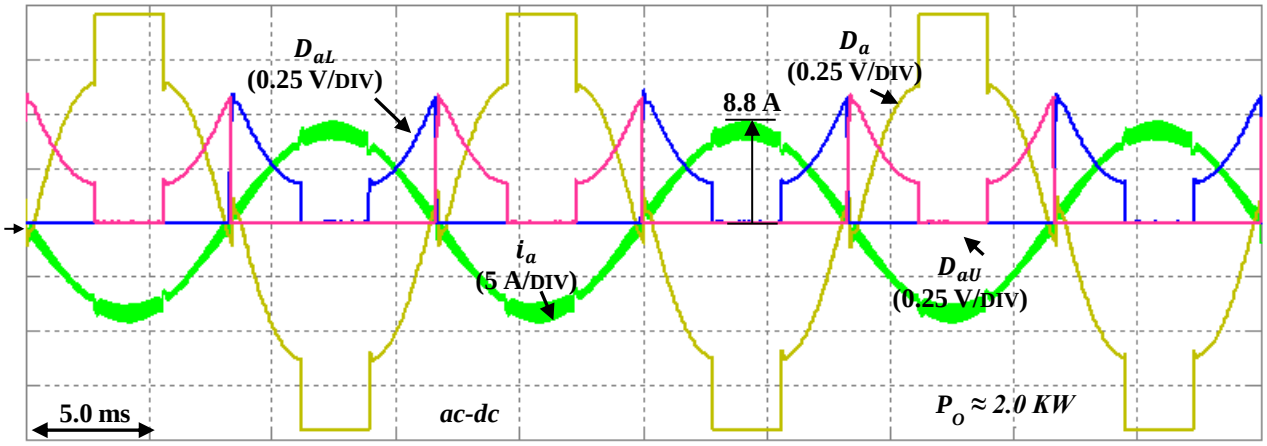

(d)

Figure 3.18 Simulated waveforms of the proposed PV source simulator: **(a)** Rectifier input currents and dc-link voltage, **(b)** Converter output currents and total output current, **(c)** Rectifier input phase voltage, input phase current, duty cycle, and electrical angle, and **(d)** Rectifier duty cycle, upper duty cycle, lower duty cycle, and input phase current

Fig. 3.19 and Fig. 3.20 show the startup experimental waveforms of grid input current, grid input voltage, and dc-link voltage when the simulator connects to the utility-grid. A startup circuitry of resistors (16 Ω per phase) in parallel with a mechanical relay is added in series between the grid voltage source and the proposed PV source simulator to protect the simulator hardware setup by limiting the grid peak inrush current to about 10 A. This high inrush current is caused due to the high capacitance value of the dc-link capacitor. Once the inrush current decays, the control system commands zero current while the limiting resistors are still in series. This step is important to protect the simulator hardware as the initial duty cycle of the main switch is maximized at startup. After that, the limiting resistors are bypassed by the mechanical relay.

Fig. 3.21 records the experimental transient response-time of each stage of the proposed PV source simulator for a step change from half to full load. Fig. 3.21(a) shows the dynamic response of the input phase current of the ac-dc rectifier and the dc-link voltage, whereas Fig. 3.21(b) shows the dynamic response of the total output current of the dc-dc converter. PV source

simulators should have a much faster transient response-time than that of the MPP tracking controller in order to act as actual PV generator in solar power conditioning systems. General time response of MPPT algorithms has been reported in literature to vary from 25 milliseconds to several seconds [76], [77]. The output current of the proposed system recovers within 3.2 milliseconds to ±5% of the steady-state value. This transient response-time of the proposed PV source simulator is about eight times faster than the fastest reported MPP tracking algorithm.

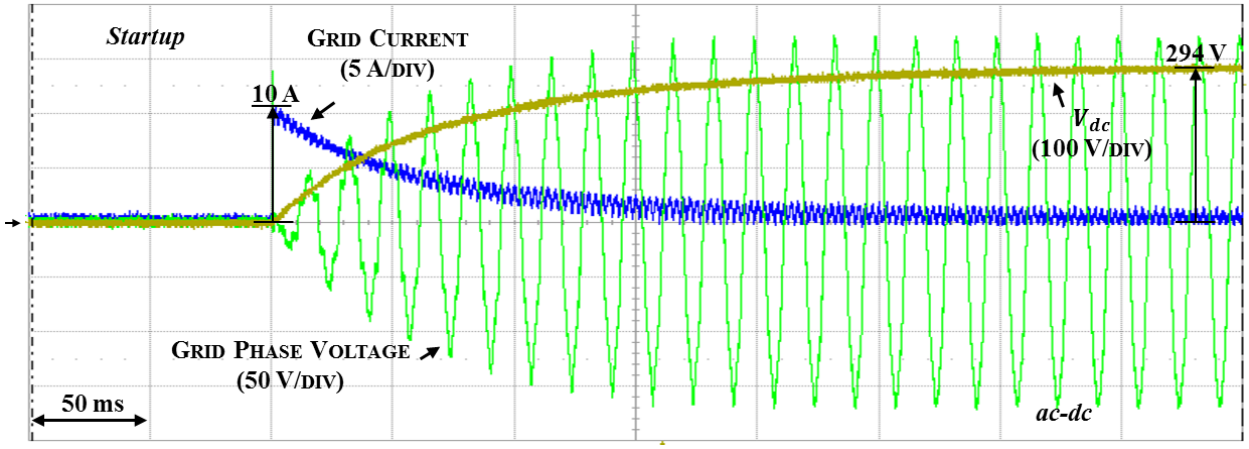

Figure 3.19 Startup experimental waveforms of grid current, grid phase voltage, and dc-link voltage when PV source simulator connects to the utility-grid

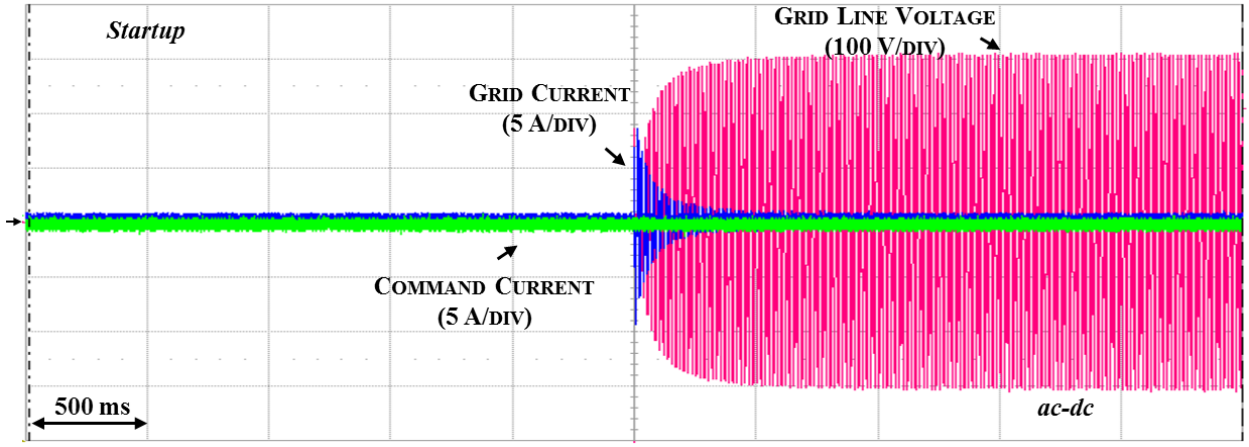

Figure 3.20 Startup experimental waveforms of grid current, grid voltage, and commanded current when PV source simulator connects to the utility-grid

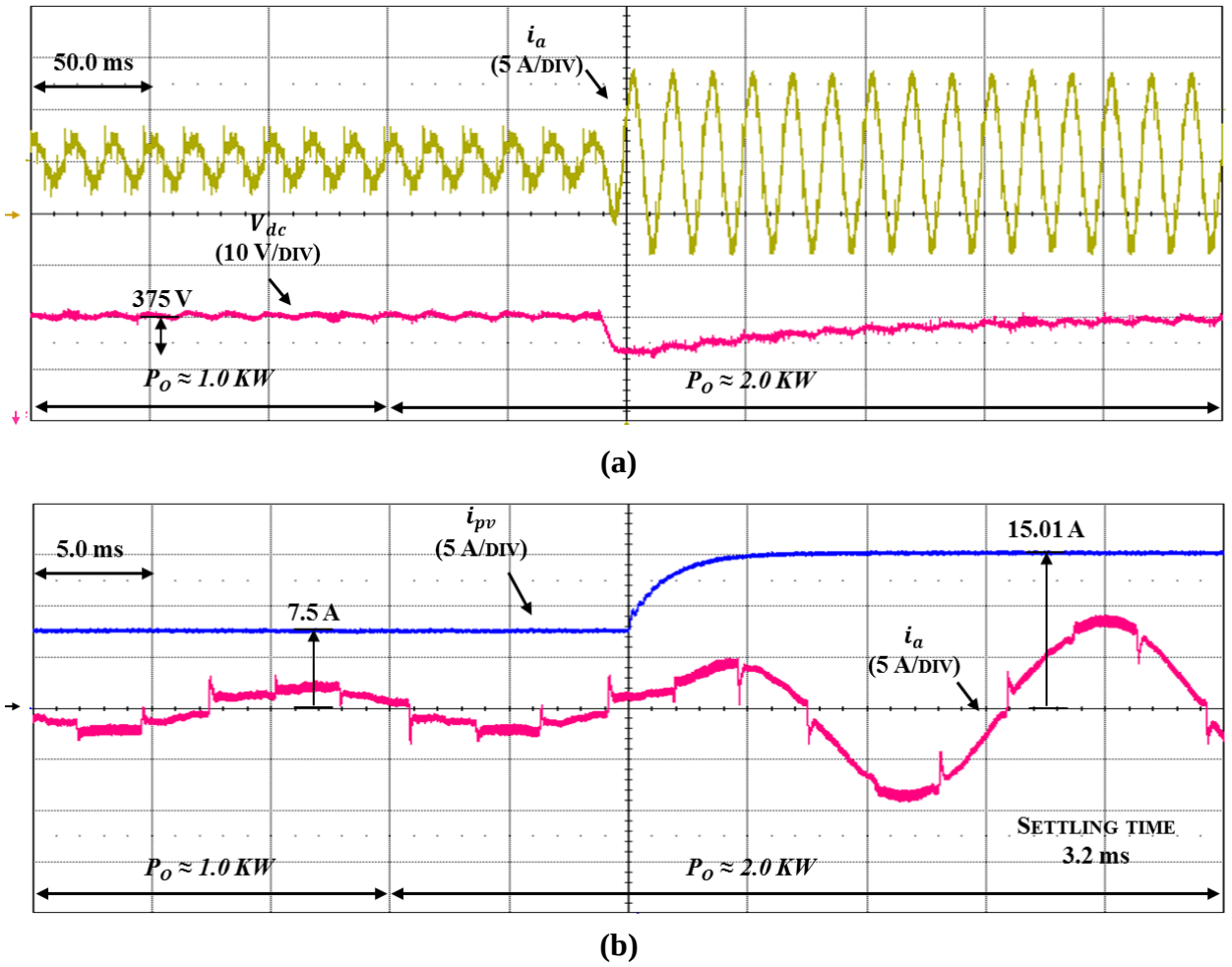

Figure 3.21 Transient response-time of the PV source simulator from half to full load; **(a)** Rectifier input phase current and dc-link voltage and **(b)** Converter total output current

Fig. 3.22 shows the proposed PV source simulator efficiency curve including the ac-dc rectifier stage and the dc-dc converter stage along with corresponding operating points. The efficiency was measured using a digital power meter with 0.1% accuracy (Model: Yokogawa WT1600). The efficiency of the proposed two-stage simulator peaks at 96.6% and the efficiency at the peak MPP is 96.4%. This efficiency is much higher than the power-stage efficiency of Chroma commercial PV source simulator (Model: 62150H-600S), which is reported to be typically 87% [78].

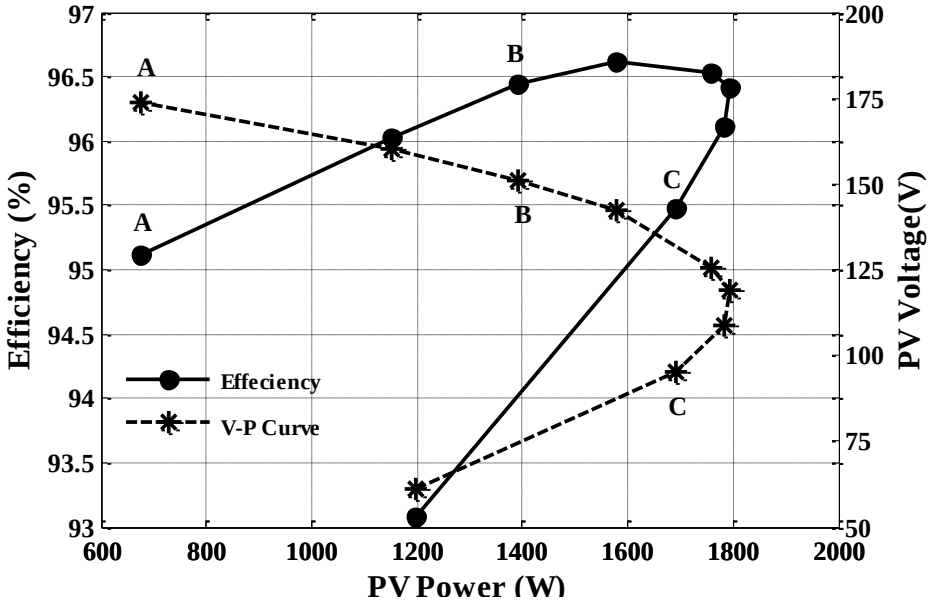

Figure 3.22 Measured PV source simulator efficiency including rectifier and converter power-stages with the corresponding operating points

3.5 SUMMARY

In this chapter, a new type of grid-connected PV source simulator has been proposed and thoroughly described. The proposed simulator has been used to precisely emulate the static and the dynamic characteristic of actual PV systems at different load and environmental conditions including the effect of partial shading. The simulator uses a high-bandwidth real-time analog reference circuit to extract the reference curves, which are then digitally processed to emulate the characteristic of a high power system. The performance of the proposed simulator has been successfully evaluated when connected to a resistive load in steady-state and transient conditions.

The proposed PV source simulator consists of two power switching stages. The three-phase ac-dc rectifier stage is a new dual boost topology that is reliable and highly efficient, whereas the second-stage, the three-phase dc-dc converter helps improve system transient response though producing low output voltage and current ripples. The experimental results illustrate the proposed system has achieved high two-stage efficiency and fast transient response-time relative to MPP tracking algorithms.

With a potential of high reliability, high efficiency, and ultrafast transient response, the proposed system architecture is well suited for high power PV source simulator. Further improvement of the simulator response can be obtained with the increase of the number of phases of the output dc-dc stage.

CHAPTER 4

DYNAMIC PERFORMANCE EVALUATION OF SOLAR POWER CONDITIONING SYSTEMS AND MPPT ALGORITHMS USING PHOTOVOLTAIC SOURCE SIMULATOR

4.1 INTRODUCTION

This chapter focuses on two main subjects: (i) closed-loop output impedance of PV source simulators and (ii) dynamic performance evaluation of solar power conditioning systems using PV source simulator. The closed-loop output impedance of PV source simulator should match closely the impedance profile of actual PV generator. This profile should exhibits high impedance at voltages lower than the MPP (similar to a current source) and low impedance at voltages higher than the MPP (similar to a voltage source). Moreover, the closed-loop output impedance should not contain resonant peaks originating from the use of the LC output filter of the dc-dc converter stage. The closed-loop output impedance of the PV source simulators proposed in Chapter 2 and 3 is verified and compared to the impedance of actual PV generator at different operating conditions including CC and CV.

The ultimate purpose of designing a PV source simulator is to evaluate the performance of solar power conditioning systems in transient and in steady-state conditions. Different commercial and non-commercial solar power conditioning systems have been evaluated along with their MPPT algorithms using the proposed PV source simulator. Moreover, the evaluated systems have been tested with actual PV generator as well to justify the validity of the PV source simulator as a replacement for actual PV generator.

4.2 SOLAR POWER CONDITIONING SYSTEMS: OVERVIEW

A solar power conditioning system converts the variable direct-current output of PV arrays or modules into an alternating-current to be fed to the utility-grid or to off-grid electrical network. Solar power conditioning systems can be classified into three main groups: (i) center-based systems, (ii) string-based systems, and (iii) module-based systems [79]. The center based-system includes mainly a centralized three-phase PV inverter, which interface large number of PV modules to the utility-grid as shown in Fig. 4.1(a) [80], [81]. The high dc input voltage of this centralized PV inverter may vary significantly as the PV array characteristic varies substantially with environmental conditions [82]. This wide dc input voltage range affects the inverter operation and efficiency. To overcome this issue, an intermediate dc-dc converter stage is added between the PV array and the PV inverter as shown in Fig. 4.1(b) to fix the dc input voltage of the PV inverter and hence optimize its efficiency [83].

A string-based system is a reduced version of center-based system. In this approach, a string PV inverter connects a single PV string (PV modules connected in series) to the utility-grid as shown in Fig. 4.2(a). This approach helps optimize the performance of each string independently and hence maximize the overall system efficiency relative to the center-based systems. However, the single-string system has a power capability limit due to the limited possible number of series connected strings [84]. The multi-string PV inverter depicted in Fig. 4.2(b) is a further improvement of the single-string inverter. This scenario combines the advantages of center-based systems and single-string systems. Each PV string is interfaced with its own dc-dc converter to a centralized dc-ac PV inverter. This helps optimize the MPP of each string and increase system reliability [85].

Module-based system integrates the PV module and the PV inverter in one unit. This approach helps reduce partial shading effect and module mismatch [86]. Moreover, module-based systems can be easily enlarged due to their modular structure. Two existing configurations of module-based systems are known as depicted in Fig. 4.3(a) and Fig. 4.3(b): (i) distributed dc-ac micro-inverter and (ii) distributed dc-dc micro-converter [87]. In either configuration, the dc-dc stage optimizes the local MPP of each PV module whereas the dc-ac stage controls the power flow to the utility-grid.

Cell-based systems are new technology under development. In this system a PV inverter is used to interface a single PV cell to the utility-grid. The difficulty is to design an inverter that will invert a low-voltage (0.5 V~ 1.0 V) to an appropriate level of the utility-grid [88].

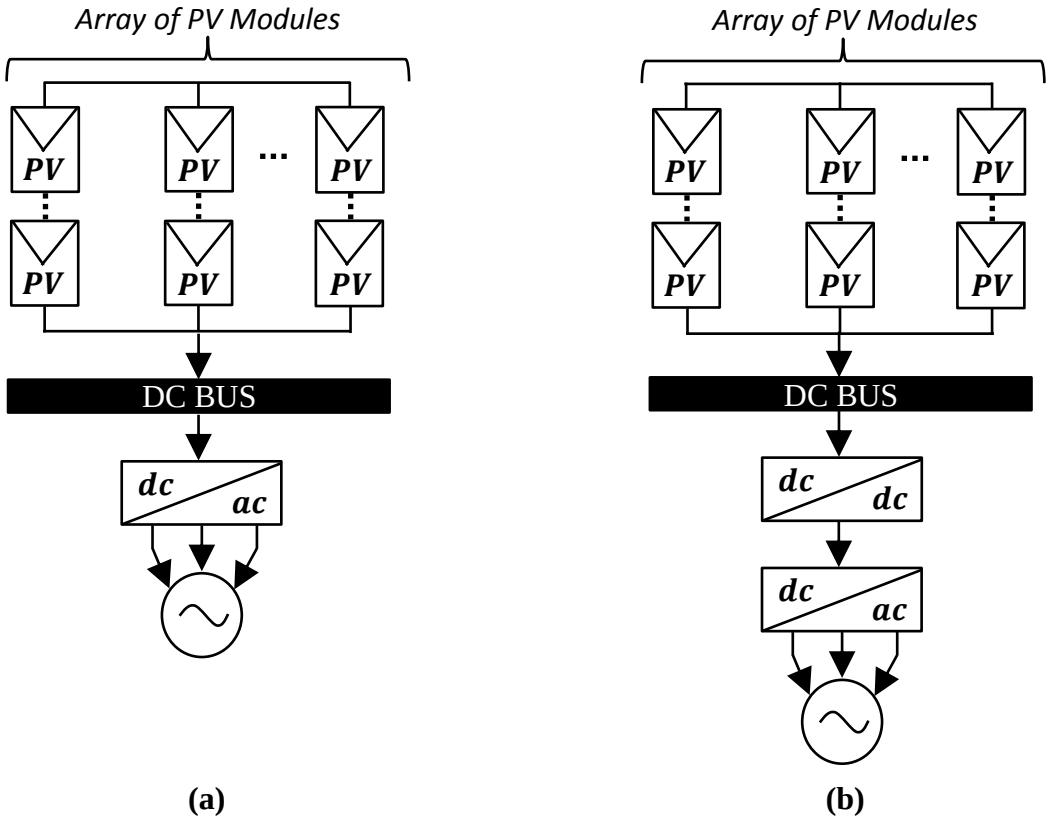

Figure 4.1 Center-based solar power conditioning system configuration; **(a)** Centralized dc-ac PV inverter and **(b)** Centralized dc-ac PV inverter with intermediate dc-dc converter

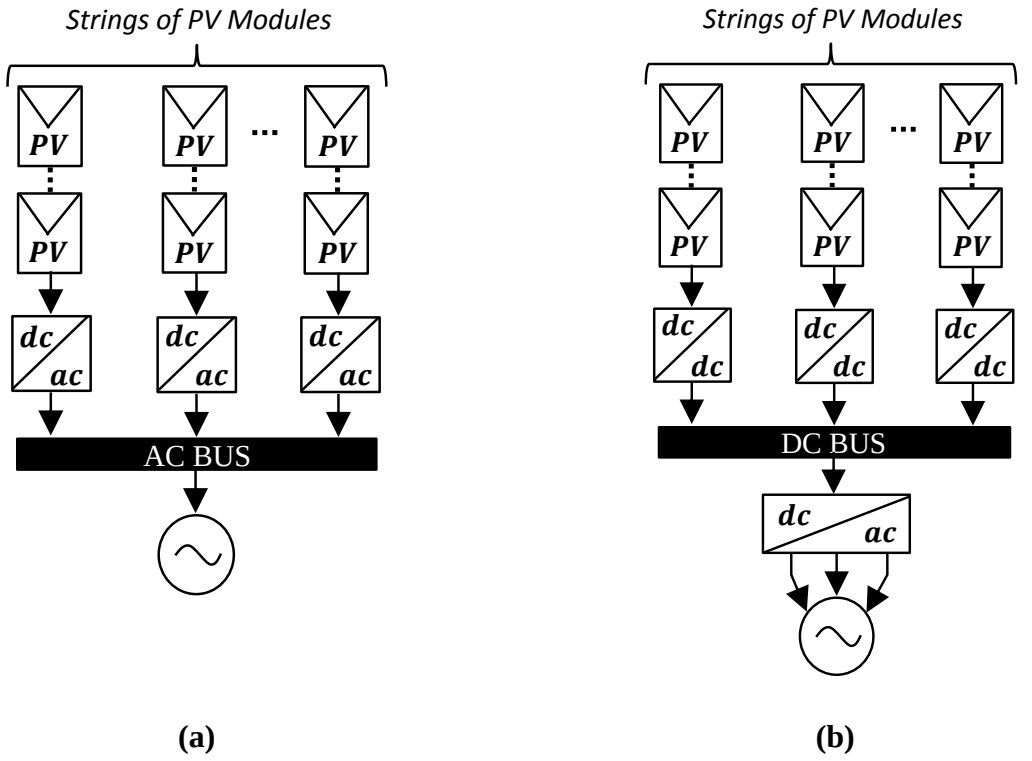

(a) **(b)**

Figure 4.2 String-based solar power conditioning system configuration; **(a)** Single string dc-ac PV inverter and **(b)** Multi-string dc-ac PV inverter

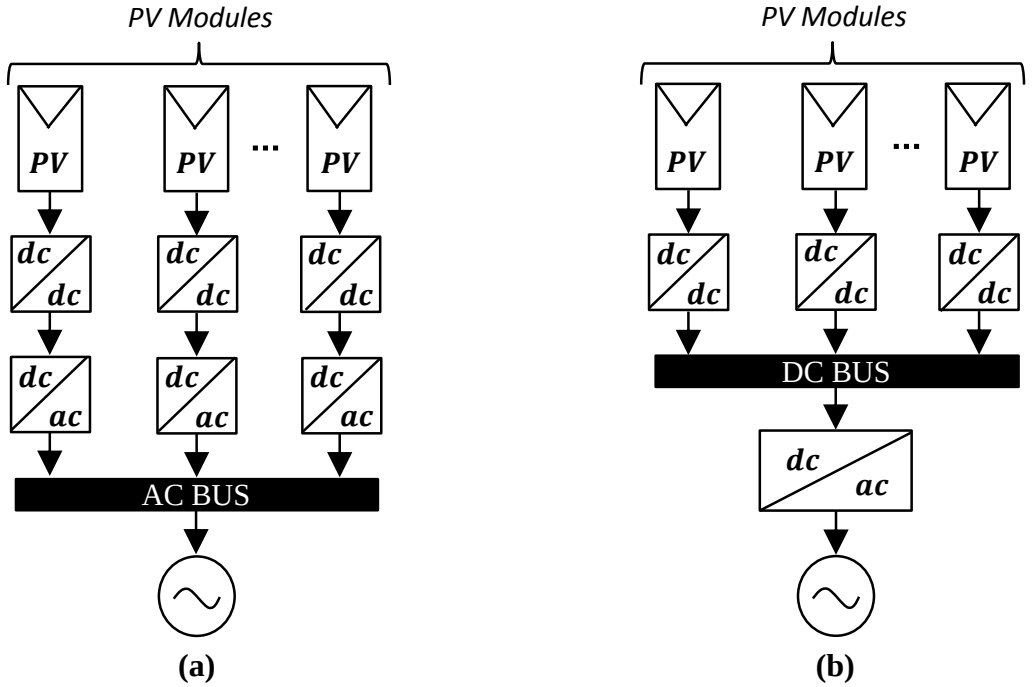

(a) **(b)**

Figure 4.3 Module-based solar power conditioning system configuration; **(a)** Distributed dc-ac PV micro-inverter and **(b)** Distributed dc-dc PV micro-converter

Throughout this chapter, different commercial and non-commercial solar power conditioning systems and their associated MPPT algorithms are tested and evaluated using the proposed PV source simulator in Chapter 3. This simulator system with its fast response-time, high efficiency, and output impedance matching is more adequate for solar power conditioning systems evaluation than the design in Chapter 2. The evaluation process includes startup performance and MPPT algorithm convergence speed during startup and during transients. Moreover, the evaluation process helps justify the validity of the proposed PV source simulator as a replacement for actual PV generator. The evaluated systems detailed technical specifications are summarized in table 4-1.

Table 4-1 TECHNICAL SPECIFICATIONS OF EVALUATED SOLAR POWER CONDITIONING SYSTEMS

Enphase Micro-Inverter (M175-24-240)			
Electrical Specifications		Electrical Specifications	
Input Voltage	54 V (MAX)	Input Power	230 W
Output Voltage	240 V	Output Power	175 W
Input Current	8 A (MAX)	Power Factor	> 0.95
MPPT Range	25 V – 40 V	Peak Efficiency	95.0 %
Enphase Micro-Inverter (M190-72-240)			
Electrical Specifications		Electrical Specifications	
Input Voltage	56 V (MAX)	Input Power	230 W
Output Voltage	240 V	Output Power	190 W
Input Current	10 A (MAX)	Power Factor	> 0.95
MPPT Range	22 V – 40 V	Peak Efficiency	95.5 %
SMA Utility Interactive Inverter (SB 5000-US)			
Electrical Specifications		Electrical Specifications	
Input Voltage	600 V (MAX)	Input Power	5300 W
Output Voltage	208 V	Output Power	5000 W
Input Current	21 A (MAX)	Power Factor	1
MPPT Range	250 V – 480 V	Peak Efficiency	96.8 %
Distributed Micro-Converter (Non-commercial)			
Electrical Specifications		Electrical Specifications	
Input Voltage	55 V (MAX)	Input Power	310 W
Output Voltage	320 V	Output Power	300 W
Input Current	15 A (MAX)	Power Factor	-
MPPT Range	20 V – 40 V	Peak Efficiency	97.8 %

4.3 CLOSED-LOOP OUTPUT IMPEDANCE OF PV SOURCE SIMULATORS

The closed-loop output impedance of PV source simulators is a critical design aspect justifies the validity of the simulator as a substitute to actual PV generator. The impedance of actual PV generator in frequency domain shows passive-like characteristic as depicted in Fig. 4.4. A crystalline PV cell (0.5 W) is used with full illumination to obtain this characteristic at CC and CV conditions .The measurement is carried out using a Venable frequency response analyzer (Model: 3210). The magnitude of the impedance is fairly constant in low-frequency range resembling resistive characteristic, whereas in high-frequency range, the impedance magnitude and phase decreases resembling capacitive characteristic. Moreover, the impedance is operating point dependent and varies with illumination level [89].

To verify the output impedance of the proposed PV source simulators, the proposed systems are modeled using their closed-loop switching models and the closed-loop output impedance is simulated and verified at different operating conditions including CC and CV. Fig. 4.5 shows the simulated closed-loop output impedance of the PV source simulator proposed in Chapter 2; the impedance profile did not match the output impedance of actual PV generator due to the double resonant peaks of the two-stage LC filter. Advanced control techniques can be applied to eliminate the effect of the output filter on the impedance characteristic. Fig. 4.6 shows the measured closed-loop output impedance of the PV source simulator proposed in Chapter 3; the impedance profile matches closely with the output impedance of actual PV generator. An impedance measurement system is built and designed to measure the closed-loop output impedance of the PV source simulator proposed in Chapter 3. The measurement system includes: (i) Venable frequency analyzer (Model: 3120), (ii) high power linear amplifier, and (iii) injection transformer. The perturbation signal of the Venable frequency analyzer (Model: 3120) is injected

into an ac linear power supply from Pacific Electronic Enterprise (Model: 300-B) for amplification, the output of the linear supply is injected through a step up transformer into the system. The injection transformer is capable of handling large amounts of dc current without saturation. After that, the output voltage and output current of the proposed PV source simulator are measured and fed back to the analyzer to calculate the system impedance. Fig. 4.7 illustrates the proposed impedance measurement setup. For all operating points, the output impedance is constant in the low-frequency range resembling resistive characteristic, and after 100 Hz the magnitude and phase of the output impedance decreases resembling capacitive characteristic. The results show that the magnitude of the simulator's output impedance decreases as the operating point shifts from CC to CV. The magnitude is high at the CC condition because the rate of change in voltage is high and the rate of change in current is low (current source characteristic). Oppositely, the magnitude is low at the CV condition as the rate of change in voltage is low and the rate of change in current is high (voltage source characteristic). Moreover, the phase of the output impedance at all operating points is between $\pm 90^{o}$. Accordingly, the proposed PV source simulator in Chapter 3 can be claimed as a substitute for actual PV systems. The profile of the impedance of this simulator matches the impedance measurement of the PV generator as well as the commercial PV simulator characterized in [90] as 'device A'. The major difference among the closed-loop output impedance of this simulator, the output impedance actual PV generator, and the closed-loop output impedance of commercial PV simulator in [90] is the frequency at which the gain drops off. The frequency is dependent on the dynamic capacitance of the PV cell(s), which is a function of cell material and cell physical size. Different PV cells in size and material will have different capacitances and as a result the magnitude and the phase will be highly affected.

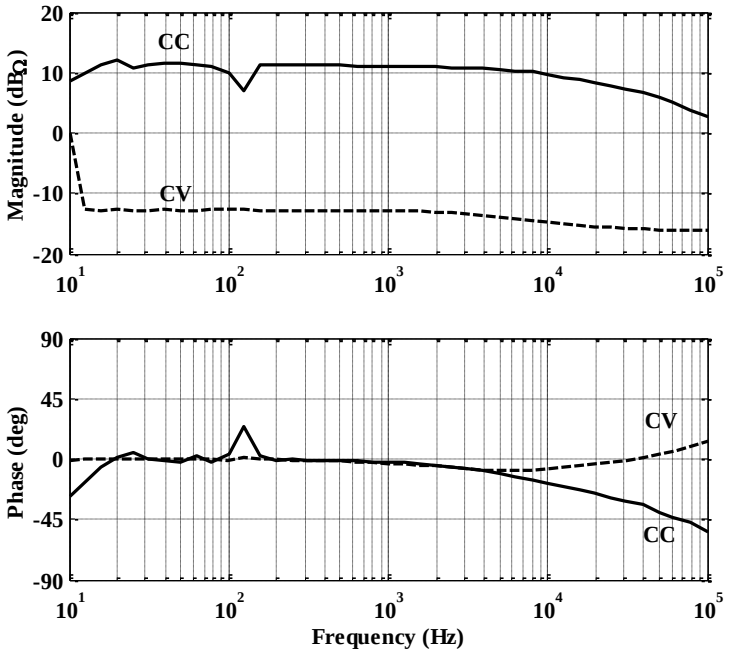

Figure 4.4 Measured output impedance of a crystalline PV cell at constant current and constant voltage conditions under illumination

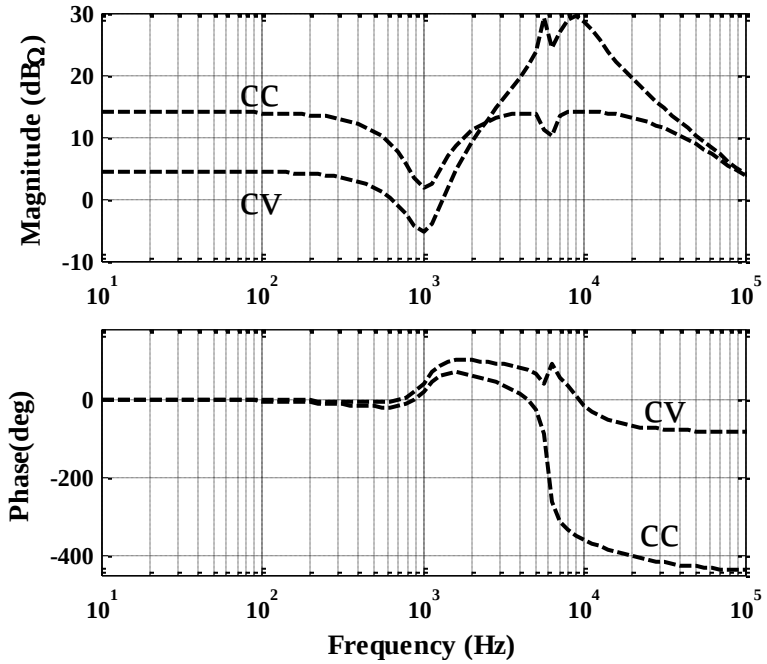

Figure 4.5 Simulated closed-loop output impedance of the proposed photovoltaic source simulator in Chapter 2 at constant current and constant voltage conditions

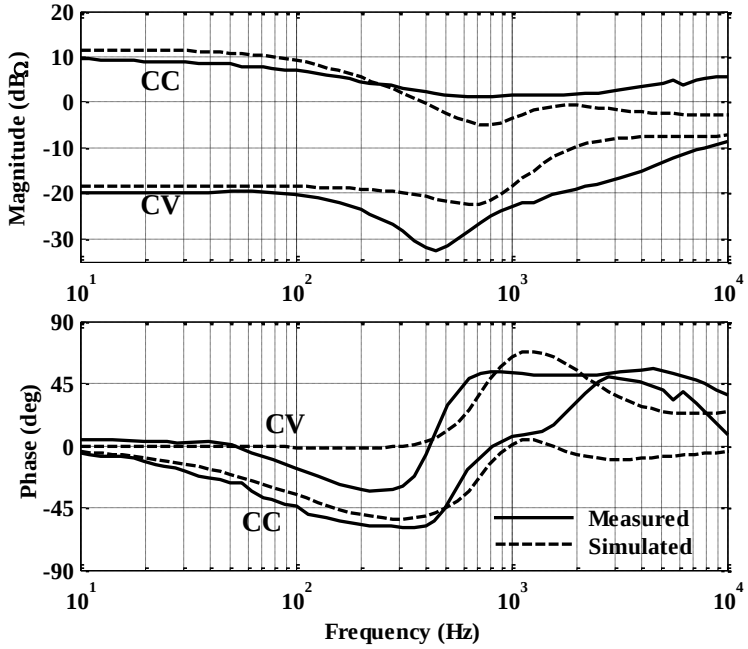

Figure 4.6 Measured closed-loop output impedance of the proposed photovoltaic source simulator in Chapter 3 at constant current and constant voltage conditions

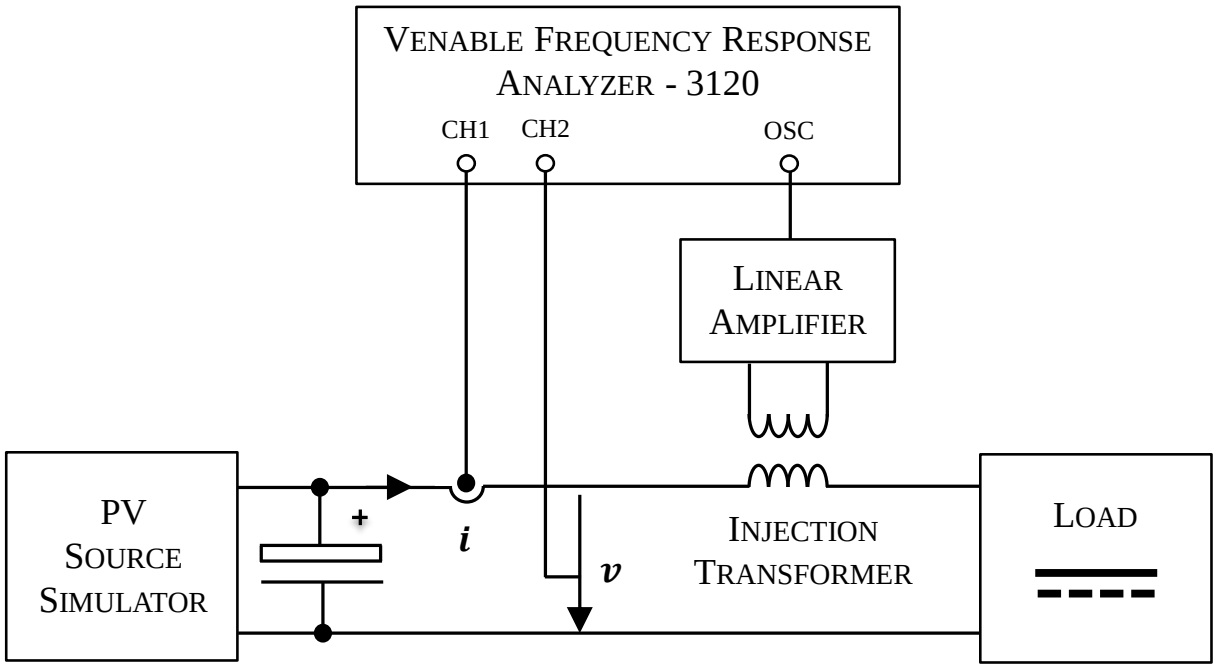

Figure 4.7 Experimental test setup for measuring the closed-loop output impedance of the proposed PV source simulator

4.4 EVALUATION OF COMMERCIAL SOLAR POWER CONDITIONING SYSTEMS

In this section, the static and dynamic performance of two commercial distributed dc-ac PV micro-inverters [91], [92] and a commercial centralized dc-ac PV inverter [93] is evaluated using: (i) The PV source simulator proposed in Chapter 3 and (ii) Actual PV generator. The process includes the evaluation of system operation during startup, transient, and steady-state conditions. This helps evaluate and compare the performance of different solar power conditioning systems and their associated MPPT algorithms. Moreover, this evaluation process helps optimize the design of the proposed PV source simulator and justify its validity as a replacement for actual PV generator.

4.4.1. EVALUATION OF DISTRIBUTED DC-AC PV MICRO-INVERTER

To optimize the control-loop design of the proposed PV source simulator and to evaluate the dynamic and static performance of a distributed grid-connected dc-ac PV micro-inverter (Model: M175-24-240) and it is associated MPPT algorithm three tests have been carried out: (i) Evaluate the dynamic and static performance of the PV micro-inverter and its ability to track the MPP at startup, steady-state, and at different weather conditions when connected to the proposed PV source simulator, (ii) Evaluate the dynamic and static performance of the PV micro-inverter and its ability to track the MPP at startup, steady-state, and at different weather conditions when connected to an actual PV generator (Model: CS6P-240P), and (iii) Optimize the control-loop bandwidth design of the proposed PV source simulator when connected to the distributed dc-ac PV micro-inverter.

Fig. 4.8(a) and Fig. 4.8(b) illustrate the startup performance of the distributed dc-ac PV micro-inverter connected to the proposed PV source simulator and to actual PV generator, respectively. In both cases, the PV micro-inverter tracks the expected MPP precisely and reaches steady-state within 800 milliseconds. The input voltage of the PV micro-inverter changes from open-circuit voltage to voltage at the MPP, whereas its input current changes from zero to the current at the MPP.

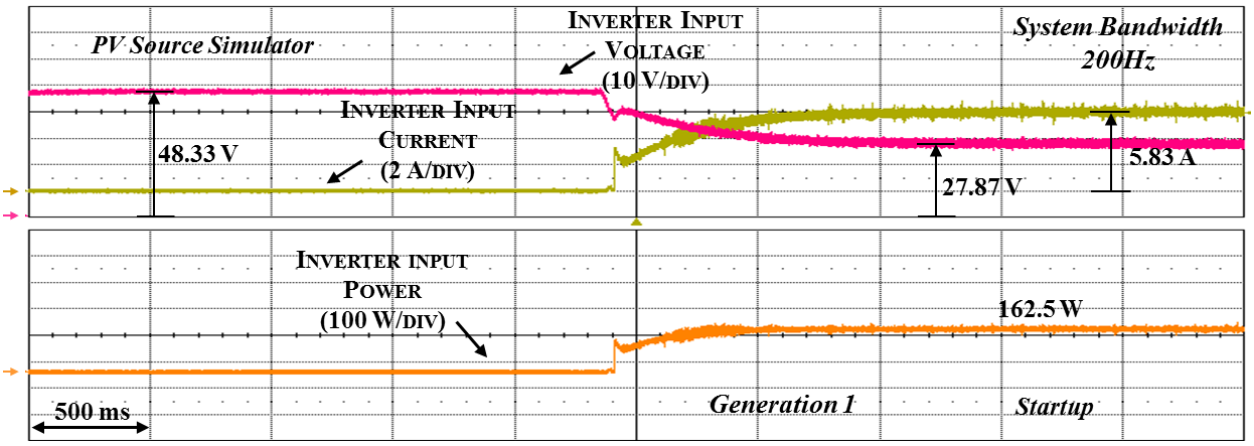

(a)

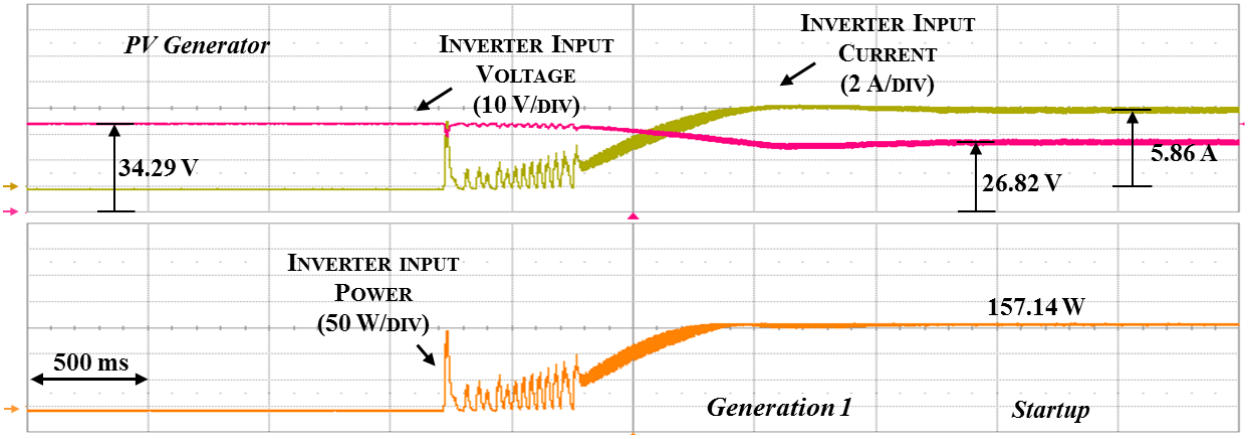

(b)

Figure 4.8 Dynamic and static performance evaluation of commercial distributed dc-ac PV micro-inverter (Generation 1); **(a)** Startup waveforms and MPP tracking using PV source simulator and **(b)** Startup waveforms and MPP tracking using actual PV generator

Figs 4.9(a) and Fig. 4.9(b) show the response of the PV micro-inverter as the irradiance level changes from high to low intensity when it is connected to the proposed PV source simulator and to actual PV generator, respectively. The MPP shifts down (input current decrease and input voltage increase) and the micro-inverter tracks the new point appropriately. The tested system functioned correctly when connected to the proposed PV source simulator and to the actual PV generator as the MPP is pursued in startup, steady-state, and transient conditions.

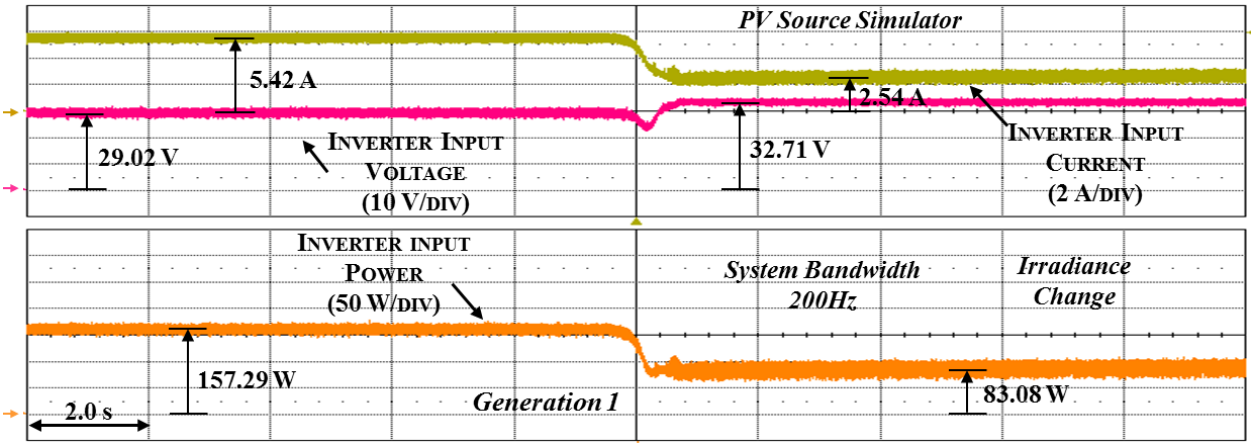

(a)

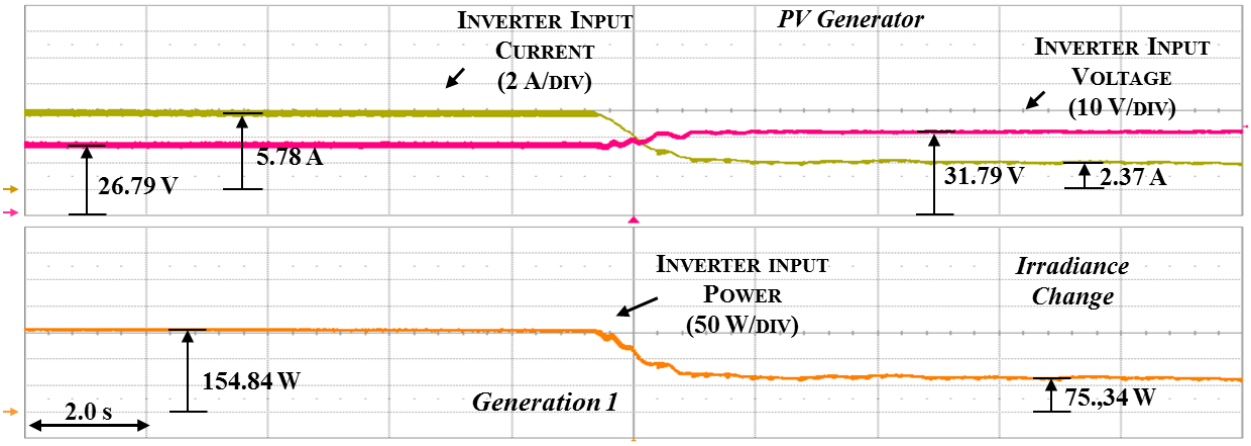

(b)

Figure 4.9 Dynamic and static performance evaluation of commercial distributed dc-ac PV micro-inverter (Generation 1); **(a)** MPP tracking with irradiance change using PV source simulator and **(b)** MPP tracking with irradiance change using actual PV generator

In order to optimize the control-loop bandwidth design of the proposed PV source simulator, a step up and down in the PV source simulator bandwidth has been executed while running the grid-connected PV micro-inverter. The PV source simulator base bandwidth is set to 200 Hz. The base bandwidth is the bandwidth of the analog outer-reference loop, which is one-tenth the bandwidth of the digital inner-current loop. Fig 4.10(a) shows the input voltage, input current, and input power of the micro-inverter when the PV source simulator bandwidth changes from 200 Hz to 50 Hz. The MPPT algorithm of the micro-inverter is not able to track the MPP as the PV source simulator dynamics are too slow relative to the MPPT controller of the PV micro-inverter. The proposed PV source simulator is not providing the right reference value to the PV micro-inverter in this case. Fig. 4.10(b) shows the input voltage, input current, and input power of the PV micro-inverter when the PV source simulator bandwidth changes from 200 Hz to 500 Hz. The MPPT algorithm of the micro-inverter is not able to track the MPP as the PV source simulator high gain increases the outer-reference loop bandwidth, and hence causes an interaction with the inner-current loop of the PV source simulator. The proposed PV source simulator is not providing the right reference value to the PV micro-inverter in this case as well. In conclusion, a minimum and a maximum PV source simulator bandwidth limits have to be achieved in order for the MPPT algorithm of the micro-inverter to perfectly track the MPP at startup, steady-state, and at different environmental and weather conditions. The upper limit of the bandwidth is constrained by the switching frequency of the PV source simulator and the lower limit of the bandwidth is constrained by the speed of the MPPT algorithm of the solar PV micro-inverter. There, the overall control-loop bandwidth of the proposed PV source simulator is optimally designed in the range of 200 Hz.

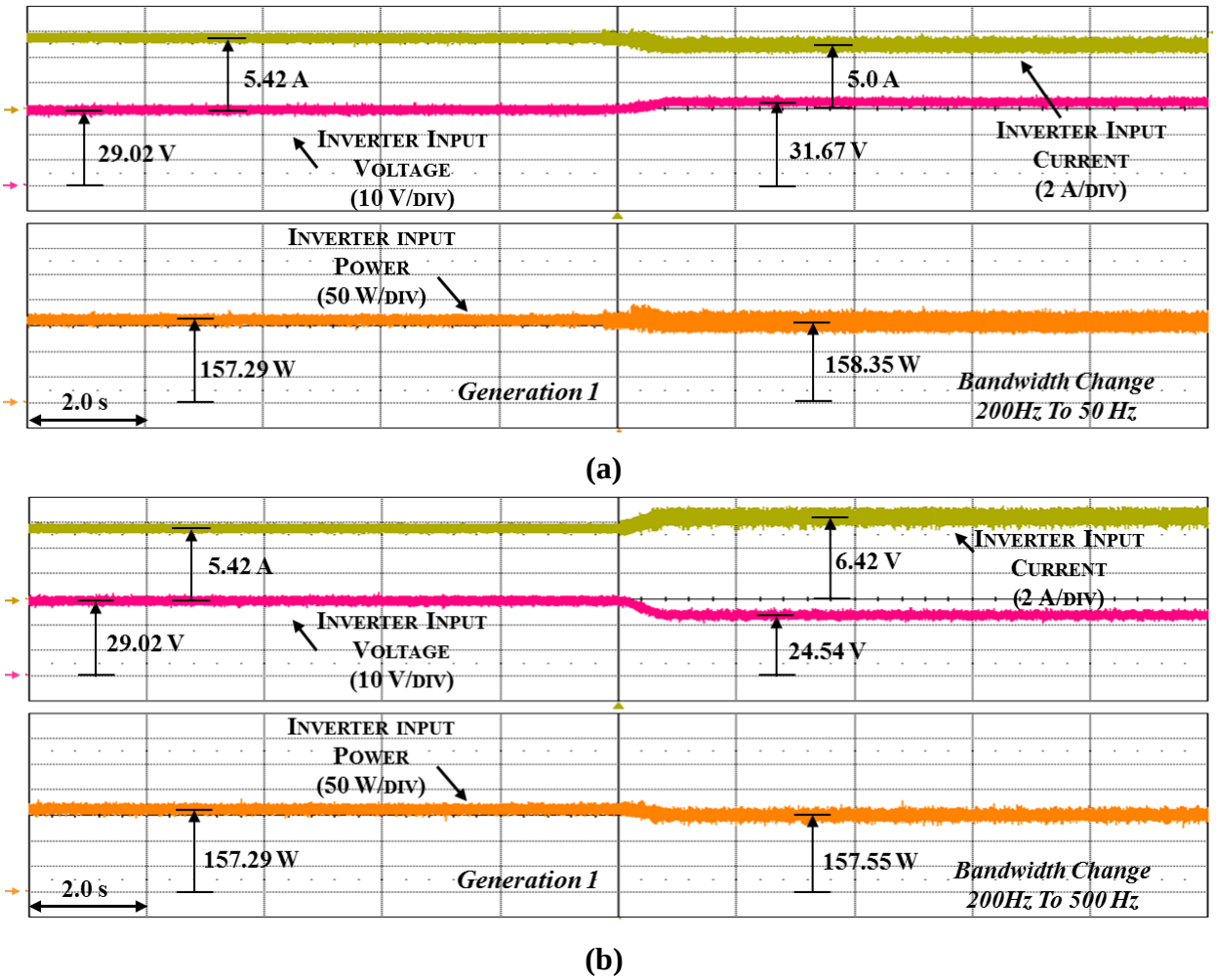

Figure 4.10 Control-loop bandwidth optimization of the proposed PV source simulator connected to the commercial distributed dc-ac PV micro-inverter (Generation 1); **(a)** Bandwidth change from 200 Hz to 50 Hz and **(b)** Bandwidth change from 200 Hz to 500 Hz

A second generation of the same distributed dc-ac PV micro-inverter (Model: M190-72-240) is connected and tested using the proposed PV source simulator and using an actual PV generator (Model: CS6P-240P) as well. Figs. 4.11(a) and Fig. 4.11(b) show the startup performance of the second generation of the PV micro-inverter when connected to the proposed PV source simulator and to actual PV generator, respectively. The micro-inverter tracks the MPP precisely and reaches steady-state within 650 milliseconds. The results show that the MPPT

algorithm of the second generation of the PV micro-inverter tracks the expected MPP faster than the first generation of the same micro-inverter under the same conditions.

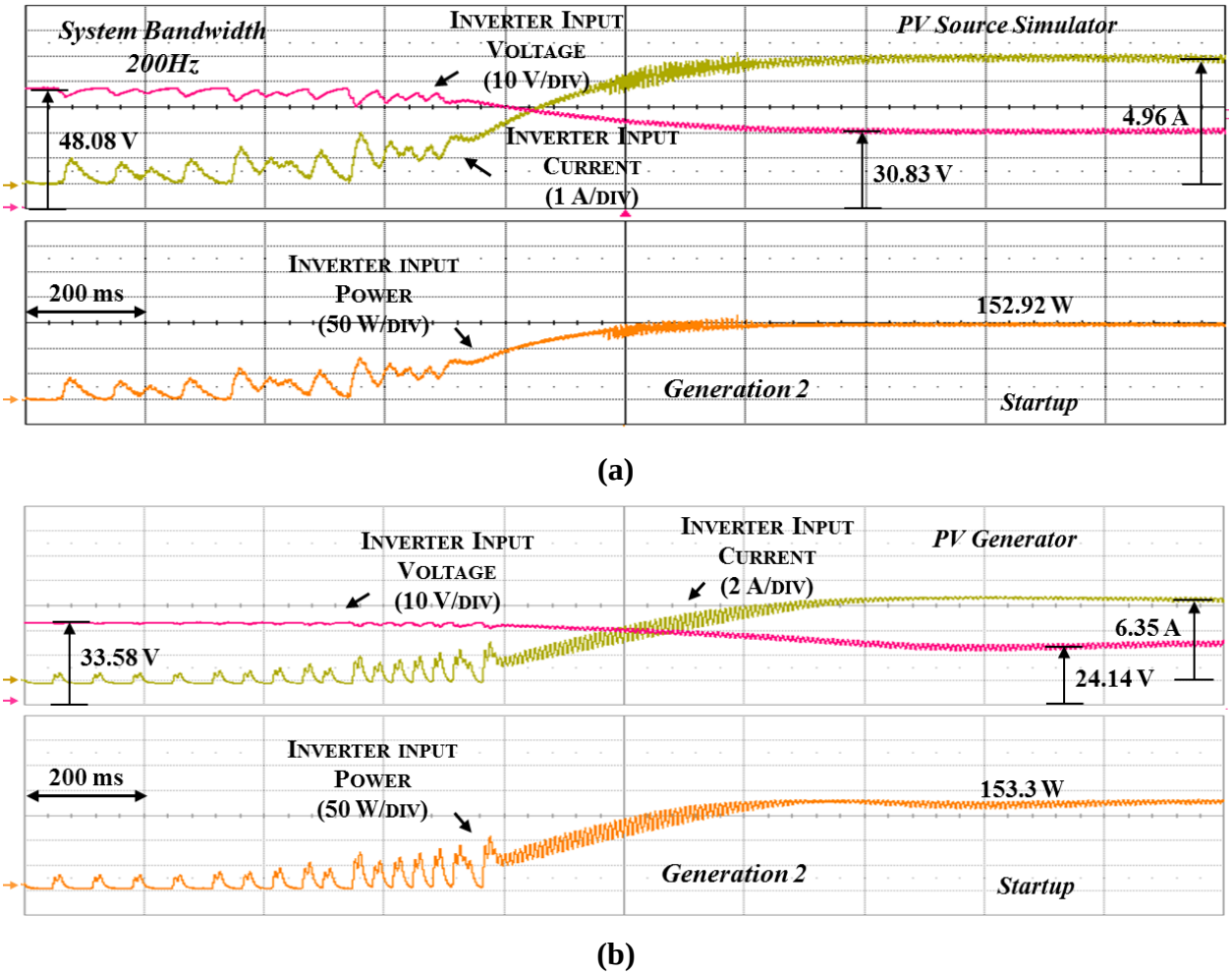

Figure 4.11 Dynamic and static performance evaluation of commercial distributed dc-ac PV micro-inverter (Generation 2); **(a)** Startup waveforms and MPP tracking using PV source simulator and **(b)** Startup waveforms and MPP tracking using actual PV generator

Fig 4.12 and Fig. 4.13 show the dynamic response of the micro-inverter when the irradiance level changes from high to low intensity and from low to high intensity. In Fig. 4.12(a) and Fig. 4.12(b) the MPP shifts down and the micro-inverter tracks the new point

appropriately, whereas in Fig. 4.13(a) and Fig. 4.13(b) the MPP shifts up and the solar micro-inverter tracks the new MPP successfully. The tested solar power conditioning system functioned correctly when it is connected to the proposed PV source simulator as the MPP has been pursued in startup, steady-state, and transient conditions. Moreover, the performance of the micro-inverter is the same when connected either to the proposed PV source simulator or to the actual PV generator, which justifies the validity of the proposed PV source simulator as replacement for actual PV generator.

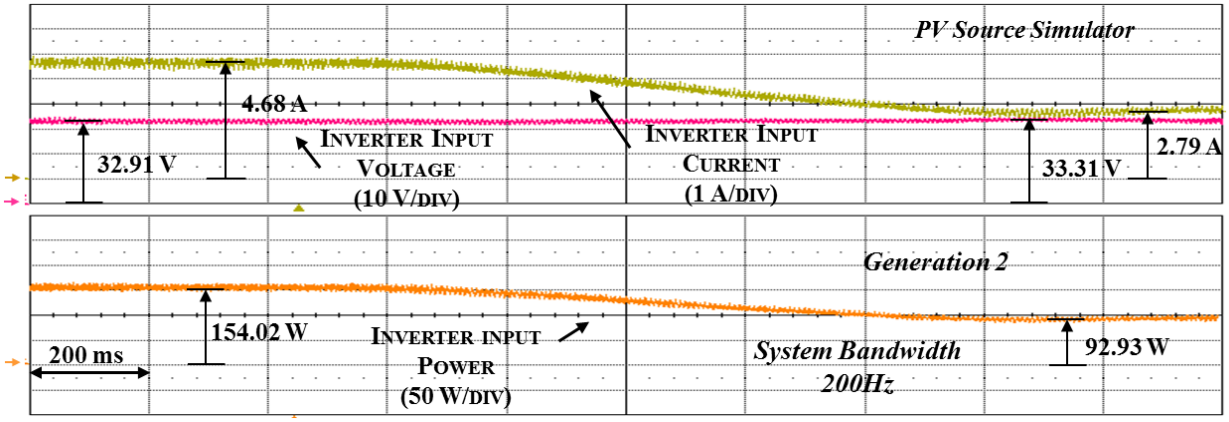

(a)

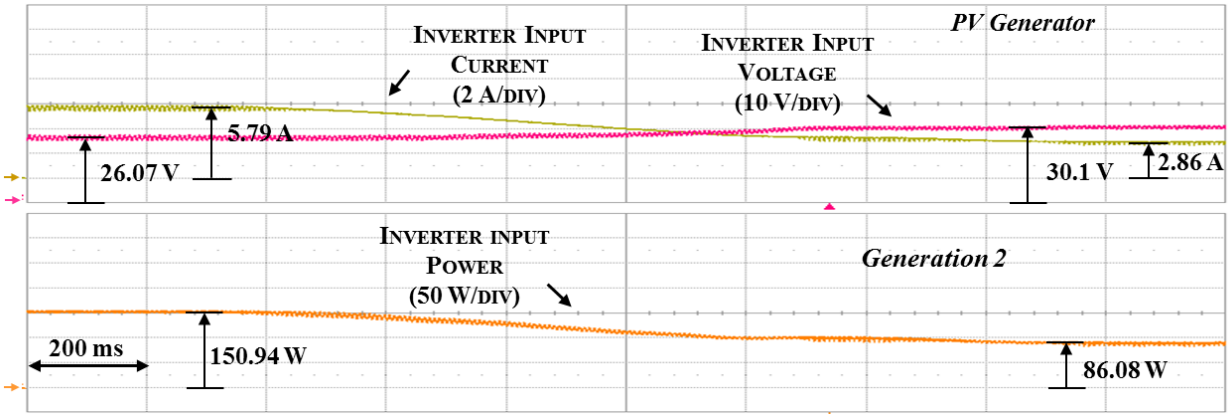

(b)

Figure 4.12 Dynamic and static performance evaluation of commercial distributed dc-ac PV micro-inverter (Generation 2); **(a)** MPP tracking with irradiance step-down using PV source simulator and **(b)** MPP tracking with irradiance step-down using actual PV generator

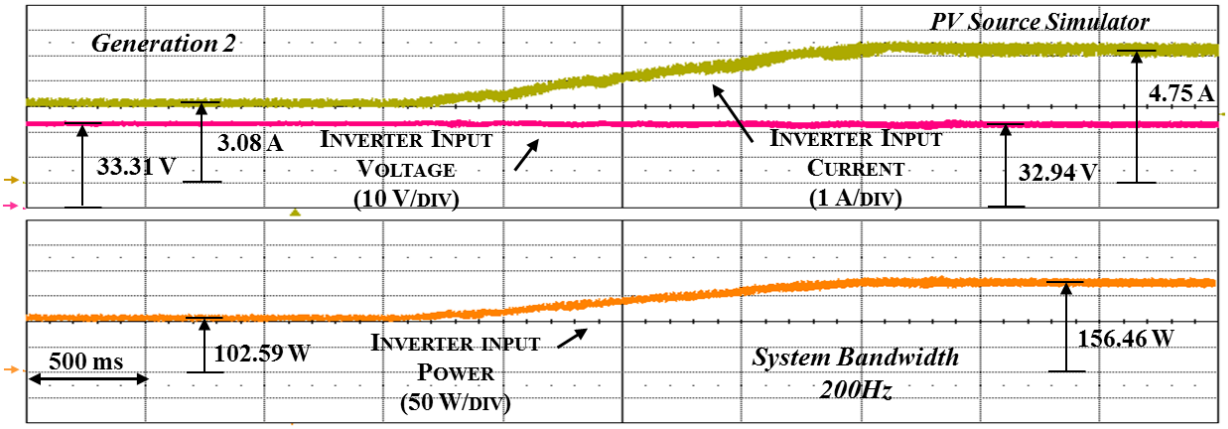

(a)

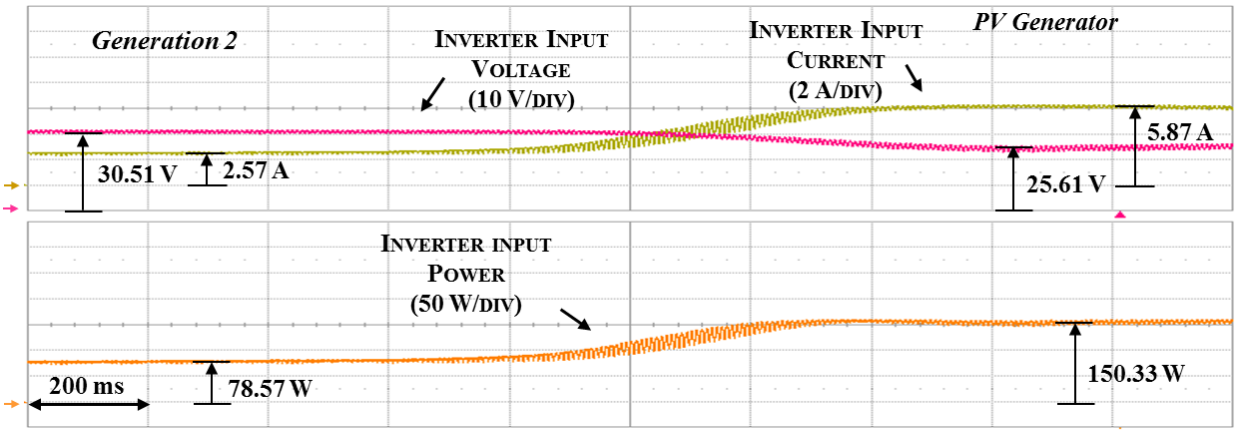

(b)

Figure 4.13 Dynamic and static performance evaluation of commercial distributed dc-ac PV micro-inverter (Generation 2); **(a)** MPP tracking with irradiance step-up using PV source simulator and **(b)** MPP tracking with irradiance step-up using actual PV generator

4.4.2. EVALUATION OF CENTRALIZED DC-AC PV INVERTER

In this section, the dynamic and static performance of a centralized dc-ac PV inverter (Model: SB 5000-US) is evaluated using the proposed PV source simulator during startup, steady-state, and transient conditions. The PV inverter utilizes the conventional H4 topology and incorporates a low-frequency transformer for isolation purposes. The evaluated PV inverter is characterized with high-efficiency and reliability. The open-circuit voltage and the short-circuit current of the proposed PV source simulator are 350 V and 10 A, respectively. Fig. 4.14 shows the startup performance of the centralized PV inverter connected to the proposed PV source simulator. At the beginning, the inverter input voltage is at the open-circuit voltage of the simulator and no power is being transferred to the utility-grid. After that, the MPPT algorithm of the PV inverter starts tracking the MPP, the algorithm reaches steady-state in 90 seconds. Obviously, the PV inverter implements a two-stage MPPT algorithm, the first-stage achieves fast tracking and the second one archives fine tracking [94].

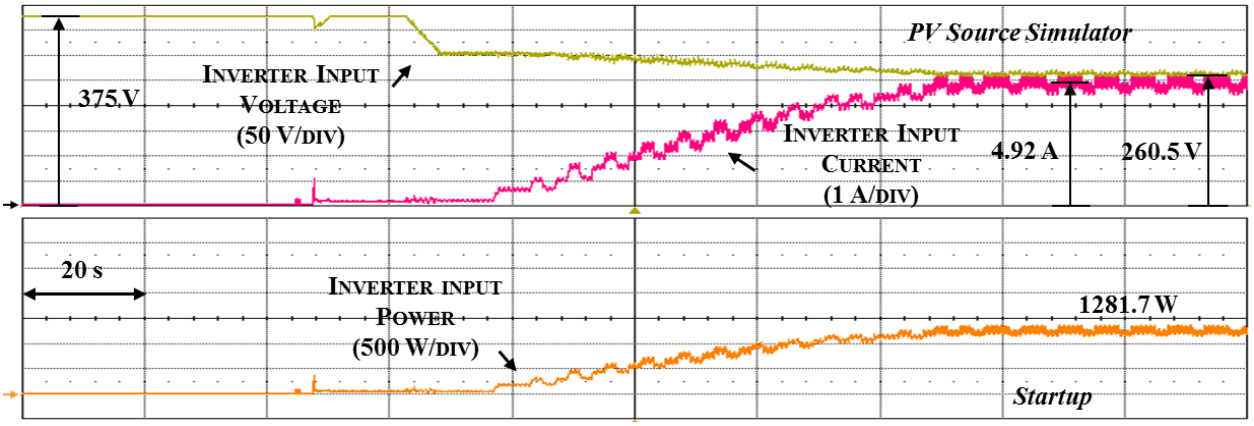

Figure 4.14 Startup performance and MPP tracking evaluation of commercial centralized dc-ac PV inverter suing PV source simulator

Fig. 4.15(a) and Fig. 4.15(b) show the dynamic response of the centralized PV inverter connected to the proposed PV source simulator when the irradiance level changes from full to half intensity and from half to full intensity, respectively. The inverter tracks the expected MPP in both cases successfully. At full intensity, a large fluctuation around the MPP occurred; the ripple content is directly proportional to the PV inverter input power [95]. The MPPT algorithm of the PV inverter must operate the PV system at the MPP with very minimal fluctuation.

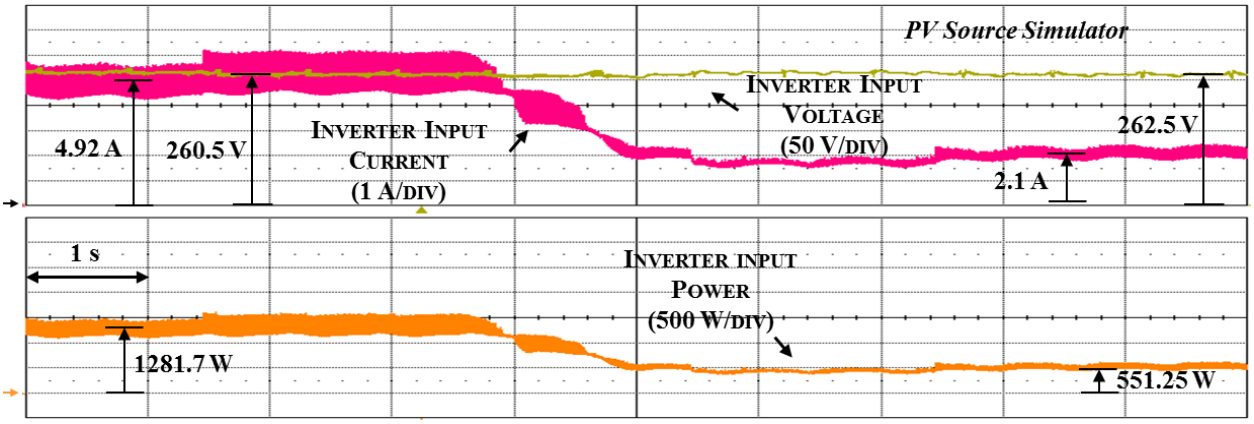

(a)

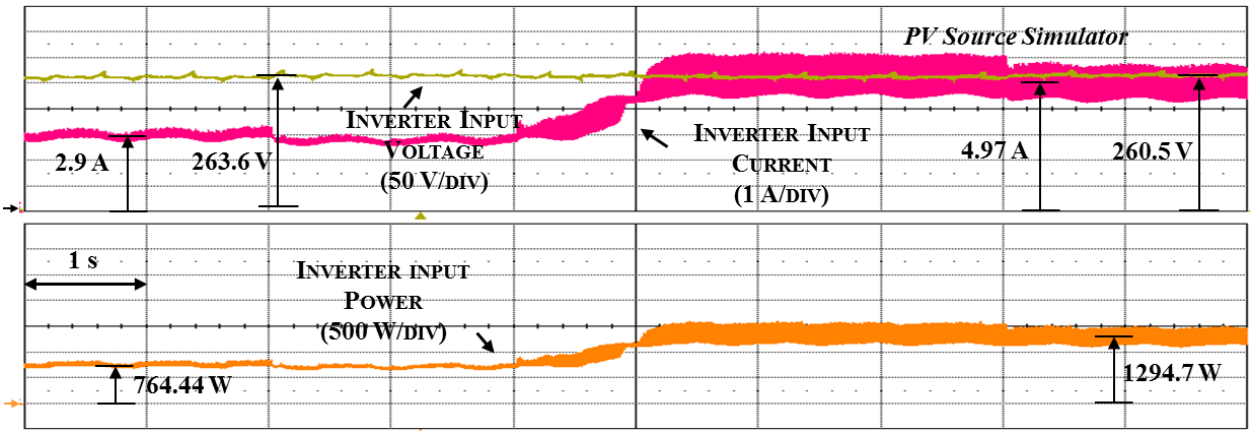

(b)

Figure 4.15 Dynamic and static performance evaluation of commercial centralized dc-ac PV inverter; (a) MPP tracking with irradiance step-down using PV source simulator and (b) MPP tracking with irradiance step-up using PV source simulator

4.5 EVALUATION OF NON-COMMERCIAL SOLAR POWER CONDITIONING SYSTEMS

4.5.1 EVALUATION OF DISTRIBUTED DC-DC PV MICRO-CONVERTER

The static and dynamic performance of a non-commercial distributed dc-dc PV micro-converter is evaluated. The PV micro-converter is a bidirectional switch based high-efficiency isolated resonant converter designed for PV MPPT applications [96]. This micro-converter is rated for 300 W, has a 30-40 V MPPT range, and utilizes a P&O algorithm to track the MPP where the controller adjusts the PV source simulator output voltage based on its instantaneous power. The evaluated solar power conditioning system is tested first with the proposed PV source simulator. After that, the micro-converter is tested with an actual PV generator. The dynamic performance at startup, steady-state, and during transient conditions is captured in both tests. Fig. 4.16(a) and Fig. 4.16(b) show the startup waveforms of the input voltage, input current, and input power of the PV micro-converter connected to the proposed PV source simulator and to actual PV generator, respectively. The micro-converter's MPPT algorithm tracks the expected MPP and reaches steady-state in about 3 seconds in both cases although oscillations around the MPP occurred. These oscillations can be minimized by decreasing the reference voltage step size although; a very small step will highly affect the conversions speed of the MPPT algorithm. One solution is to have a variable step size, which gets smaller toward the MPP [97-100] or to implement a two-stage algorithm; the first stage achieves fast tracking and the second one achieves fine tracking.

Fig. 4.17(a) and Fig. 4.17(b), show the transient waveforms of the input voltage, input current, and input power of the PV micro-converter connected to the proposed PV source

simulator when the irradiance level changes down and up, respectively. Fig. 14.7(c) shows the performance of the PV micro-converter connected to actual PV generator when the irradiance level changes down and up. Input current and voltage change according to the irradiance level and the micro-converter tracks the new MPP point. The performance of the micro-converter connected to either the proposed PV source simulator or the actual PV generator during startup, steady-state, and transient conditions is very similar. The micro-converter tracks the true MPP successfully at all conditions.

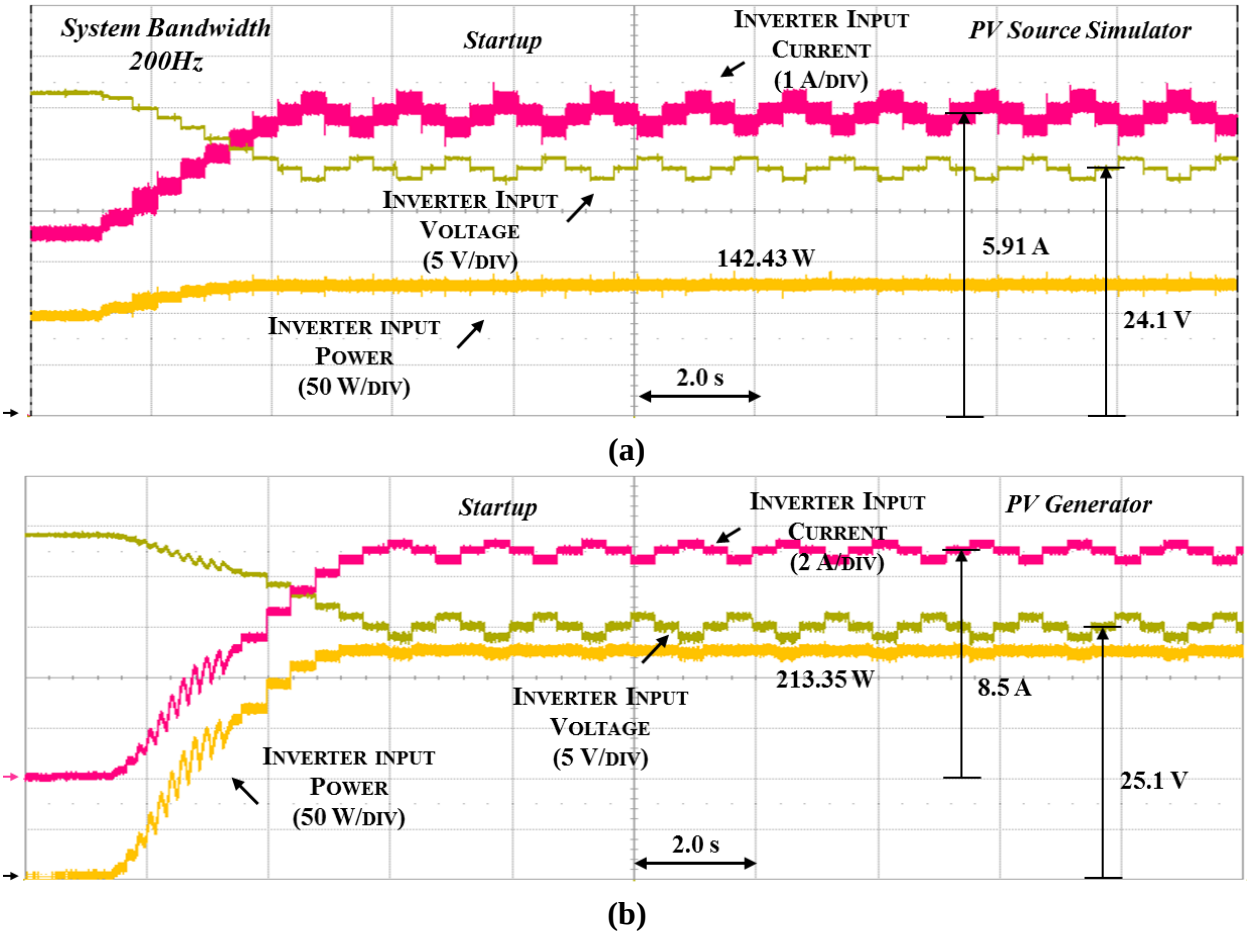

Figure 4.16 Dynamic and static performance evaluation of non-commercial distributed dc-dc PV micro-converter; **(a)** Startup waveforms and MPP tracking using PV source simulator and **(b)** Startup waveforms and MPP tracking using actual PV generator

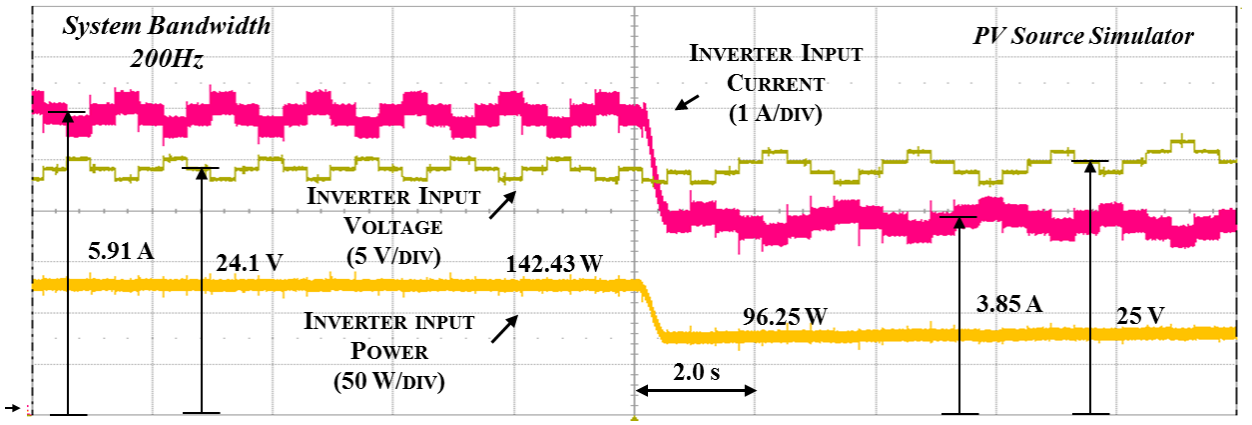

(a)

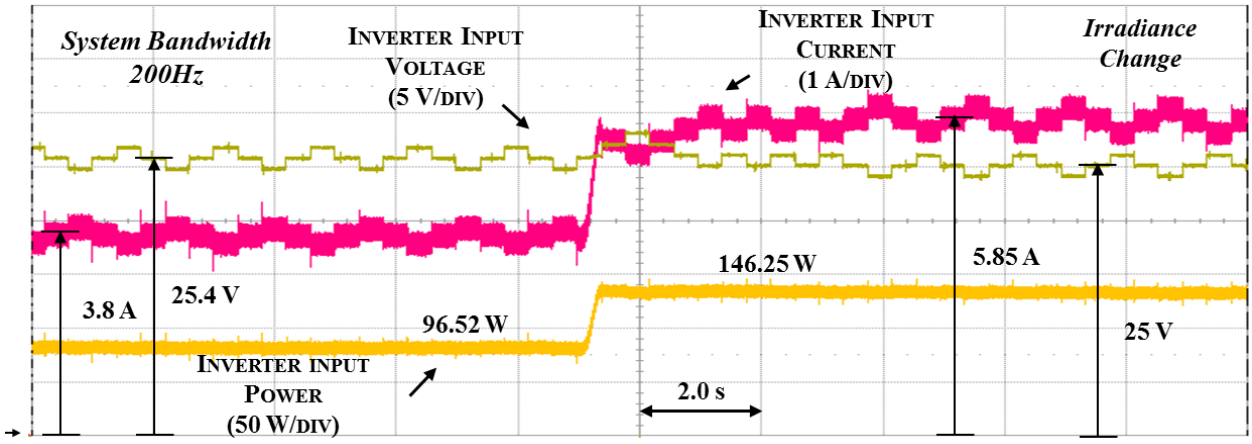

(b)

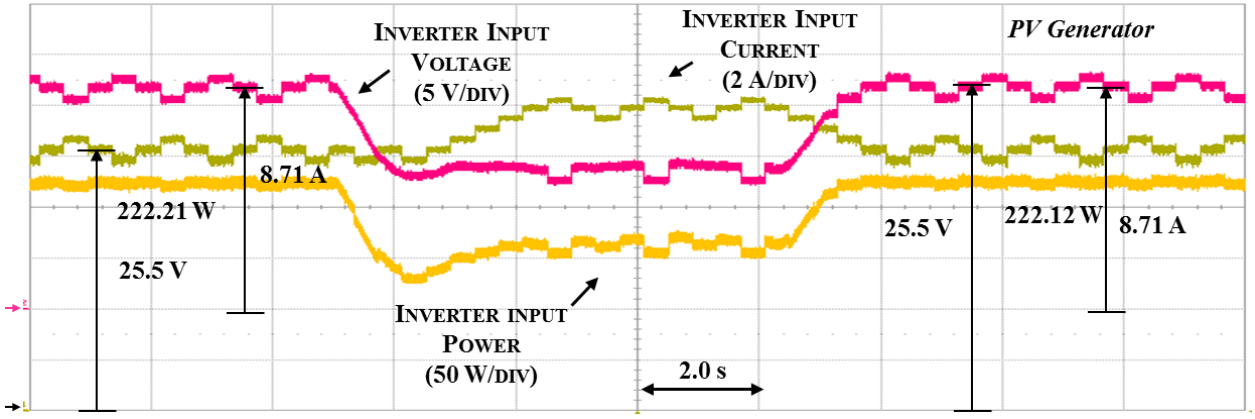

(c)

Figure 4.17 Dynamic and static performance evaluation of non-commercial distributed dc-dc PV micro-converter; **(a)** MPP tracking with irradiance step-down using PV source simulator, **(b)** MPP tracking with irradiance step-up using PV source simulator, and **(c)** MPP tracking with irradiance change using actual PV generator

4.6 SUMMARY

In this chapter, the closed-loop output impedance of the proposed PV source simulators in Chapter 2 and Chapter 3 is verified and compared to the measured output impedance of actual PV generator at different operating conditions including constant current and constant voltage. Unlike the closed-loop output impedance of the simulator proposed in Chapter 2 that did not match the output impedance profile of actual PV generator due to the double resonant peaks created from the implementation of the two-stage output filter, the closed-loop output impedance of the PV source simulator proposed in Chapter 3 matches the output impedance profile of actual PV generator closely. In low-frequency range, the output impedance is constant resembling resistive characteristic, and in high-frequency ranges (above 100 Hz) the magnitude and phase of the output impedance decreases resembling capacitive characteristic. Moreover, the phase of the output impedance at all operating points is between $\pm 90^{o}$.

In the second part of this chapter, evaluation of different commercial and non-commercial solar power conditioning systems is done using the proposed PV source simulator. The process includes the evaluation of the performance in startup, steady-state, and transient conditions. Moreover, the evaluated systems have been tested using an actual PV generator. The dynamic and static performance of those solar power conditioning systems is similar when connected either to the proposed PV source simulator or to the actual PV generates. Accordingly, the proposed PV source simulator in Chapter 3 can be claimed as a substitute for actual PV systems.

CHAPTER 5

CONCLUSIONS AND FUTURE WORKS

5.1 CONCLUSIONS

This dissertation focuses on the design optimization, modeling, and control of PV source simulators. A PV source simulator is a convenient tool for the dynamic and static evaluation of solar power conditioning systems and their associated MPPT techniques. Throughout this research, two different PV source simulator systems are designed, modeled, and experimentally verified. A detailed systematic design procedure for the control and power circuits of the proposed systems is introduced. The first proposed PV source simulator is characterized with the implementation of two novel analog reference generation circuits with a bandwidth of 90 kHz. Moreover, the simulator system utilizes a two-stage output filter along with a switching power-stage to improve the control-loop bandwidth. The design of the first system is then enhanced with the second PV source simulator system. This system features:

a. High power-stage efficiency. The power stage includes a three-phase front-end ac-dc converter and a three-phase interleaved dc-dc converter. The peak efficiency of 96.4% was measured at 1.8 kW MPP operating point.
b. Fast transient response-time. The output current of the proposed PV source simulator recovers within 3.2 milliseconds to ±5% of the steady-state output value, which is eight times faster than the fastest reported MPPT control response of 25 milliseconds.

c. Chopper type phase leg power circuit preventing shoot-through fault. Both ac-dc and dc-dc converters adopt the chopper type phase leg circuit, which has either a top switch in series with a bottom diode or a top diode in series with a bottom switch that prevents from shoot through faults found in a conventional phase-leg with switches for both top and bottom devices.

d. The output impedance resembles typical PV generator output impedance, which is resistive in the low-frequency range and becomes capacitive in the high-frequency range.

Moreover, a hybrid control system is implemented to combine the advantages of analog and digital based simulators. This technique decreases digital computational times allowing a higher switching frequency and therefor a higher control-loop bandwidth to be selected.

The major results of this research can be summarized into three main parts. The first part of this research focuses on the development of new and novel reference generation techniques to create the current-voltage reference characteristic of an actual PV generator. This technique should be accurate, simple, and flexible. Three different analog circuits have been proposed and experimentally implemented: (i) PV cell diode model with external current source, (iii) illuminated PV cell with controllable light source. (ii) un-illuminated PV cell with external current source. The implementation of the first approach is simple where the PV equivalent circuit is experimentally implemented using a voltage-controlled current source and a voltage-controlled voltage source. The current-voltage characteristic of the diode should match the desired emulated PV characteristic based on the approximation model. The second approach is a real-time simulator and hence, is the most accurate among other approaches. The third technique

combines the advantages of the first two techniques. The real-time reference curve is generated using the external current source as sunlight illumination.

The second part of this research focuses on the development of a power-stage circuit that is adequate for PV source simulators. Four major design features are essentials in the power-stage of a PV source simulator: (i) high power-stage efficiency (> 90%), (ii) low output-current and voltage ripples ($\Delta I < 1$ A and $\Delta V < 1$ V), (iii) fast transient response-time (< 25 milliseconds), and (iv) output impedance matching with actual PV generator. In the first simulator system, a two-stage LC output filter is implemented with a single-phase dc-dc buck converter to allow ripple-free output and a high cut-off frequency of the output filter for fast loop bandwidth design. The system achieved a reasonably fast response-time under irradiance perturbation up to 40 Hz. The peak efficiency of the proposed system is 95%. In the second simulator, the proposed system includes a novel three-phase ac-dc dual boost rectifier cascaded with a three-phase dc-dc interleaved buck converter. The dual boost circuit integrates two active switches per phase or six active switches for a three-phase system without having two switches in series for each phase leg; in consequence, the shoot-through failure is avoided. This distinguished feature makes the dual boost topologies attractive due to their high reliability. Moreover, the three-phase dc-dc converter helps improve system transient response (< 25 milliseconds) though producing low output ripple (< 1 A). The proposed two-stage simulator achieved 96.4% efficiency at the maximum power point.

The third part of this research focuses on how to justify the validity of the proposed PV source simulator as a replacement for actual PV generator. Three main experiments have been conducted: (i) measurement of the closed-loop output impedance of the proposed PV source simulators, (ii) evaluation of the dynamic performance of different commercial and non-

commercial solar power conditioning systems along with their associated MPPT algorithms using the proposed PV source simulator at startup, steady-state, and transient conditions, and (iii) evaluation of the performance of different commercial and non-commercial solar power conditioning systems using an actual PV generator at startup, steady-state, and transient conditions. The closed-loop output impedance of the PV source simulator proposed in Chapter 2 did not match the output impedance profile of an actual PV generator due to the double resonant peaks created from the utilization of the two-stage output filter. Advanced control techniques can be applied to remove the effect of the output filter on the impedance of the simulator. The closed-loop impedance of the PV source simulator proposed in Chapter 3 matches the output impedance profile of an actual PV generator closely in different operating regions including constant current and constant voltage. The output impedance of the proposed PV source simulator is constant in the low-frequency range resembling resistive characteristic; in the high-frequency range, the impedance magnitude decreases resembling capacitive characteristic. Moreover, the phase of the output impedance at all operating points is between $\pm 90^{o}$.The performances of the evaluated solar power conditioning systems connected to either the PV source simulator proposed in Chapter 3 or to the actual PV generator is very similar. The evaluated systems track the expected MPP at startup, steady-state, and transient conditions.

As a conclusion, the proposed PV source simulator can be claimed as a substitute to actual PV generators. The proposed system matches the static and dynamic characteristics of actual PV generators.

5.2 FUTURE WORKS

Further improvements on the design of the proposed PV source simulator can be applied to enhance the performance of the simulator control system to be faster than the response of any newly proposed MPPT algorithms. First, advanced linear and non-linear control techniques can be applied to the control system to improve the transient response-time to match that of linear PV source simulators (< 1 milliseconds). Second, increasing the switching frequency (up to 100 kHz) of the proposed PV source simulator by incorporating more advanced power switches and diodes will enhance the control-loop bandwidth of the proposed system (> 1 kHz).

The same implementation concept can be applied to simulate different types of energy sources. A general type energy source simulator can be designed to emulate the characteristic of different types of cells including PV and thermoelectric generators (TEG).

The measurement of the output impedance of the PV source simulator is not a trivial process. The measurement requires an impedance measurement set, which includes a frequency repose analyzer, a linear amplifier, and an injection transformer. Hence, a detailed theoretical derivation of the closed-loop output impedance of PV source simulators can be done to help researchers to theoretically verify the closed-loop output impedance of their proposed PV source simulators.

5.3 SCHOLARLY CONTRIBUTIONS

- **A. Koran**, K. Sano, R. Kim, and J. Lai, "Design of a Photovoltaic Simulator With a Novel Reference Signal Generator and Two-Stage LC Output Filter," *IEEE Trans. on Power Electronics*, vol. 25, no. 5, pp. 1331–1338, May 2010.
- **A. Koran**, T. LaBella, and J. Lai, "High-Efficiency Photovoltaic Source Simulator with Fast Response-Time for Solar Power Conditioning Systems Evaluation," *IEEE Trans. on Power Electronic*, to be published.
- R. Kim, J. Lai, B. York, and **A. Koran**, "Analysis and Design of Maximum Power Point Tracking Scheme for Thermoelectric Battery Energy Storage System," *IEEE Trans. on Power Electronics*, vol. 56, no. 9, pp. 3709–3716, September 2009.
- Y. Cho, **A. Koran**, H. Miwa, B. York and J. Lai, "An Active Current Reconstruction and Balancing Strategy with DC-Link Current Sensing for a Multi-phase Coupled-inductor Converter," *IEEE Trans. on Power Electronics*, vol. 24, no. 4, pp. 1697–1705, April 2012.
- **A. Koran**, K. Sano, R. Kim, and J. Lai, "Design of a Photovoltaic Simulator with a Novel Reference Signal Generator and Two-Stage LC Output Filter," *in Proc. IEEE ECCE Conf.*, 2009, pp. 319 - 326.
- J. Lai, B. York, **A. Koran**, Y. Cho, B. Whitaker, and H. Miwa "High-Efficiency Design of Multiphase Synchronous Mode Soft-Switching Converter for Wide Input and Load Range ," *in Proc. IEEE ECCE Conf.*, 2009, pp. 319 - 326.

- Y. Cho, **A. Koran**, H. Miwa, B. York and J. Lai, "An Active Current Reconstruction and Balancing Strategy with DC-Link Current Sensing for a Multi-phase Coupled-inductor Converter," *in Proc. IEEE ECCE Conf.*, 2010, pp. 3414 - 3419.

REFERENCES

[1] Q. Li and P. Wolfs, "A review of the single phase photovoltaic module integrated converter topologies with three different dc link configurations," *IEEE Trans. Power Electron.*, vol. 23, no. 3, pp. 1320-1333, May 2008.

[2] E. Koutroulis, K. Kalaitzakis, and N. Voulgaris, "Development of a microcontroller-based photovoltaic maximum power point tracking control system," *IEEE Trans. Power Electron.*, vol.16, no. 1, pp. 46-54, January 2001.

[3] M.C. Di Piazza, M. Pucci, A. Ragusa, G. Vitale, "A grid-connected system based on a real time PV emulator: design and experimental set-up," *in Proc. 36th Annu. IEEE IECON Conf.*, 2010, pp. 3237-3243.

[4] L. Zhang, K. Sun, L. Feng, H. Wu, and Y. Xing, "A family of neutral point clamped full-bridge topologies for transformerless photovoltaic grid-tied inverters," *IEEE Trans. Power Electron.*, vol. 28, no. 2, pp. 730-739, February 2013.

[5] G. Vachtsevanos and K. Kalaitzakis, "A hybrid photovoltaic simulator for utility interactive studies," *IEEE Trans. Energy Convers.*, vol. EC-2, no. 2, pp. 227-231, Jun. 1987.

[6] S. Jiang, D. Cao, Y. Li, and F. Peng, "Grid-connected boost-half-bridge photovoltaic microinverter system using repetitive current control and maximum power point tracking," *IEEE Trans. Power Electron.*, vol. 27, no. 11, pp. 4711-4722, November 2012.

[7] Y. Chen and M. Smedley, "A cost-effective single-stage inverter with maximum power point tracking," *IEEE Trans. Power Electron.*, vol. 19, no. 5, pp. 1289-1294, September 2004.

[8] O. Hashimoto, T. Shimizu, and G. Kimura, "A novel high performance utility interactive photovoltaic inverter system," *in Conf. Record 2000 IEEE Ind. Applicat. Conf.*, 2000, pp. 2255–2260.

[9] A. Latham, R. Pilawa-Podguski, K. Odame, and C. Sullivan, " Analysis and optimization of maximum power point tracking algorithms in the presence of noise," *IEEE Trans. Power Electron.*, vol. 28, no. 7, pp. 3479-3494, July 2013.

[10] Y. Kuo, T. Liang, and J. Chen, "Novel maximum-power-point-tracking controller for photovoltaic energy conversion system," *IEEE Trans. Power Electron.*, vol. 48, no. 3, pp. 594-601, June 2001.

[11] T. Esram, J. Kimball, P. Krein, P. Chapman, and P. Midya, "Dynamic maximum power point tracking of photovoltaic arrays using ripple correlation control," *IEEE Trans. Power Electron.*, vol. 21, no. 5, pp. 1282-1291, September 2006.

[12] A. Abdelsalam, A. Massoud, S. Ahmed, and P. Enjeti, "High-performance adaptive perturb and observe MPPT technique for photovoltaic-based microgrids," *IEEE Trans. Power Electron.*, vol. 26, no. 4, pp. 1010-1021, April 2011

[13] A. Singh, A. R. Hota, and A. Patra, "Design and implementation of a programmable solar photovoltaic simulator," *in Proc. IEEE ICPCES Conf.*, 2010, pp. 1-5.

[14] H. Nagayoshi, S. Orio, Y. Kono, and H. Nakajima, "Novel PV array/module I-V curve simulator circuit," *in Proc. IEEE Photovoltaic Spec. Conf.*, 2002, pp. 1535-1538.

[15] H. Votzi, F. A. Himmelstoss, and H. Ertl, "Basic linear-mode solar-cell simulators," *in Proc. 35th Annu. IEEE industrial electronics Conf.*, 2009, pp. 261-265.

[16] H. Lee, M. Lee, S. Lee, H. Lee, H. Nam, S. Park, "Development of photovoltaic simulator based on dc-dc converter," *in Proc. 31st Annu. IEEE INTELEC Energy Conf.*, 2009, pp. 1-5.

[17] H. Liu, M. He, and X. You, "Investigation of photovoltaic array simulators based on different kinds of PWM rectifiers," *in Proc. IEEE ICCCAS Int. Conf.*, 2009, pp. 737-741.

[18] G. Segura, J. Mestre, M. Casas, A. Andreu, "Development of a photovoltaic array emulator system based on a full-bridge structure," *in Proc. 9th Int. Elec. Power Quality and Utilisation Conf.*, 2007, pp. 1-6.

[19] Z. Ziming, Z. Jianwen, S. Haimeng, W. Gang, H. Xiwen, and Z. Shi, "Research on photovolta array emulator system based on a novel zero-voltage zero-current switching converter," *in Proc. Power and Energy Eng. Conf.*, 2010, pp. 1-4.

[20] C. Chang, E. Chang, and H. Cheng, "A High Efficiency Solar Array Simulator Implemented by an LLC Resonant DC/DC Converter," *IEEE IPEC Conf.*, 2010, pp. 2603-2609.

[21] W. Peiyu, T. Boxue, Z. Housheng, and Z. Yanlei, "Research on maximum power point tracker based on solar cells simulator," *in Proc. Int. Advan. Comp. Cont. Conf.*, 2010, pp. 319-323.

[22] L. Lopes and A. Lienhardt, "A simplified nonlinear power source for simulating PV panels," *in Proc. 34th Annu. IEEE Power Electron. Specialist Conf.*, 2003, pp. 1729-1734.

[23] H. Matsukawa, K. Koshiishi, H. Koizumi, K. Kurokawa, M. Hamada, and L. Bo, "Dynamic evaluation of maximum power point tracking operation with PV array simulator," *in Proc. Solar energy and Solar Materials Conf.*, 2002, pp. 537-546.

[24] W. kui, L. Yongdong, R. Jianye, and S. Min, "Design and implementation of a solar array simulator," *in Proc. ICEMS Int. Conf.*, 2004, pp. 2633 - 2636.

[25] P. Marenholtz, "Programmable solar array simulator," *IEEE Trans. Aerospace and Electronic Systems*, vol. AES-2, no. 6, pp. 104-107, Nov. 1966.

[26] J. Ollila, "A medium power PV-array simulator with a robust control strategy," *in Proc. IEEE Conf.* Control Appl., 1995, pp. 40-45.

[27] S. Kukami, C. Thean, and A. Kong, "A novel PC based solar electric panel simulator," *in Proc. 5th Int. PEDS Conf.*, 2003, pp. 848 - 852.

[28] A. Nanakos and E. Tatakis, "Static and dynamic response of a photovoltaic characteristics simulator," *in Proc. 13th EPE-PEMC Conf.*, 2008, pp. 1827 - 1833.

[29] E. Koutroulis, K. Kalaitzakis, and V. Tzitzilonis, "Development of an FPGA-based system for real-time simulation of photovoltaic modules," *in Proc. IEEE RSP Conf.*, 2006, pp. 200-208.

[30] O. Midtgard, "A simple photovoltaic simulator for testing of power electronics," *in Proc. Eur. Conf. Power Electron.* Appl., 2007, pp. 1-10.

[31] H. Nagayoshi, "Characterization of the module/array simulator using I-V magnifier circuit of a pn photo-sensor," *in Proc. 3rd World Conf. Photovoltaic Energy Conv.*, 2003, pp. 2023-2026.

[32] A. Koran, K. Sano, R. Kim, and J. Lai, "Design of a Photovoltaic Simulator With a Novel Reference Signal Generator and Two-Stage LC Output Filter," *IEEE Trans. Power Electron.*, vol. 25, no. 5, pp. 1331-1338, May 2010.

[33] A. Koran, K. Sano, R. Kim, and J. Lai, "Design of a Photovoltaic Simulator with a Novel Reference Signal Generator and Two-Stage LC Output Filter," *in Proc. IEEE ECCE Conf.*, 2009, pp. 319 - 326.

[34] M. Park and I.Yu, "A novel real-time simulation technique of photovoltaic generation systems using RTDS," *IEEE Trans. Energy Convers.*, vol. 19, no. 1, pp. 164-169, Mar. 2004.

[35] H. Nagayoshi and M. Atesh, "Partial shading effect emulation using multi small scale module simulator units," *in Proc. 31st IEEE Photovoltaic Specialists Conf.*, 2005, pp. 1710-1713.

[36] L. Zárate, L. Vilhena, B. Neto, D. Soares, and F. Bittencout, "Artificial neural networks applied for representation of curves current-voltage of photovoltaic modules," *in Proc. 6th IEEE Int. Conf. Industrial Informatics*, 2008, pp. 1644-1649.

[37] L. Bun, B. Raison, G. Rostaing, S. Bacha, A. Rumeau, A. Labonne, "Development of a real time photovoltaic simulator in normal and abnormal operations," *in Proc. 37th Annu. IEEE IECON Conf.*, 2011, pp. 867 - 872.

[38] D. Dolan, J. Durago, J. Crowfoot, and Taufik, "Simulation of a photovoltaic emulator," *in Proc. North American Power Symposium*, 2010, pp. 1 - 7.

[39] S. Ldloyd, G. Smith, and D. Infield, "Design and construction of a modular electronic photovoltaic simulator," *in Proc. Inst. Electr. Eng. Power Electron.* Variable Speed Drives Conf., 2000, pp. 120-123.

[40] J. Lee, B. Min, T. Kim, J. Kim, M. Ryu, J. Baek, D. Yoo, and J. Yoo, "Development of a photovoltaic simulator with novel simulation method of photovoltaic characteristics," *in Proc. 31st INTELEC Conf.*, 2009, pp. 1-5.

[41] J. Blanes, F. Toledo, S. Montero, and A. Garrigos, "In-site real-time photovoltaic I-V curves and maximum power point estimator," *IEEE Trans. Power Electron.*, vol. 28, no. 3, pp. 1234-1240, March 2013.

[42] K. Khouzam, C. Ly, C. Koh, and P. Ng, "Simulation and real-time modeling of space photovoltaic systems," *in Proc. IEEE WCPEC Conf.*, 1994, vol. 2, pp. 2038-2041.

[43] M. Park and I. Yu, "A novel real-time simulation technique of photovoltaic generation systems using RTDS," *IEEE Trans. Energy Convers.*, vol. 19, no. 1, pp. 164-169, Mar. 2004.

[44] V. Preethishri, K. Kumar, and P. Sivakumar, "Embedded emulator of photovoltaic array and wind driven induction generator by using digital signal controller (tms320f28335)," *in Proc. Power electronics IICPE conf.*, 2010, pp. 1-7.

[45] Z. Housheng and Z. Yanlei, "Research on a Novel Digital Photovoltaic Array Simulator," *in Proc. Int. ICICTA Conf.*, 2010, pp. 1077 - 1080.

[46] S. Gonzalez, S. Kuszmaul, and D. Deuel, and R. Lucca, "PV array simulator development and validation," *in Proc. 35th IEEE PVS Conf.*, 2010, pp. 2849 - 2852.

[47] L. Fraas, and L. Patain, *Solar cells and their applications*. Hoboken, New Jersey: Wiley, 2010, pp. 77.

[48] M. Villalva, J. Gazoli, and E. Filho, "Comprehensive Approach to Modeling and Simulation of Photovoltaic Arrays," *IEEE Trans. Power Electron.* , vol. 24, no. 5, pp. 1198-1208, May 2009.

[49] R. Kumar and M. Surech, "Facility to measure solar cell ac parameters using an impedance spectroscopy technique," *AIP Trans. Rev. Sci. Instrum.*, vol. 73, no. 8, pp. 3422-3426, August 2001.

[50] M. Saadawi, A. Hassan, K. Abo-Al-Ez, and M. Kandil, "A proposed dynamic model of photovoltaic-DG system," *in Proc. 1st IEEE INREC Conf.*, 2010, pp. 1-6.

[51] H. Moller, *Semiconductors for solar cells*. Norwodd, MA: Artech House, 1993, pp. 31-33.

[52] S. Jain and V.Agarwal, "A newalgorithm for rapid tracking of approximate maximum power point in photovoltaic systems," *IEEE Power Electron. Letter*, vol. 2, no. 1, pp. 16–19, Mar. 2004.

[53] Y.-C. Kuo, T.-J. Liang, and J.-F. Chen, "Novel maximum-power-point tracking controller for photovoltaic energy conversion system," *IEEE Trans. Ind. Electron.*, vol. 48, no. 3, pp. 594–601, Jun. 2001.

[54] M. A. S. Masoum, H. Dehbonei, and E. F. Fuchs, "Theoretical and experimental analyses of photovoltaic systems with voltage and current-based maximum power-point tracking," *IEEE Trans. Energy Convers.*, vol. 17, no. 4, pp. 514–522, Dec. 2002.

[55] S. Yuvarajan and S. Xu, "Photo-voltaic power converter with a simple maximum-power-point-tracker," *in Proc. 2003 Int. Symp. Circuits Syst.*, 2003, pp. III-399–III-402.

[56] B. M. Wilamowski and X. Li, "Fuzzy system based maximum power point tracking for PV system," *in Proc. 28th Annu. Conf. IEEE Ind. Electron. Soc.*, 2002, pp. 3280–3284.

[57] M. Veerachary, T. Senjyu, and K. Uezato, "Neural-network-based maximum-power-point tracking of coupled-inductor interleaved-boost converter- supplied PV system using fuzzy controller*," IEEE Trans. Ind. Electron.*, vol. 50, no. 4, pp. 749–758, Aug. 2003.

[58] Y. H. Lim and D. C. Hamill, “Simple maximum power point tracker for photovoltaic arrays,” *Electron. Lett.*, vol. 36, pp. 997–999, May 2000.

[59] T. Kitano, M. Matsui, and D.-h. Xu, “Power sensor-less MPPT control scheme utilizing power balance at DC link-system design to ensure stability and response,” *in Proc. 27th Annu. Conf. IEEE Ind. Electron. Soc.*, 2001, pp. 1309–1314.

[60] T. Esram and P. Chapman, "Comparison of photovoltaic array maximum power point tracking techniques," *IEEE Trans. Power Electron.*, vol. 22, no. 2, pp. 439-449, June 2007.

[61] L. Castaner, and S. Silvestre, *Modeling photovoltaic systems using PSpice*. Wiley, 2003, pp. 234.

[62] Manual of Venable Frequency Response Analyzer Model 3120, Venable Instruments, Austin, TX, 2006.

[63] B. Anderson and R. Anderson, *Fundamentals of semiconductor devices*. McGraw-Hill, 2004, pp. 682.

[64] C. Chang, E. Chang, and H. Cheng, "A High Efficiency Solar Array Simulator Implemented by an LLC Resonant DC-DC Converter," *IEEE Trans. Power Electron.*, vol. 28, no. 6, pp. 3039-3046, June 2013.

[65] Y. Li, T. Lee, F. Peng, and D. Liu, "A Hybrid control strategy for photovoltaic simulator," *in Proc. 24th Annu. IEEE APEC Conf.*, 2009, pp. 899 - 903

[66] Q. Zeng, P. Song, and L. Chang, "A photovoltaic simulator based on dc chopper," *in Proc. IEEE CCECE Conf.*, 2002, vol. 1, pp. 257-261.

[67] J. Chen, J. Chen, C. Gong, X. Chen, and F. Zhang, "A novel high reliability dual-boost half-bridge reversible PWM rectifier," *in Proc. IEEE PESC Conf.*, 2008, pp. 3330-3334.

[68] C. Liu, P. Sun, J. Lai, Y. Ji, M. Wang, C. Chen, and G. Cai, "Cascaded dual-boost/buck active-front-end converter for intelligent universal transformer," *IEEE Trans. Indus. Electron.*, vol. 59, no. 12, pp. 4671-4680, December 2012.

[69] S. Hiti and D. Boroyevich, "Control of front-end three-phase boost rectifier," *in Proc. 9th IEEE APEC Conf.*, 1994, pp. 927-933.

[70] V. Blasko, "A hybrid PWM strategy combining modified space vector and triangle comparison methods," *in Proc. 27th IEEE PESC Conf.*, 1996, pp. 1872 -1878.

[71] Y. Qiu, M. Xu, K. Yao, J. Sun, and F. Lee, "Multifrequency small-signal model for buck and multiphase buck converters," *IEEE Trans. Power Electron.*, vol. 21, no. 5, pp. 1185-1192, September 2006.

[72] S. Dhople, A. Davoudi, A. Dominguez, and P. Chapman, "A unified approach to reliability assessment of multiphase DC-DC converters in photovoltaic energy conversion Systems," *IEEE Trans. Power Electron.*, vol. 27, no. 2, pp. 739-751, February 2012.

[73] H. Nagaraja, D. Kastha, and A. Patra, "Design prinsibles of a symmetrically coupled inductor structure for multiphase synchronous buck converters," *IEEE Trans. Power Electron.*, vol. 58, no. 3, pp. 988-997, March 2011.

[74] B. Yin, R. Oruganti, S. Kumar, and A. Bhat, "A simple single-input-single-output (SISO) model for three-phase PWM rectifiers," *IEEE Trans. Power Electron.*, vol. 24, no. 3, pp. 620-631, March 2009.

[75] S. Lyden, M. Haque, A. Gargoom, M. Negnevisky, and P. Muoka, "Modelling and parameter estimation of photovoltaic cell," *in Proc. 22nd Australian Univ. Power Eng. Conf. (AUPEC)*, 2012, pp. 1-6.

[76] H. Lee, L. Phuong, P. Dzung, N. Dan Vu, and D. Khoa, "The new maximum power point tracking algorithm using ANN-based solar PV systems," *in Proc. IEEE TENCON Conf.*, 2010, pp. 2179-2184.

[77] B. Alajmi, K. Ahmed, S. Finney, and B. Williams, "Fuzzy-Logic-Control Approach of a Modified Hill-Climbing Method for Maximum Power Point in Microgrid Standalone Photovoltaic System," *IEEE Trans. Power Electron.*, vol. 26, no. 4, pp. 1022-1030, April 2011.

[78] 62150H-600S Solar Array Simulation Datasheet, Chroma, Lake Forest, CA, 2000.

[79] M. Venkatesan, R. Rajeswari, and K. Keerthivasan, "A survey of single phase grid connected photovoltaic system," *in Proc. IEEE Int. Conf. on Emerging trends in Sci., Eng. and Tech.*, 2012, pp. 404-408.

[80] T. Wu, H. Nien, H. Hsieh, and C. Shen, "PV Power injection and active power filtering with amplitude-clamping and amplitude-scaling algorithms," *IEEE Trans. Ind. Application*, vol. 43, no. 3, pp. 731-741, May/June 2007.

[81] E. Koutroulis and F. Blaabjerg, "Design optimization of transformerless grid-connected PV inverters including reliability," *IEEE Trans. Power Electron.*, vol. 28, no. 1, pp. 325-335, January 2013.

[82] Z. Zhao, M. Xu, Q. Chen, J. Lai, and Y. Cho, "Derivation, analysis, and implementation of a boost–buck converter-based high-efficiency PV inverter," *IEEE Trans. Power Electron.*, vol. 27, no. 3, pp. 1304-1312, March 2012.

[83] J. Slevaraj and N. Rahim, "Multilevel inverter for grid-connected PV system employing digital PI controller," *IEEE Trans. Ind. Electron.*, vol. 56, no. 1, pp. 150-158, January 2009.

[84] J. Kwon, B. Kwon, and K. Nam, " Grid-Connected Photovoltaic Multistring PCS With PV Current Variation Reduction Control" *IEEE Trans. Ind. Electron.*, vol. 60, no. 4, pp. 1503-1511, April 2013.

[85] N. Rahim and J. Selvaraj, " Multistring five-level inverter with novel PWM control scheme for PV application" *IEEE Trans. Ind. Electron.*, vol. 57, no. 6, pp. 2111-2123, June 2010.

[86] B. York, W. Yu, and J. Lai, "An integrated boost resonant converter for photovoltaic applications," *IEEE Trans. Power Electron.*, vol. 28, no. 3, pp. 1199-1207, March 2013.

[87] S. Chen, T. Liang, L. Yang, and J. Chen, " A boost converter with capacitor multiplier and coupled inductor for AC module applications" *IEEE Trans. Ind. Electron.*, vol. 60, no. 4, pp. 1503-1511, April 2013.

[88] M. Wuest, P. Toggweiler, and J. Riatsch, "Single cell converter system (SCCS)," *in Proc. 1st IEEE WCPEC*, vol. 1, 1994, pp. 813–815.

[89] A. Maki, S. Valkealahti, and T. Suntio, "Dynamic terminal characteristics of a photovoltaic generator," *in Proc. 14th IEEE EPE/PEMC Conf.*, 2010, pp. T12-76-T12-80.

[90] L. Nousiainen, J. Puukko, A. Maki, T. Messo, J. Huusari, J. Jokipii, J. Viinamaki, T. Lobera, S. Valkealahti, and T. Suntio, "Photovoltaic generator as an input for power electronic converters," *IEEE Trans. Power Electron.*, vol. 28, no. 6, pp. 3028-3038, June 2013.

[91] M175-24-240 Enphase Micro-Inverter Models M175 and M200 Datasheet, Enphase Energy Inc., Petaluma, CA, 2008.

[92] M190-72-240 Enphase Micro-inverter Models M190™ and M210™ Datasheet, Enphase Energy Inc., Petaluma, CA, 2011.

[93] SB 5000-US Sunny Boy 5000-US / 6000-US / 7000-US / 8000-US Datasheet, SMA America, LLC, Rocklin, CA.

[94] S. Jain and V. Agarwal, "A new algorithm for rapid tracking of approximate maximum power point in photovoltaic systems," *IEEE Power Electron. Lett.*, vol. 2, no. 1, pp. 16–19, Mar. 2004.

[95] S. Kjaer, J. Pedersen, and F. Blaabjerg, " A review of single-phase grid-connected inverters for photovoltaic odules," *IEEE Trans. Ind. Application*, vol. 41, no. 5, pp. 1292-1306, September/October 2005.

[96] T. LaBella, W. Yu, and J. Lai, "A bidirectional switch based high-efficiency isolated resonant converter for PV applications," unpublished.

[97] W. Xiao and W. G. Dunford, "A modified adaptive hill climbing MPPT method for photovoltaic power systems," *in Proc. 35th Annual IEEE Power Electron. Spec. Conf.*, 2004, pp. 1957–1963.

[98] A. Al-Amoudi and L. Zhang, "Optimal control of a grid-connected PV system for maximum power point tracking and unity power factor," *in Proc. Seventh Int. Conf. Power Electron. Variable Speed Drives*, 1998, pp. 80–85.

[99] C.-C. Hua and J.-R. Lin, "Fully digital control of distributed photovoltaic power systems," *in Proc. IEEE Int. Symp. Ind. Electron.* 2001, pp. 1–6.

[100] N. Femia, G. Petrone, G. Spagnuolo, and M. Vitelli, "Optimization of perturb and observe maximum power point tracking method," *IEEE Trans. Power Electron.*, vol. 20, no. 4, pp. 963–973, Jul. 2005.